

A task-space oriented approach for the reproduction of sit-to-stand motion using operational space control

Von der Fakultät für Ingenieurwissenschaften,
Abteilung Maschinenbau und Verfahrenstechnik der
Universität Duisburg-Essen
zur Erlangung des akademischen Grades
einer

Doktorin der Ingenieurwissenschaften
– Dr.-Ing. –

genehmigte Dissertation
von

Bettina Weber
aus
Krefeld, Deutschland

Referent: Prof. Dr.-Ing. Andrés Kecskeméthy
Korreferent: Prof. Dr. Georg Rauter

Tag der mündlichen Prüfung: 18. Januar 2021

Preface

The following thesis was developed during my time employed as a research associate at the chair of Mechanics and Robotics at the University of Duisburg-Essen, with partial funding by the project “RehaBoard – Ein Computerassistenzsystem für die interdisziplinäre Behandlungsplanung bei Gangstörungen nach Schlaganfall” granted by the European Regional Development Fund (Europäischer Fonds für regionale Entwicklung (EFRE)).

Without a strong support group I could not have achieved my current level of success. First of all, I would like to sincerely express my gratitude to my supervisor Prof. Dr.-Ing. Andrés Kecskeméthy for the opportunity to work on this topic, for his advice and guidance throughout the research process and his style of teaching and precision in scientific work, which is very educational and has always served as an example. In particular I would like to thank you for the chance to finish this thesis despite one year of parenting time and the resulting short duration of preparation time.

Also I would like to thank Prof. Dr. Georg Rauter for his interest in this thesis, his thorough report and his valuable suggestions.

It was a pleasure to spend time with my colleagues, each of whom has allowed for a relaxed and amicable work atmosphere. I am very grateful for the continued support of Dr.-Ing. Dominik Raab during my time at the university. I appreciate his technical assistance in the gait laboratory and also greatly acknowledge all my students help in the experiments and through other contributions to this thesis.

Many thanks goes to Dr.-Ing. Francisco Geu Flores who always provided valuable scientific impulses, helpful suggestions and overall professional expertise and support, beginning with the mentoring of my master’s thesis further to the guidance on my research and throughout my academic teaching.

Finally, I would like to thank my family for their love and understanding throughout my education. I cannot begin to express my exceptional gratitude to my husband Malte Weber for granting extraordinary aid. Not only has he provided me with unbroken encouragement, confidence and moral support, but he also always helped me out from a professional aspect with regard to mathematics and other scientific related topics.

Contents

1	Introduction	1
1.1	State of the art	3
1.1.1	Literature review on the control-based method	6
1.1.2	Literature review on the optimization-based method	8
1.1.3	Literature review on the operational space control method	10
1.2	Introductory example	14
1.3	Motivation and objective	19
1.4	Overview	20
2	Kinematical and dynamical basics	22
2.1	Kinematics of serial manipulators	22
2.1.1	Direct kinematics	23
2.1.1.1	Kinematic singularities	24
2.1.1.2	Kinematic redundancy	25
2.1.1.3	Redundancy resolution within direct kinematics	26
2.1.2	Inverse kinematics	27
2.1.2.1	Redundancy resolution within inverse kinematics	28
2.2	Dynamics of serial manipulators	29
2.2.1	Inverse dynamics	29
2.2.2	Direct dynamics	30
2.2.3	Relationship between joint torques and end-effector forces	30
3	Measurement and model	32

3.1	Sit-to-stand motion capture measurements	32
3.2	Biomechanical model	34
3.2.1	Anthropometric model data	35
3.2.2	Orientation data transmission to the model	38
3.2.3	Dynamic model description	39
3.2.4	Buttocks contact force model	42
3.2.4.1	Kelvin-Voigt model	44
3.2.4.2	Gaussian function model	52
3.2.4.3	Discussion of buttocks force models	54
4	Operational space formulation and control	55
4.1	Operational space dynamic model	55
4.2	Direct dynamics in operational space	56
4.3	Inverse dynamics in operational space	57
4.4	Operational space control method	58
4.5	Application to quadruple pendulum model performing STS motion	62
4.5.1	Task definition for STS motion	62
4.5.2	Posture definition for STS motion	64
4.5.3	Direct dynamics integration	65
5	Simulation results	66
5.1	Approach one: command variables $x_{t_{\text{des}}}$, $y_{t_{\text{des}}}$ and $\varphi_{t_{\text{des}}}$	69
5.2	Approach two: command variables $y_{t_{\text{des}}}$ and $\varphi_{t_{\text{des}}}$	80
6	Comparison to an optimization-based motion generation method	88

6.1	Optimization-based reference method	88
6.2	Implementation for quadruple pendulum model	93
7	Conclusions and outlook	98
7.1	Contributions	98
7.2	Limitations and outlook	99
	Appendices	102
A	Results to introductory example	103
A.1	Computation routine	103
A.2	Cost function values of optimization process	103
A.3	Joint angles, angular velocities and angular accelerations	104
A.4	Joint torques	104
B	Range and null space of the Jacobian matrix	105
C	Equations of motion of quadruple pendulum	106
D	Gaussian function buttocks force fit	107
E	Dynamically consistent pseudo-inverse of the Jacobian matrix	108
F	Simulation results of triple pendulum	109
	Bibliography	112

Abstract

To this day, biomechanics actively research how the nervous system selects particular motion strategies in order to achieve a desired motion. The human sit-to-stand transfer, as one of the most important tasks influencing the quality of life, has been studied extensively through experimental studies. Simulative studies, however, are relatively rare, although anticipating the sit-to-stand movement accurately is essential for many applications, e.g. treatment planning or the design of exoskeletons.

Existing research in sit-to-stand motion prediction has mainly focused on developing direct dynamics strategies in joint space. This thesis addresses the application of a control method in operational space through assigning a desired end-effector motion, i.e. the head trajectory, to a biomechanical four-link skeletal model in the sagittal plane in order to predict healthy sit-to-stand motion. The dynamics of the quadruple pendulum is enhanced by a new Gaussian function model to replicate the contact forces between chair and buttocks during sitting.

Since infinitely many possible configurations exist to perform the desired motion, the mechanism is called redundant with regard to its task. The proposed operational space control scheme is adapted from the field of robotics and resolves those redundancies at kinematic level using a general projector matrix in the null space of the task Jacobian. By this means, the task control is complemented by human posture regulation, which, in this case, considers the orientation of the foot related link. Besides controlling human posture, this method provides freedom to the choice of a suitable pseudo-inverse of the Jacobian matrix that affects performance preferences. With the purpose of finding the fundamental objective that underlies the sit-to-stand motion on a neural level, different pseudo-inverses are tested within posture control for two simulation approaches considering the task command variables. The first approach controls the two dimensional head position as well as the orientation of the upper body. The second approach only regards the vertical position and the orientation as the task.

Simulation results demonstrate physiologically accurate performance predictions in comparison to reference data based on performed sit-to-stand measurements. The method also emerges as being superior compared to the application of a recently published optimization-based control approach in terms of computation time, efficiency and overall generality.

1 Introduction

One of the mechanically most demanding tasks of daily activities is the human sit-to-stand (STS) movement (see fig. 1.1), which is “defined as the process of rising from a chair to a standing up position without losing stability balance” [12]. Generally accepted as a prerequisite for gait and other functional abilities it has a huge impact on the quality of life, especially for people that can not accomplish normal STS transfer due to physical restrictions such as disabilities, neurological or musculoskeletal disorders, injuries or advanced age.

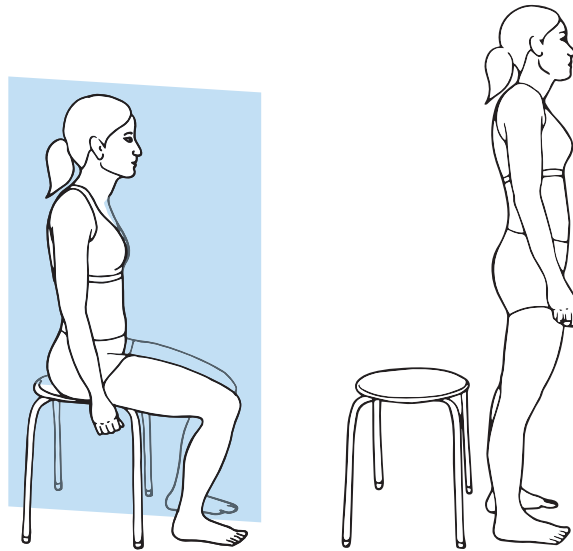


Figure 1.1: Sit-to-stand motion within sagittal plane (depicted in blue).

In order to predict movement strategies, study cause and effect and forecast the joint torques, that are high in comparison to other human motions, STS is worthy of being studied through mathematical models that predict the kinematics and dynamics of a human body [12, 22, 84, 91, 98]. Predictive methods have the advantage over experiments, that they are faster and not cumbersome. Among others they are mostly developed in order to help with subject-specific exoskeleton design or design of assistive devices in rehabilitation robotics [22, 28, 35, 69, 70, 99, 116].

The human body itself is usually represented by a skeletal model, i.e. an articulated multilink system that is driven by torques at revolute joints. The number of links and degrees of freedom (DOFs) of the model depend on the dimension of the workspace in which the system is moving (2D or 3D) as well as on the aim of the study. In case of a planar model, the biomechanical system is restricted to the sagittal plane and fre-

quently assumed to be symmetrical. Three links representing the shanks, thighs and upper body including the head, arms and trunk (HAT) form the simplest model with three DOFs, where feet are sometimes added as an additional link fixed to the ground, not affecting the number of DOFs. In order to consider the arms' swing, a six-link model with five DOFs can be used consisting of foot, shank, thigh, torso, upper and lower arm. A more realistic modeling approach is pursued through spatial models of five or more links of different numbers of DOFs. Asymmetrical motion can be thereby examined [12]. Occasionally, musculoskeletal systems that include computational muscle modeling are used in the field of biomechanics in order to account for neuromuscular dynamics and control including muscle strength limits, muscle contraction and activation delays [14, 15, 30, 53]. However, the inclusion of muscles can be rarely found in the models regarding STS simulations [81, 88].

Over the last decades, broad research has been conducted in the field of motion prediction in biomechanics in general [13, 18, 31, 68, 90, 103, 111]. In contrast, only limited studies concentrate on STS forward simulations (a literature review on STS motion prediction is given in section 1.1). STS in particular was studied extensively on a biomechanical level through experimental studies in order to analyze chair, subject and strategy-related factors [34] that influence STS motion performance such as chair height [2, 37, 95], arm support or use of hand force [2, 6, 102], muscle strength [25, 63], age [19, 71, 85, 86], pregnancy [23, 64], physiological status [63], speed [25, 63, 85, 86, 89], balance or postural stability [19, 63, 71, 85, 94], body configuration [89, 102] and foot position [24, 37, 56, 95] etc. The differences of STS-strategies in normal and obese or impaired subjects was studied extensively as well [3, 10, 106].

Despite descriptive analyses of STS, normative studies were performed that focus on the phase division of the movement cycle through event markers of STS [58, 59, 100]. Although there is no standardized definition of the STS movement cycle, the basic idea presented by the phases is the same and event marker formulations such as initiation, seat-off or standing on and stabilization are used throughout the literature. Other normative studies define STS with regard to coordination strategies [1, 32]. Hughes et al. [32], for example, characterize rising strategies for elderly people and classify them in "momentum transfer", "stabilization" and "combined" strategies. The former refers to the requirement of sufficient horizontal momentum developed in the trunk in order to transfer the center of mass over the feet, since it does not lie over the base of support during the instable period when the buttocks leaves the chair. Opposed to this strategy, the base of support and center of mass are rearranged before standing within the stabilization strategy in order to rise using very little momentum. A combination

of both strategies can be found in the combined strategy where a repositioning of the body takes place in order to shorten the distance between the center of mass and the feet. In this thesis, the momentum transfer strategy forms the basis for the STS motion transfer within the conducted experiments as well as simulations.

1.1 State of the art

The aim of motion simulation is to generate joint angle profiles on the basis of pre-defined conditions, such as the initial configuration of the system, and to gather information on unmeasurable variables of a biomechanical system, such as joint torques and forces. The problem of motion simulation, however, is undetermined, since infinite many trajectories exist to complete a specific task.

In order to resolve the undetermined problem in STS forward simulation, different methods have been implemented in the literature. Commonly used in STS motion prediction are basically two methods: (a) a control-based motion generation method and (b) an optimization-based motion generation method [12]. Both methods are described in joint space, i.e. the space in which the joint variables \mathbf{q} of a mechanical or in this case biomechanical system are defined.

(a) The **control-based motion generation method** attempts to emulate the neural central system and treats the human body model as a controllable system. It aims at finding required joint torques as input for the human body model in order for the output to carry out a certain behavior. This usually refers to joint angle profiles that need to follow desired trajectories. The desired trajectories can either be gathered through experimental measurements or computed by an auxiliary system. Since the motion is reproduced by tracking reference trajectories, new motions can not be generated. According to Chumacero and Yang [12] two control laws were found within this method, (i) the tracking control and (ii) the optimal control technique:

- (i) **Tracking control**: This control technique aims at finding a torque vector $\mathbf{\Gamma}(t)$ such that the joint angle trajectories $\mathbf{q}(t)$ track desired joint angle trajectories $\mathbf{q}^*(t)$.
- (ii) **Optimal control**: In order to operate the dynamic human system such that some optimality criterion is achieved, an objective function of state and

control variables is optimized. In STS motion simulation, the control strategy typically employs a linear-quadratic regulator (LQR). First, a negative feedback controller compares the measured output $\mathbf{q}(t)$ to a reference signal $\mathbf{q}^*(t)$ and generates a stabilizing input torque vector $\mathbf{\Gamma}(t)$ for a system that is linearized at an operating point. The stabilizing input then is used in the LQR which minimizes a cost function by using the Ricatti equation. The optimal torque vector is thereby generated which serves as input for the human body model and at best drives $\mathbf{q}(t)$ to $\mathbf{q}^*(t)$.

(b) The **optimization-based motion generation method** is based on the assumption that the neural central system takes certain (unknown) performance criteria as a basis in order to perform tasks. Within this modeling approach, human performance measures are used to define one or more cost functions in order to achieve natural human movement. In the literature, several objective functions have been suggested and analyzed, as described below. The approach allows for considering environmental and physiological restrictions of the motion in the form of suitable constraints, for example by limiting the physical space in which the motion is performed. All in all, the algorithm generates optimal joint motion with respect to (w.r.t.) some criteria in consideration of imposed constraints. For this, joint angle and velocity trajectories are used by the equations of motion to compute corresponding torques $\mathbf{\Gamma}(t)$. The torques are then used by the cost function to evaluate the solution. If the constraints are not fulfilled and/or the solution is not optimal with regard to the minimized cost function, new trajectories are generated and the process starts over.

Finding suitable **human performance measures** in STS remains an open challenge and depends on the motion to be performed. Most widely used as a cost function f is the *minimum torque* or *minimum effort*

$$f = \int_{t_0}^{t_f} \mathbf{\Gamma}(t)^T \mathbf{\Gamma}(t) dt$$

with t_0 and t_f being the start and finish time of integration. This cost function considers the dynamics of the motion.

Among others, minimizing the *kinetic energy cost* represents another cost function

$$f = \int_{t_0}^{t_f} \dot{\mathbf{q}}(t)^T \dot{\mathbf{q}}(t) dt$$

which addresses the energy consumption while planning the trajectory $\mathbf{q}(t)$.

An alternate performance criterion found in STS is the *generated power* for each

joint n to be used in a cost function

$$f = \int_{t_0}^{t_f} \sum (\mathbf{\Gamma}_n(t) \dot{\mathbf{q}}_n(t))^2 dt$$

in order to consider high kinematic changes and input torques.

Also, *minimum torque change* can be used

$$f = \int_{t_0}^{t_f} \dot{\mathbf{\Gamma}}(t)^T \dot{\mathbf{\Gamma}}(t) dt$$

in order to take a maximum motion smoothness into account.

The **constraints** can be classified in physical and physiological restrictions, they also can be time-dependent and time-independent. Physical constraints address environmental issues or the space where the motion is performed such as

- the *chair dimension and position*,
- the *foot contact* ensuring that the feet are in constant contact with the ground,
- the *initial and final position*, so the model moves from a sitting to a standing position, and
- *collision avoidance* in order to avoid self-penetration of the links.

Physiological constraints in particular include

- *joint angle limits*,
- *joint torque limits*,
- *joint strength* and
- *dynamic stability* in order to guarantee for the body not to fall down during motion.

The equation of motion itself represents an equality constraint that always should be fulfilled for the entire motion of the corresponding model. The time-dependent constraints need to be satisfied for the whole duration of the motion under study, while the time-independent constraints are only employed at certain points such as initial and final positions and velocities of joint angles.

To solve the optimization problem numerically and to reduce the search space of the optimal joint angle trajectories from infinite to a few limited numbers, parameterization methods are utilized. Finding the coefficients of a predefined set of base functions then is equivalent to the problem of finding the optimal trajectory. Typically, interpolating functions such as B-splines and movement

elements are used: (a) *B-splines* are basis functions that are piecewise formed of polynomial functions creating smooth curves. They are driven by control points that influence one segment of the curve, respectively, allowing for local control. The order of the polynomials is independent of the number of control points [12]. (b) *Movement elements*, “a kind of physiologically supported basis functions” [98], “refer to the technique where six movement-patterns are linearly combined in order to construct a [smooth] trajectory that minimizes the joint angle jerk” [12].

To overcome the downside of the optimal control approach, which is the need for joint trajectory reference and the inability of generating different motions, the optimization-based method was applied more frequently. However, according to Chumacero-Polanco and Yang [12] no single cost function predicts good natural STS motion, but a multi-objective cost function leads to better results. The combination of different performance measures then again is crucial, since they behave differently in comparison with different combinations among each other. Both approaches imply mathematical formulations and controls in joint space. Joint space control techniques rely on transformations from task specifications to joint space descriptions in order to regulate the task’s corresponding joint space motion.

In this thesis, an alternate method for STS motion generation is proposed which bridges the gap between the space where tasks are defined and the space in which the control itself is taking place. It is based on the operational space control method that is used in robotics since 1980.

In the following, an overview on the literature on control-based and optimization-based STS motion generation methods is given, followed by a description of the state-of-the-art of operational space control methods focusing on applications in humanoid robotics and biomechanics.

1.1.1 Literature review on the control-based method

A **tracking controller** within the control-based motion generation method was firstly used in 1978 by Hemami and Jaswa [27] on a planar three-link nonlinear inverted pendulum model to reproduce human STS motion. The nonlinear model was linearized along joint trajectories in order to utilize mode feedback. Open-loop joint torques were derived from experimental measurements as reference and feedback torques were

calculated based on the sensed angles and their rates. The supportive effects of the chair while sitting were not considered.

Optimal control is used more often, for example by Wang et al. [113] to quantitatively identify the optimal trajectories in order to reduce body loads. Within the optimal control approach they used an optimization algorithm that minimizes the moments and torque powers of all joints. Their nonlinear planar four-link model was linearized at the sitting position.

Mughal and Iqbal have extensively researched the simulation of STS-maneuvers through the optimal control approach. Only some of their work is mentioned in the following overview. In [72] and [73] the authors use a four-link model in the sagittal plane with joint angles at ankle, knee and hip that is linearized at standing and sitting positions. For both local linear systems, linear fuzzy models are designed in combination with a fuzzy optimal control technique based on an H_2 linear quadratic regulator. The models are merged to one system through membership functions that incorporate if-then rules based on the knee angle changes since all other angles w.r.t. the horizontal remain the same. The control input are the torques generated at ankle, knee and hip that are regulated through feedback states. Later on, the authors extended their approach in [74] by using physiological variables, namely the center of mass and ground reaction forces, to base their weighted cost function on that minimizes the errors of the states. LQR is used where the weights are based upon the physiological variables to compute feedback components of the joint torques. Reference trajectories for all joint angles are included in order to generate feedforward components of joint torques. Total net torques are then gathered by the sum of feedforward and feedback components. Physiological latencies, i.e. time-delays of information that is sent through the central nervous system to the brain, are introduced by Rasool, Mughal and Iqbal in [93] to the model and physiological cost optimization used in [74]. Furthermore, they employ a three-dimensional, eight segmented model with seven joints in some of their research works [76, 79, 75, 77, 78]. In [75], for example, the model is linearized only at the standing position. A decoupled optimal controller design is focused on where one foot is connected to the ground by a weld joint and holonomic constraints are imposed on the other one. Control input torques are regulated through an H_2 -LQR regarding the constrained subsystem of the foot position while the system of unconstrained joint angles is driven by an H_∞ -LQR. Arbitrary reference trajectories are used at first to satisfy stable STS-transfer. These reference angular profiles are synthesized on a physiological basis in [77]. In [79], a decoupling takes place with regard to the separation of frontal and sagittal variables, claiming to yield better results than in [76]. However, torques

converge to zero.

1.1.2 Literature review on the optimization-based method

Sadeghi et al. [98] have researched the idea that the central nervous system might use different strategies while performing a complex task. That is why they make use of different cost functions for each phase of the STS-movement of their four-link three DOF skeletal model in the sagittal plane. In phase one of their multi-phase cost model, they use the minimization of generated power in the ankle and knee joint, in phase two the minimization of the torques are of interest whereas in phase three the minimization of kinetic energy is employed. All three cost functions are combined through the weighted sum of individual cost functions. In their approach, torque limits as well as dynamic stability are implemented as task-independent constraints. For parameterizing the search space, movement elements are employed in order to generate the corresponding joint angle, velocity and acceleration trajectories of ankle, knee and hip. In total 18 parameters are optimized. According to them, the results predict the STS motion sufficiently accurately and show a potential flexibility to distinguish between movement strategies of different subjects.

With the aim of developing a three-dimensional unassisted STS motion prediction formulation for healthy young adults, Ozsoy and Yang [84] use a multi-objective cost function of dynamic effort and difference of left and right vertical ground reaction forces. Several constraints are employed including joint angle limits, foot contacts, chair height and contact, stability, initial and final postures as well as joint angular velocities and accelerations, and stage durations. For an optimization of 171 parameters, the parameterization is accomplished through quadratic B-splines of fifth order, where the duration of the motion is given as an input. The results predict slightly asymmetrical STS motion for the nine-link spatial model of lower limbs and trunk and 21 DOFs. They followed up on their three-dimensional unassisted STS motion prediction method in 2019 [116] in order to forecast STS motion for elderly individuals by giving a longer duration of motion as input. The results are indirectly validated through results of experiments in the literature and show that differences between young and old appear most commonly with regard to the duration of reaching the trunk flexion peak in the sagittal plane.

Geravand, Korondi and Peer [22] formulate unassisted and assisted STS transfer as an optimal feedback control problem to generate optimal trajectories for a six-link sagittal

model of five DOFs. The cost function is defined as a combination of minimum effort in a sense of minimum time response, minimum torque change, minimum jerk as well as human balance and task end-point accuracy. The physical control constraints of torque limitations are considered. For the unassisted case, seven weighting matrices, incorporated within the cost functions, are specified and ten joint parameters have to be optimized. The results are evaluated for different healthy subjects by comparison of simulations and experimental data from the instance of seat-off, since no chair support effects are considered in the simulations. Acceptable model accuracy is obtained.

Another multi-objective cost function was used by Kuželíčki et al. [60] within dynamic optimization. Minimum effort and minimum jerk are used as cost functions for the five-link three-dimensional model in the sagittal plane, whereas the minimum difference between left and right ground reaction forces is used to assure symmetry of motion. As constraints joint angle limits and initial and final positions are applied. The parameterization is executed through B-splines, where 65 control point parameters are optimized [12, 22].

Yamasaki, Kambara and Koike [115] hypothesize that motion of the center of mass is optimized. They use dynamic optimization to examine whether minimum jerk or minimum torque change might be responsible for generating an upright, a natural or a leaning-forward strategy of STS-movement using a three-link sagittal model. The trajectory optimization of the center of mass is solved as a two-point boundary value problem of a set of nonlinear ordinary differential equations. Trajectories after seat-off are successfully reproduced by the minimum torque change model in all three patterns.

Expanding on Garner's master's thesis [20], Pandy, Garner and Anderson [88] use an optimal control approach on a planar three-segment musculoskeletal model that is actuated by eight musculotendinous units. In order to understand how muscles coordinate body segment motions, different performance criteria based on muscle force are evaluated within their study. They convert the optimal control problem into a parameter optimization problem where neural excitations to each muscle are modeled using linearly interpolated nodes. They conclude that incorporating the minimization of muscle forces only during contact with the chair until seat-off in combination with the time derivative of muscle force for the time between seat-off and termination leads to good agreement with regard to experiment results. Also, they find that, for multi-joint coordination, motion constraints play an important role next to performance criteria. Considered constraints are terminal segment positions, static equilibrium for the standing position and limits to the neural excitation signal.

In her dissertation, Norman-Gerum [81] provides an iterative dynamic optimization approach for the motion prediction routine of STS that is build on the hypothesis that healthy humans prioritize mechanical efficiency in motion. At first, a three-link planar model with an integrated buttocks model is used and candidate STS trajectories of the hip joint center are described by Bézier curves. Joint torques as well as the physical infeasibility including slipping and falling are minimized in the cost function. Motion patterns are compared to literature normative data concluding that STS motion predictions seem reasonable. Following, a musculoskeletal geometry was included by extending the model by 10 muscles. The optimal control strategy was recast by adding the minimization of muscle stresses to the former cost function. Resulting simulations again are supposed to produce characteristic STS motion patterns. A detailed description of this method disregarding the muscle model can be found in chapter 6 of this thesis.

In the field of mobility assistance robots for STS support, related research is conducted by Geravand et al. [22], Mombaur [70], Mombaur and Khai-Long Ho [28, 69] or Saint-Bauzel et al. [99], just to mention a few. In [70] best possible external support is focalized and determined by a simulation-based optimal control approach to predict STS motions of geriatric patients using an eight DOF model in the sagittal plane with geriatric segment parameters and a chair of standard 45 *cm* height. The weighted combination of several cost functions is pursued by the minimization of joint torques squared, minimization of mechanical work in all joints, minimization of angular velocity of the head and a regularization term to smoothen external forces. A variety of constraints such as bounds on joint angles, angular velocities, forces and torques, external forces, starting and end conditions as well as considerations of contacts are included. The solution approach is based on a direct multiple shooting technique and yields position and velocity histories of joint torques and external forces including their moving points of applications. Generated motions were evaluated by clinical partners and verified to be similar to realistic geriatric STS motion transfer.

1.1.3 Literature review on the operational space control method

The **operational space control method** treats the motion control directly in operational space, i.e. the space in which the task is defined and end-effector trajectories are tracked. Opposed to joint space control techniques, control characteristics like error, performance, dynamics and controlled variables are thereby associated with the task [43, 49].

Analogous to joint space control systems, the operational space control covers a variety of control approaches and can be handled at inverse kinematics [26, 29, 65, 80, 108] or dynamic level [40, 43, 45, 51]. A well-known approach on dynamic level is based on the operational space formulation that was established by Oussama Khatib and for the first time formalized in his dissertation in 1980 [39]. Here and in his further work, he deduced a mathematical description of a dynamic model of the manipulator end-effector in operational space. The fundamental idea of the approach is to control end-effector motion and force through utilizing the forces directly produced at the end-effector, which are generated through corresponding torques and forces applied at the manipulator joints [52, 49, 107]. Additionally, the command can be extended in order to achieve a desired posture in the null space of the task. The purpose of the development of this method was the requirement of a precise control of end-effector motion and applied end-effector forces for serial manipulators in order to attain high accuracy and performance in precision tasks, like assembly operations or welding of parts. The advantages not only lie in attaining precise and simultaneous control of end-effector motion and active forces, but also in sparing a time-consuming transformation of the end-effector path from a Cartesian description into joint trajectories [40, 42, 43, 49].

At first, the application of operational space control has been majorly restricted to the field of serial robotics. Over the years, the operational space formulation and control was extended to the real-time control in the presence of obstacles and constraints [41]. Mobile robots were included in experiments [55, 96, 97] and the operational space formulation was modified to be compatible with complex branching (tree-like) redundant mechanisms as well as combined parallel and serial mechanical structures such as macro-/mini-manipulator systems and multi-effector manipulators [8, 9, 33, 44, 45, 46, 47, 49].

Soon came the application of the approach for humanoid robots in dynamic environments through mapping human behavior on robots. Since human motion is characterized by performing several tasks simultaneously and hierarchically, task descriptions implicate a combination of coordinates related to the arms, the legs and the torso etc., while the remaining motion freedom concerns robot posture as well as internal and external constraints. Thus, the focus lay on combining motion planning and control methods in a task-oriented approach, where the aim was to generate desired motion behavior that simultaneously does not interfere with the execution of the task [5]. In this context, an explicit specification to manipulator task and posture control within task and posture space, respectively, was derived, that guarantees posture behavior to be performed without projecting any acceleration onto the task [5, 54]. Khatib et al.

simulated and validated their method on multiple experiments such as maintaining a specified hand position of the humanoid robot's simulation while its elbow oscillates in a predefined manner. Sentis and Khatib, extended the method to control whole-body behaviors in humanoid systems with regard to simultaneously fulfilling multiple tasks under prioritization considerations [104, 105]. They employed their approach exemplarily on the interactive hand position control of a humanoid robot simulation under joint limit constraints and on compliant tasks such as self-balance while maintaining an upright posture and hand position control.

Still focusing on reproducing human movement within robotic environments but one step closer to the field of biomechanics, the prioritized control approach was used to reconstruct human motion from experimental motion capture data by directly controlling marker trajectories [15, 16, 53]. Usually, raw marker positions in Cartesian space are post-processed into joint angle, angular velocity and acceleration trajectories in joint space using inverse kinematics calculations and then solved for the human dynamics. Those steps are replaced by the task space reconstruction algorithm that obviates the transformation into joint space and overcomes motion sensing errors and computationally costly processes. Demircan et al. tracked marker positions of tai chi movements [16] and of a throwing motion [15] in a prioritized manner using the operational space control method in order to drive a simulated scaled kinematic human model to those marker locations and to extract joint angles in real-time. Khatib et al. used direct marker control in [53] in order to synthesize human motion. A posture-based muscular effort minimization criterion was introduced on a musculoskeletal model and validated on motion capture experiments of upper limb reaching tasks. A generalized effort minimization criterion was then implemented in order to analyze the throwing motion of a football player which was examined through motion capture experiments. Results of the analysis for the dynamic characterization of the human motion procedure confirmed their hypothesis that humans “tend to minimize the muscular effort while following the lines of maximum feasible accelerations when performing a task” [53].

Within the field of biomechanics the operational space framework had limited application. Thelen and Anderson [110] used the operational space method for the generation of forward dynamic simulations of three-dimensional normal gait on a 20 DOF, torque driven model. Using the feet as end-effectors within the approach, optimal trajectories of the feet were first computed through nonlinear constrained optimization in order to be consistent with experimentally recorded ground reaction forces. The foot tracking task was enhanced through tracking measured joint angle displacements of the lower extremities in order to solve redundancy problems and avoid penetration of the feet

into and sliding on the ground. Although self-balancing of whole-body movements could not be accomplished with this method, after 30 minutes of computation time results were generated that indicated similarities of joint torque shapes and magnitude between simulation and inverse dynamics computations.

De Sapio et al. [14] presented a general task-level control framework with an extension of the application to biomechanical systems. In order to control muscles, musculoskeletal parameters were embedded into the postural field. Unlike dynamic optimizations with feedforward approaches, the framework is characterized through stable response to external disruptions due to its feedback nature. Apart from this, a simulation structure for the generation of physiological musculoskeletal simulations was described.

Based on experimental results of moving the hand to a target under disturbances, Mistry and Schaal [67] hypothesized that a task-space control mechanism underlies human motion behavior and is therefore used by the nervous system. Built upon Khatib's formulation of operational space control, they presented an operational space approach for the whole-body control of underactuated and constrained systems. They employed the Moore-Penrose pseudo-inverse of the Jacobian matrix and a modification of the null space motion component in order to compensate for redundancies and resolve underactuation.

To the author's knowledge, the concept of using operational space control in the biomechanical field of a STS motion has so far only been utilized once by Barthélemy et al. in 2006 [4]. For reference, STS measurements were conducted using a *Vicon* motion capture system including a posturographic force platform for the recording of ground reaction forces. The experimental setup included test subjects sitting in a static comfortable position on an armless and backless chair of 0.45 m height with arms crossed on the chest. Subjects were asked not to move their feet during their motion in self chosen speed. For motion reconstruction of the recorded data and for performing simulations, they made use of a 3R planar biomechanical model provided by the Humanoid Motion Analysis and Simulation (HuMANs) toolbox developed at INRIA-Grenoble. As a control scheme for predicting STS motion they implemented a combination of operational control and optimal control through quadratic minimization under linear constraints. The constraints refer to the contact between feet and ground and to the contact between chair and subject which was modeled as a single, non sliding contact point at the hip. The task space was chosen to be a combination of the angular acceleration of the model's center of mass and of the vertical head position called \ddot{x}_1 and \ddot{x}_2 , respectively.

The objective function was defined as minimizing the norm of the acceleration energy

$$\text{minimize } (\ddot{x}_{id} - \ddot{x}_i)^T \mathbf{\Lambda}_{ri} (\ddot{x}_{id} - \ddot{x}_i), i = 1, 2$$

with \ddot{x}_{id} being the desired acceleration and $\mathbf{\Lambda}_{ri}$ being the inertia matrix in task space. A hierarchy structure was added by projecting joint accelerations on the null space of the first task's Jacobian matrix using a projector matrix \mathbf{P}_1 in order to avoid interference of the second task with the first one. Furthermore the acceleration energy, projected on the second task space through \mathbf{P}_2 , was minimized in order to have a unique solution of the overall minimization problem. To handle singularities, singular value decomposition of $\mathbf{\Lambda}_{ri}^{-1}$ was used to compute $\mathbf{\Lambda}_{ri}$ and \mathbf{P}_i . Simulation results, however, are missing in this paper. It also lacks statements of citations to the literature. A complete version of this paper could not be found.

1.2 Introductory example

Inspired by Hemami and Jaswa [27] a control based method premised on a PD controller using state feedback by pole placement was implemented for a three-link nonlinear inverted pendulum model in the sagittal plane as a first attempt to simulate human STS motion. Herewith, control gains are selected such that all eigenvalues are assigned in the left half of the complex plane to achieve asymptotic stability.

The model's segments represent both shanks, both thighs and the HAT as one entity, respectively, with masses and lengths based on measurement data and calculations described in chapter 3. For the sake of simplicity, segment centers of masses S_i , $i = 1, 2, 3$, are placed in the middle of each link as shown in fig. 1.2. Joint angles q_1 , q_2 and q_3 for ankle, knee and hip, respectively, are described w.r.t. y -axis of the base frame \mathcal{K}_0 , that is situated in the ankle joint. Without considerations of the supporting forces of the chair while sitting, the model is driven by torque actuators at the joints.

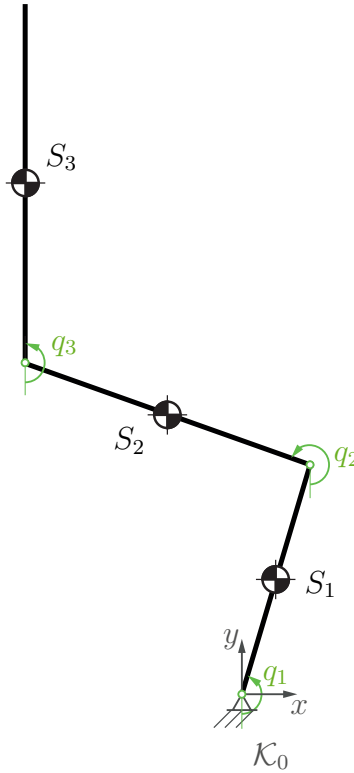


Figure 1.2: Triple pendulum model used for control of STS-motion by pole placement

For incorporating the method of pole placement, the system is linearized about the operating point corresponding to the vertical stand. System dynamics of the linearized system are described in state space representation with $n = 6$ state variables, $p = 3$ inputs and $q = 6$ outputs:

$$\begin{aligned}\dot{\tilde{\mathbf{x}}}(t) &= \mathbf{A}\tilde{\mathbf{x}}(t) + \mathbf{B}\tilde{\mathbf{u}}(t) \\ \tilde{\mathbf{y}}(t) &= \mathbf{C}\tilde{\mathbf{x}}(t),\end{aligned}$$

where $\tilde{\mathbf{x}} = [q_1, \dot{q}_1, q_2, \dot{q}_2, q_3, \dot{q}_3]^T$, $\tilde{\mathbf{x}} \in \mathbb{R}^n$, is the state vector containing joint angles and angular rates, \mathbf{A} of dimension $n \times n$ is the state matrix, \mathbf{B} of dimension $n \times p$ is the input matrix, $\tilde{\mathbf{y}} \in \mathbb{R}^q$ is the output vector and \mathbf{C} of dimension $q \times n$ is the output matrix which, in this case, is the identity matrix $\mathbf{I}_{6 \times 6}$. The control law is $\tilde{\mathbf{u}} = -\mathbf{K}\tilde{\mathbf{x}}$, $\tilde{\mathbf{u}} \in \mathbb{R}^p$, with gain matrix \mathbf{K} of dimension $p \times n$.

In order to achieve asymptotic stability of the linearized system, control gains \mathbf{K} are selected such that all poles $\bar{\lambda}_j$, $j = 1, \dots, 6$ are assigned in the left half of the complex plane with

$$\begin{aligned}
\bar{\lambda}_1 &= v_1 + v_4 \cdot i \\
\bar{\lambda}_2 &= v_1 - v_4 \cdot i \\
\bar{\lambda}_3 &= v_2 + v_5 \cdot i \\
&\vdots \\
\bar{\lambda}_6 &= v_3 + v_6 \cdot i
\end{aligned}$$

and $\mathbf{v} = [v_1, v_2, \dots, v_6]^T$. The control parameters of \mathcal{K} can be obtained, for example, by solving the determinant $\det(\tilde{s}\mathcal{I} - (\mathcal{A} - \mathcal{B}\mathcal{K}))$ through equating it with the polynomial of desired poles for the characteristic polynomial of the closed loop system and subsequently comparing the coefficients:

$$\det(\tilde{s}\mathcal{I} - (\mathcal{A} - \mathcal{B}\mathcal{K})) = (\tilde{s} - \bar{\lambda}_1)(\tilde{s} - \bar{\lambda}_2) \dots (\tilde{s} - \bar{\lambda}_6).$$

Since no information on the physiological location of the poles could be found in the literature, initial values for the poles were set arbitrarily in the left half of the S-plane through the definition of initial values \mathbf{v}_0 . An optimization process then followed, adjusting the poles based on minimizing the weighted sum of the mechanical energy of each joint. To limit the solution space, the real and imaginary parts v_j of the poles are restricted to the interval $-50.0 \leq v_j \leq -0.01$ in order for the poles to guarantee stability of the system. The restriction regarding the maximum negative value is thereby based on the tradeoff between limiting the control effort and sufficiently dampening the modes. The cost function $f(\mathbf{v})$ then is

$$\begin{aligned}
&\underset{f(\mathbf{v})}{\text{minimize}} & f(\mathbf{v}) &= \sum_{i=1}^3 \tilde{w}_i \cdot \int_{t_0}^{t_f} |\dot{q}_i(t)\Gamma_i(t)| dt \\
&\text{subject to} & & -50.0 \leq v_j \leq -0.01
\end{aligned}$$

where \tilde{w}_i are the weighting factors, $\Gamma_i(t)$ are the joint torques, t_0 is the initial time and t_f is the end of the STS motion. The motion in terms of angles, angular velocities and angular accelerations are obtained through direct dynamics calculations with joint torques as inputs:

$$\tilde{\mathbf{u}} = \mathbf{\Gamma}.$$

The process is iterated with the new values of \mathbf{v} as input to the optimization scheme until the solution $f(\mathbf{v}^*)$ converges. An illustration of the described optimization process can be found in fig. 1.3.

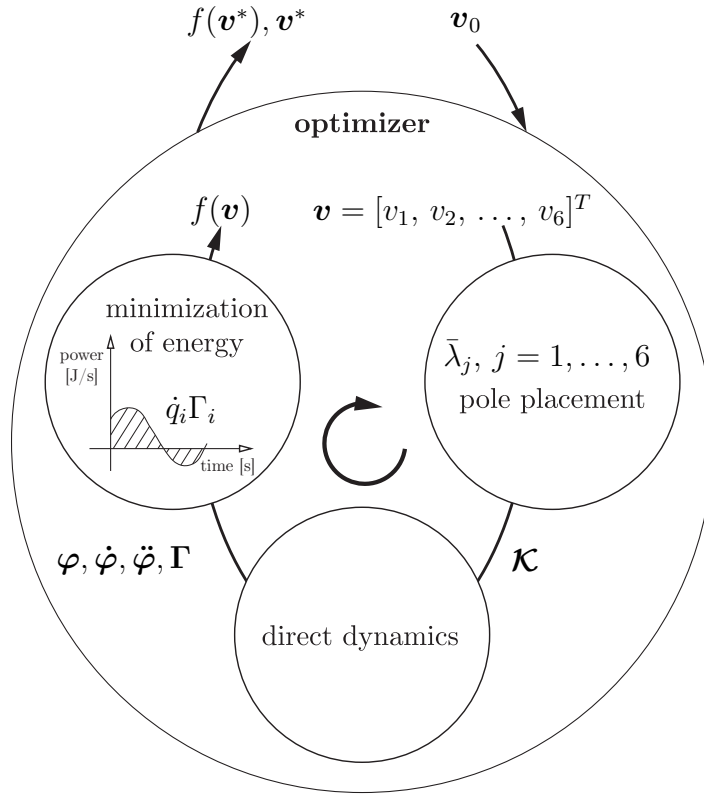


Figure 1.3: Schematic of optimization of pole placement.

On the basis of initial poles chosen to be

$$\bar{\lambda}_0 = \begin{bmatrix} -40.0 - 3.0i \\ -40.0 + 3.0i \\ -35.0 - 2.0i \\ -35.0 + 2.0i \\ -30.0 - 5.0i \\ -30.0 + 5.0i \end{bmatrix}$$

and weighting factors $\tilde{w}_1 = 7.0$, $\tilde{w}_2 = 5.0$ and $\tilde{w}_3 = 3.0$ the optimizer calculated the new poles

$$\bar{\lambda} = \begin{bmatrix} -39.0433 - 0.0102i \\ -39.0433 + 0.0102i \\ -29.7170 - 0.0143i \\ -29.7170 + 0.0143i \\ -2.0411 - 1.5366i \\ -2.0411 + 1.5366i \end{bmatrix}$$

corresponding to the gain matrix

$$\mathcal{K} = \begin{bmatrix} 859 & 499 & 1063 & 577 & 14500 & 863 \\ 204 & 422 & 1264 & 549 & 14507 & 864 \\ 2 & 6 & 11 & 8 & 303 & 18 \end{bmatrix}.$$

The highest weighting value was given to w_1 in order to restrict the motion in the ankle the most while more freedom to the movement of the upper body was considered through choosing a smaller value w_3 for the hip.

Finally, the real and imaginary parts \mathbf{v}^* composing the poles were used within the direct dynamics calculations of the nonlinear triple pendulum model in order to predict STS motion. Corresponding simulation results are shown in fig. 1.4 as a sequence of snapshots.

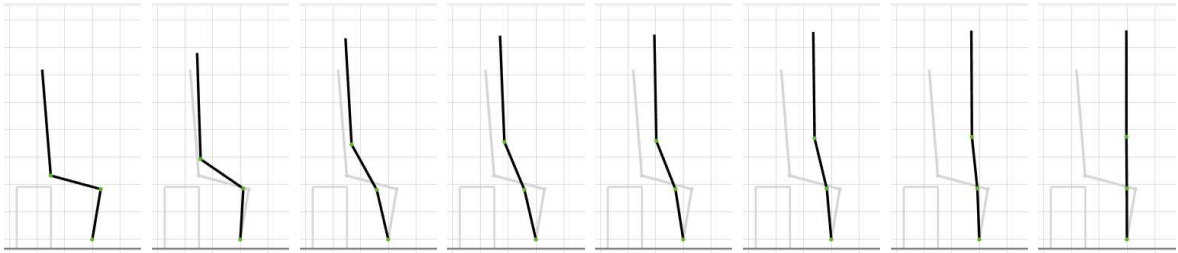


Figure 1.4: Simulation sequence of STS motion using the control based motion generation method of state feedback by pole placement.

Further information on the computation routine as well as on simulation results with regard to cost function values $f(\mathbf{v}^*)$, joint angles and joint torque histories before and after the optimization process can be found in appendix A. Results indicate that lifting the pendulum from a sitting to a stable standing position is possible driving the joint torques. However, a STS transfer that resembles human motion cannot be predicted solely using predefined weighting factors and the minimization of joint energies within the proposed optimization process. The method of pole placement itself might not be expedient at all, but this cannot be concluded definitely at this point, since a simplified model without physiological locations of segment centers of masses or supporting contact forces of the chair was considered. Still, this approach shows an example of controlling the STS motion in joint space and outlines the complexity of control processes underlying human STS motion, that herewith could not be fully grasped.

1.3 Motivation and objective

The STS motion in particular has a huge impact on the quality of life since it is a common, required and complex sensorimotor process. The major challenge in STS is the problem of seat-off. When the point of support during sitting is lost, the projection of the center of mass lies behind the base of support which makes the system statically unstable. Forward trunk flexion then generates momentum to complete the task, but it requires precise control in order not to lose balance. Accomplishing STS motion can be demanding due to reduced abilities in terms of physical or cognitive limitations. Maintaining or re-establishing this skill in its absence is crucial to positively influence one's well-being and mobility and to decrease the risk of falling. Here, STS motion prediction comes into play. Anticipating this movement accurately is essential with regard to many applications such as the design of prostheses, exoskeletons or (wearable) robotic devices for STS assistance in ergonomical engineering, rehabilitation and treatment planning within the medical field, the animation of articulated figures in computer-graphics as well as the design and control of humanoid robots, just to mention a few. To be able to understand how patients would adapt their motion due to a treatment or a training, one must first be able to predict the motion of a healthy subject.

Research in STS motion prediction is rare and has focused on developing direct dynamics strategies in joint space. The control-based introductory example has shown that regulating an inverse pendulum is relatively simple by driving the torques, but generating a human STS postural behavior while getting up from the chair can not easily be attained. In optimization-based motion generation methods, the difficulty comprises finding suitable performance measures or combinations as well as constraints for the specific motion. All in all, defining joint trajectories does not prove to be practical in order to specify a task due to the kinematic redundancy of anthropoid models [5].

By contrast, operational space control methods have proven to be a promising approach for regulating multibody systems since they yield task end-point accuracy in the field of robotics and auspicious results in biomechanics in general. It has so far only been used once in STS motion prediction. This leads to the demand for examining healthy STS motion prediction using an operational space control technique in order to utilize the advantages, that are among others: (i) real-time motion control, (ii) sparing time-consuming transformations from known task related descriptions into joint space and (iii) employing null space motion for postural control in order to make use of complex internal dynamics instead of regarding redundancies as a problem.

The objective of this thesis is to test the hypothesis that the task space control of human motion is more reflective of how the nervous system controls movement and more accurate than joint space control, assuming that joint torques might not actively be regulated in order to perform a desired task. To this end, the applicability of the operational space control method is implemented for the example of the human STS motion by the use of a desired head trajectory for a biomechanical four-link skeletal model in the sagittal plane as an extension to the most commonly used three-link planar model. Furthermore, finding the fundamental objective that is processed by the neural system and that underlies the specific motion comprises an optimization problem in itself. In operational space control, this is characterized by finding a suitable pseudo-inverse of the Jacobian matrix. Testing a set of different pseudo-inverses is undertaken in this work in order to gain a deeper understanding of how the subconscious control strategy of the postural system functions to complete the STS task. At the same time, the thesis aims at gathering information on unmeasurable variables of the biomechanical system, i.e. the joint torques.

1.4 Overview

The remaining part of this thesis is organized as follows: Chapter **2** gives an overview on the background of the kinematics and dynamics as well as on the notation utilized in this work. Within the kinematics section, it gives a definition of joint space and operational (task) space and depicts the relationship between those two spaces. The fundamental phenomena of kinematic singularities and redundancies are addressed along with redundancy resolution techniques on direct and inverse kinematics level which are accomplished through the employment of null space motion. Thereafter the basics of inverse and direct dynamics are briefly presented. The correlation of joint and task space on force level is introduced analogously to the motion level.

In chapter **3** conducted STS measurements are described in detail, serving as reference data to human STS motion reconstruction. A biomechanical four-link model is then portrayed including its measurement-based anthropometry derivation and the transmission of measurement-based orientation data. The mathematical formulation of the model dynamics is given based on the introduction of a proposed buttocks contact force model, its assumptions and a corresponding brief literature overview. In what follows is an in-depth presentation on the implementation of two different buttocks contact force models. First, a literature based Kelvin-Voigt approach, that is adapted

to the employed biomechanical model, attempts to reconstruct the measured vertical and horizontal forces. After that, the results of a newly developed Gaussian function model are delineated. Both approaches are compared and weighted up, with the outcome that the Gaussian function model is implemented in the subsequent simulation framework.

Chapter 4 describes the operational space formulation. The difference of direct and inverse dynamics in operational space with respect to joint space is expanded, focusing on existing solution approaches for redundancy handling, on the basis of which the control method is derived. Task and posture decomposition are clarified and the overall control law is deduced at acceleration and force level. Specifics of the application of the proposed method to the four-link model are given hereafter. Implemented pseudo-inverses are presented, while three different pseudo-inverses of the Jacobian matrix are outlined for testing within the posture control framework for the STS motion.

Simulation results are presented in chapter 5, structured in two approaches regarding a variation of command variables at task level. Within each approach, the aforementioned testing of pseudo-inverses at posture level is shown first. Being based on the decision of which pseudo-inverse yields the most accurate results regarding the consistency with reference joint angles, corresponding STS performance predictions are illustrated hereafter. This includes the results for joint angles, angular velocities, angular accelerations, the end-effector position and orientation as well as corresponding velocities and accelerations, joint torques and all in all corresponding errors w.r.t. reference data in order to validate the approaches. Each section closes with a discussion that includes a simulation sequence as a series of snapshots.

The following chapter 6 contrasts the proposed operational space control method with a recent optimization-based motion generation technique. To that end, the reference method is described briefly. Then a comparison is performed through an implementation for the proposed four-link model.

Finally, a summary including contributions as well as limitations and an outlook for future work is given in chapter 7.

2 Kinematical and dynamical basics

2.1 Kinematics of serial manipulators

The mathematical basis for the description of the motion of the human body without considering the influence of forces and moments is formed by the kinematical framework of serial manipulators, since the human body is usually modeled as an open kinematic chain. Such a mechanism consists of $n + 1$, $n \in \mathbb{N}$, rigid bodies (including the ground) interconnected through n joints which are responsible for transmitting relative motion between pairs of bodies [38, 107]. The first body is fixed to the ground, which is represented through a base frame \mathcal{K}_0 . The end point of the serial manipulator is referred to as the end-effector and described by a coordinate frame \mathcal{K}_e .

It is assumed that each joint grants a single degree of freedom according to the joint variable q that, in this scenario, represents an angle due to a revolute joint. Therefore, the number of joints constitutes the number of DOFs of the manipulator, which characterizes its mechanical structure and distinctly determines its configuration. In the context of biomechanics the configuration of the human body will be termed posture, which signifies the position and orientation (pose) of all rigid bodies forming the kinematic chain [107].

The vector $\mathbf{q} = [q_1, \dots, q_n]^T$ of n joint variables is defined in the so called joint space, also referred to as configuration space [107]. The manipulator task, conversely, is specified in the operational space or task space. This denotes the space in which the vector of the end-effector pose \mathbf{x}_e is defined. The end-effector pose comprises the configuration of \mathcal{K}_e w.r.t. the reference frame \mathcal{K}_0 in terms of $m \in \mathbb{N}$ inherently independent configuration parameters (with $m \leq n$) which also define the number of end-effector DOFs in free motion operations [42]. These parameters are called operational coordinates and are defined through

$$\mathbf{x}_e = \begin{bmatrix} \mathbf{p}_e \\ \mathbf{\Phi}_e \end{bmatrix}$$

with \mathbf{p}_e describing the end-effector position in terms of a minimal number of, most commonly, Cartesian coordinates. Typically, the end-effector orientation $\mathbf{\Phi}_e$, which refers to the rotation of \mathcal{K}_e w.r.t. \mathcal{K}_0 , is described by an Euler angles triplet $\mathbf{\Phi}_e = (\varphi, \vartheta, \psi)$ [107]. This minimal representation belongs to the special orthonormal group $\text{SO}(3)$ and allows for trajectory generation.

The relationship between joint space and operational space is given through the direct and inverse kinematics (see fig. 2.1) which will be described hereafter.

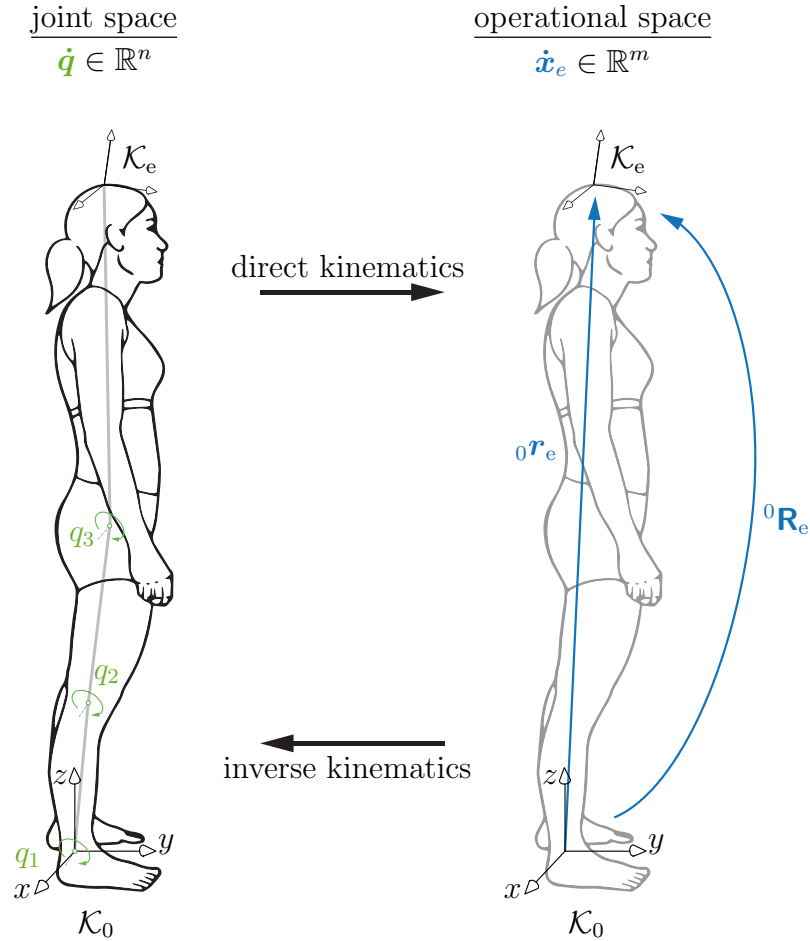


Figure 2.1: Schematic of the direct and inverse kinematics of a human body.

2.1.1 Direct kinematics

Direct kinematics refers to the transmission of joint motion to the motion of the manipulator's end-effector. The aim is to compute the pose of the end-effector, represented by the coordinate frame \mathcal{K}_e , as a function of the joint variables w.r.t. the base frame \mathcal{K}_0 . Thus, the operational variables $\mathbf{x}_e \in \mathbb{R}^m$ can be computed based on the knowledge of the joint space variables $\mathbf{q} \in \mathbb{R}^n$ at position level through a, in general nonlinear, vector function $\mathbf{f} : \mathbb{R}^n \rightarrow \mathbb{R}^m$, formally described by

$$\mathbf{x}_e = \mathbf{f}(\mathbf{q}). \quad (2.1)$$

Through the velocity transmission, one obtains the direct kinematics at velocity level

$$\dot{\mathbf{x}}_e = \mathbf{J}_e(\mathbf{q}) \dot{\mathbf{q}}, \quad (2.2)$$

with the operational space velocity vector $\dot{\mathbf{x}}_e \in \mathbb{R}^m$ collecting the angular velocity of the end-effector frame and the linear velocity of its origin w.r.t. the base frame, and joint space velocities $\dot{\mathbf{q}} \in \mathbb{R}^n$. $\mathbf{J}_e \in \mathbb{R}^{m \times n}$ is the analytical Jacobian matrix

$$\mathbf{J}_e(\mathbf{q}) = \frac{\partial \mathbf{f}}{\partial \mathbf{q}} = \begin{bmatrix} \frac{\partial f_1}{\partial q_1} & \cdots & \frac{\partial f_1}{\partial q_n} \\ \vdots & \ddots & \vdots \\ \frac{\partial f_m}{\partial q_1} & \cdots & \frac{\partial f_m}{\partial q_n} \end{bmatrix},$$

which contains a listing of partial derivatives of the position and orientation components of eq. (2.1) w.r.t. the joint axes. It is a function of the configuration and describes the linear mapping from the joint velocity space to the end-effector velocity space [11, 107].

Differentiating eq. (2.2) again w.r.t. time expresses the direct kinematics at acceleration level

$$\ddot{\mathbf{x}}_e = \mathbf{J}_e(\mathbf{q}) \ddot{\mathbf{q}} + \dot{\mathbf{J}}_e(\mathbf{q}, \dot{\mathbf{q}}) \dot{\mathbf{q}}, \quad (2.3)$$

where $\ddot{\mathbf{x}}_e$ includes the end-effector's angular and linear acceleration and $\ddot{\mathbf{q}}$ contains the joint space accelerations.

2.1.1.1 Kinematic singularities

In general, it is not possible to assign any arbitrary motion to the end-effector, since singular configurations reduce the mobility of a manipulator. Kinematic singularities are configurations at which the Jacobian \mathbf{J}_e is rank-deficient. In this case, the manipulator end-effector can not move anymore in certain directions in Cartesian space or rotate around them. This leads to a temporary loss of one or more DOFs of the manipulator, which are defined by the rank of the Jacobian matrix. In the subspace orthogonal to this singular direction in operational space, manipulator movements remain free. This behavior spreads out over the neighborhood of singular configurations, where small velocities in the operational space already lead to large joint space velocities [107]. Kinematic singularities can be classified in boundary singularities and internal singularities. Whereas boundary singularities occur when the manipulator is completely stretched or entrenched, internal singularities generally arise on account of the alignment of axes of motion within the workspace or due to particular end-effector configurations [107].

2.1.1.2 Kinematic redundancy

Within kinematic calculations, redundancies pose another problem. A kinematic redundancy appears when more DOFs are available than variables to describe a certain task. A manipulator is said to be intrinsically redundant when the dimension of the operational space m is smaller than the dimension of the joint space n . If only a number r of coordinates of the operational space vector, with $r < m$, are of interest to conduct a certain task, but $m = n$, the manipulator is still said to be functionally redundant, meaning that the concept of redundancy is relative to the task that is assigned to the manipulator [107]. The corresponding Jacobian matrix $\mathbf{J} \in \mathbb{R}^{r \times n}$ then describes the instantaneous velocity transmission from the joint velocity space $\dot{\mathbf{q}} \in \mathbb{R}^n$ to the end-effector space of velocities of concern $\dot{\mathbf{x}} \in \mathbb{R}^r$ in order to perform the specific task. Note that the index e is from now on left out to address the general case, where $r \leq m$. If the manipulator is kinematically redundant with $r < n$, there exist $n - r$ redundant DOFs.

Physically speaking, a redundant manipulator can have different postures while maintaining the same end-effector pose which is referred to as internal motion. This is illustrated in fig. 2.2 for the example of a three-link planar manipulator with three joints. For this case, only the position of the origin of the end-effector is of interest.

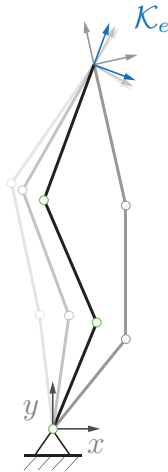


Figure 2.2: Exemplary internal motion (grey) of three-link planar manipulator (black) for a fixed origin of frame \mathcal{K}_e .

Internal motion is characterized by the range $\mathcal{R}(\mathbf{J})$ and null space $\mathcal{N}(\mathbf{J})$ of the mapping described by \mathbf{J} (see appendix B), as illustrated in fig. 2.3, where the Jacobian matrix has to be regarded as constant for a specific posture. Joint velocities $\dot{\mathbf{q}}$ that do not

generate any end-effector velocity in the given manipulator posture lie within the null space of the Jacobian matrix. All other joint velocities produce end-effector velocities $\dot{\mathbf{x}}$ that lie within the range of the Jacobian matrix.

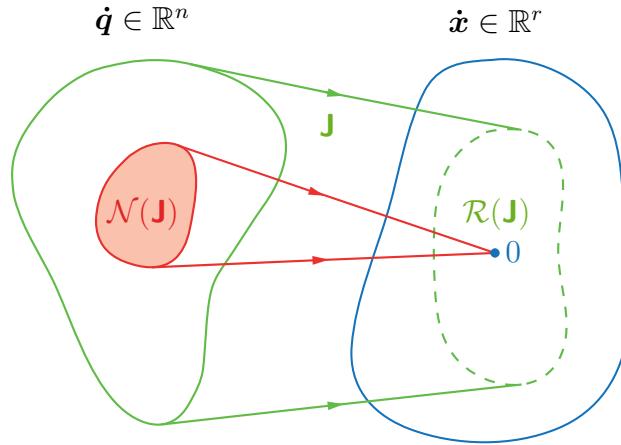


Figure 2.3: Mapping between joint and end-effector space at velocity level, inspired by [107].

If the Jacobian has full rank, the dimension of the null space is $\dim(\mathcal{N}(\mathbf{J})) = n - r$ whereas the dimension of the range space is $\dim(\mathcal{R}(\mathbf{J})) = r$, so the range spans the entire space \mathbb{R}^r . At a singular configuration, the Jacobian degenerates and the dimension of the null space increases while the dimension of the range space decreases, as $\dim(\mathcal{R}(\mathbf{J})) + \dim(\mathcal{N}(\mathbf{J})) = n$, independently of the rank of \mathbf{J} .

2.1.1.3 Redundancy resolution within direct kinematics

Since the null space is $\mathcal{N}(\mathbf{J}) \neq \emptyset$, redundancy resolution techniques can be employed in case of a redundant manipulator, where one can choose any joint velocity vector $\dot{\mathbf{q}}_{\text{any}}$ in order to take advantage of redundant DOFs. The aim is to generate internal joint motions that do not alter the end-effector pose but positively affect the desired motion through influencing the manipulator configuration.

One can choose an $n \times n$ projector matrix \mathbf{P} so that $\mathcal{R}(\mathbf{P}) \equiv \mathcal{N}(\mathbf{J})$ [107]. If $\hat{\mathbf{q}}$ already is a solution to eq. (2.2), then

$$\dot{\mathbf{q}} = \hat{\mathbf{q}} + \mathbf{P}\dot{\mathbf{q}}_{\text{any}} \quad (2.4)$$

represents another solution to eq. (2.2), since

$$\dot{\mathbf{x}} = \mathbf{J}\hat{\mathbf{q}} + \mathbf{J}\mathbf{P}\dot{\mathbf{q}}_{\text{any}} \quad (2.5)$$

given

$$\mathbf{J}\mathbf{P}\dot{\mathbf{q}}_{\text{any}} = \mathbf{0} \quad (2.6)$$

yields

$$\dot{\mathbf{x}} = \mathbf{J}\dot{\mathbf{q}},$$

where the dependence on \mathbf{q} has been omitted for the sake of clarity.

2.1.2 Inverse kinematics

In practical applications it is crucial to be able to specify a desired motion trajectory to the end-effector. On the basis of the given end-effector target position ${}^0\mathbf{r}_e$ and orientation ${}^0\mathbf{R}_e$ the corresponding joint variables need to be determined which is referred to as the inverse kinematics (see fig. 2.1 in chapter 2.1) [101, 107].

At position level, the solution of the inverse kinematics is formally described by

$$\mathbf{q} = \mathbf{f}^{-1}(\mathbf{x}). \quad (2.7)$$

In general, eq. (2.7) is not resolvable in closed-form, for example through algebraic or geometrical solution approaches, due to complex structures of the manipulator or nonlinearities within the relationship between joint space variables and operational space variables. Also, multiple solutions by reasons of redundancy or even infinite solutions because of singularities might exist. Furthermore, unreachable configurations or joint limits might lead to solutions that are not admissible. Numerical solution techniques provide a remedy, since they can be applied to any kinematic structure. However, in general they do not provide all admissible solutions [101, 107].

Usually, the inverse kinematics is handled at velocity level. It is formally described by the inversion of the manipulator Jacobian in order to obtain the joint velocities

$$\dot{\mathbf{q}} = \mathbf{J}^{-1}\dot{\mathbf{x}}. \quad (2.8)$$

Yet eq. (2.8) is only solvable if the Jacobian matrix is square and of full rank, thus regular. Is the manipulator located in a singular configuration or is it redundant to begin with, computing the Jacobian inverse is not feasible any more.

A general solution method is posed by employing a pseudo-inverse of the Jacobian matrix \mathbf{J}^\dagger which satisfies the condition of pseudo-inverses, namely

$$\mathbf{J}\mathbf{J}^\dagger = \mathbf{I}. \quad (2.9)$$

Eq. (2.8) then becomes

$$\dot{\mathbf{q}} = \mathbf{J}^\dagger \dot{\mathbf{x}}, \quad (2.10)$$

which, multiplied by \mathbf{J} from the left, fulfills the direct kinematics equation (eq. (2.2)).

2.1.2.1 Redundancy resolution within inverse kinematics

Facing the redundancy issue ($r < n$), a general solution to the joint velocities based on eq. (2.2), eq. (2.6) and eq. (2.9) is

$$\begin{aligned} \mathbf{J} \dot{\mathbf{q}} &= \dot{\mathbf{x}} \\ \Leftrightarrow \mathbf{J} \dot{\mathbf{q}} &= \mathbf{J} \mathbf{J}^\dagger \dot{\mathbf{x}} + \mathbf{J} \mathbf{P} \dot{\mathbf{q}}_{\text{any}} \\ \Leftrightarrow \dot{\mathbf{q}} &= \mathbf{J}^\dagger \dot{\mathbf{x}} + \mathbf{P} \dot{\mathbf{q}}_{\text{any}}, \end{aligned} \quad (2.11)$$

where \mathbf{x} , again, denotes the end-effector velocities of concern, \mathbf{P} a projector onto the null space of \mathbf{J} and $\dot{\mathbf{q}}_{\text{any}}$ a vector of arbitrary joint velocities.

In order to solve eq. (2.11), an approach typically used in the literature is formulating the inverse kinematics problem as a constrained linear optimization problem, where the goal is to find the solutions $\dot{\mathbf{q}}$ that minimize a cost function g' defined as

$$g'(\dot{\mathbf{q}}) = \frac{1}{2} (\dot{\mathbf{q}} - \dot{\mathbf{q}}_{\text{any}})^T (\dot{\mathbf{q}} - \dot{\mathbf{q}}_{\text{any}}),$$

while satisfying the primary constraint (eq. (2.2)). This way, the norm of $(\dot{\mathbf{q}} - \dot{\mathbf{q}}_{\text{any}})$ is minimized in order to get solutions as close as possible to $\dot{\mathbf{q}}_{\text{any}}$, while $\dot{\mathbf{q}}_{\text{any}}$ can be specified so as to satisfy an additional constraint to the problem. The optimal solution then results in

$$\dot{\mathbf{q}} = \mathbf{J}^* \dot{\mathbf{x}} + (\mathbf{I} - \mathbf{J}^* \mathbf{J}) \dot{\mathbf{q}}_{\text{any}} \quad (2.12)$$

with the Moore-Penrose inverse $\mathbf{J}^* = \mathbf{J}^T (\mathbf{J} \mathbf{J}^T)^{-1}$. The first term $\mathbf{J}^* \dot{\mathbf{x}}$ of eq. (2.12) attempts to minimize the norm of joint velocities. The second term $(\mathbf{I} - \mathbf{J}^* \mathbf{J}) \dot{\mathbf{q}}_{\text{any}}$ is called homogeneous solution and endeavors to satisfy the additional constraint specified by $\dot{\mathbf{q}}_{\text{any}}$. In this case, the bracket term represents the projector matrix

$$\mathbf{P} = \mathbf{I} - \mathbf{J}^* \mathbf{J} \quad (2.13)$$

that maps $\dot{\mathbf{q}}_{\text{any}}$ in the null space of \mathbf{J} , allowing for internal joint motion at a fixed end-effector pose $\dot{\mathbf{x}} = \mathbf{0}$. This method was used in literature for task-oriented control at the inverse kinematics level in a sense of prioritized handling of subtasks [26, 29, 65, 80].

2.2 Dynamics of serial manipulators

The dynamics deals with the motion of bodies under the influence of forces. The dynamic model of a manipulator is the basis for the design of manipulator structures as well as for motion simulation and the design of control schemes. This allows for testing of control algorithms in a simulation environment without the need of using a physical manipulator.

The dynamic model is typically derived in the joint space and gives a description of the relationship between the joint actuator torques $\mathbf{\Gamma}$ and the motion of the structure in terms of the generalized coordinates $\mathbf{q} \in \mathbb{R}^n$ and their time derivatives $\dot{\mathbf{q}}$, $\ddot{\mathbf{q}}$. When neglecting joint friction torques for simplicity as well as forces and moments exerted by the end-effector on the environment, the general joint space dynamic model is represented by the following differential equation in minimal form:

$$\mathbf{A}(\mathbf{q})\ddot{\mathbf{q}} + \mathbf{b}(\mathbf{q}, \dot{\mathbf{q}}) - \mathbf{g}(\mathbf{q}) - \mathbf{Q}(\mathbf{q}, \dot{\mathbf{q}}) = \mathbf{\Gamma}. \quad (2.14)$$

In this notation, $\mathbf{A}(\mathbf{q}) \in \mathbb{R}^{n \times n}$ describes the symmetric, positive definite and in general configuration-dependent inertia matrix for an n -DOF manipulator. Vector $\mathbf{b}(\mathbf{q}, \dot{\mathbf{q}}) \in \mathbb{R}^n$ is the vector of Coriolis, gyroscopic and centrifugal forces, $\mathbf{g}(\mathbf{q}) \in \mathbb{R}^n$ contains the configuration-dependent joint forces by the presence of gravity, $\mathbf{Q}(\mathbf{q}, \dot{\mathbf{q}})$ is the vector of the projection of general external forces and $\mathbf{\Gamma} \in \mathbb{R}^n$ is the vector of generalized forces applied to the joints (termed joint torques), in this regard the vector of actuation torques [107].

The solution of the so-called equations of motion either gives a characterization of the acting forces and torques or a description of the motion in terms of time dependent position, velocity and acceleration coordinates of the system components. In order to solve the equations, depending on which values are known in advance, the branch is divided into inverse and direct dynamics.

2.2.1 Inverse dynamics

The inverse dynamics constitutes a method to reconstruct the joint torques $\mathbf{\Gamma}(t)$ depending on time t , that act on a manipulator and are responsible for its specific motion sequence for given $\ddot{\mathbf{q}}(t)$, $\dot{\mathbf{q}}(t)$ and $\mathbf{q}(t)$. Kinematic descriptions of the manipulator as well as inertia properties and possible external forces applied on the structure provide the basis for the calculation of those causal forces.

2.2.2 Direct dynamics

With respect to the joint torques $\mathbf{\Gamma}(t)$, the direct dynamics problem in joint space refers to the calculation of the resulting motion $\ddot{\mathbf{q}}(t)$, and thus $\dot{\mathbf{q}}(t)$, $\mathbf{q}(t)$, of the articulated mechanism for $t > t_0$, with t_0 referring to an initial time. In contrast to the inverse dynamics, the internal forces are known or established beforehand.

In detail, the joint accelerations can be computed through the dynamic model that allows for the description of the motion of the whole structure:

$$\ddot{\mathbf{q}} = \mathbf{A}^{-1}(\mathbf{q})[\mathbf{\Gamma} - \mathbf{b}(\mathbf{q}, \dot{\mathbf{q}}) + \mathbf{g}(\mathbf{q}) + \mathbf{Q}(\mathbf{q}, \dot{\mathbf{q}})], \quad (2.15)$$

once the state of the system in terms of the position $\mathbf{q}(t_i)$ and the velocity $\dot{\mathbf{q}}(t_i)$ at a specific time t_i is known. The position and velocity of the next time step $t_{i+1} = t_i + \Delta t$, with integration step Δt , then can be computed by a numerical integration method.

2.2.3 Relationship between joint torques and end-effector forces

On force level, the relationship between the joint torques and the generalized forces applied to the end-effector is given by the transpose of the manipulator Jacobian:

$$\mathbf{\Gamma} = \mathbf{J}^T(\mathbf{q})\mathbf{F}. \quad (2.16)$$

Here, \mathbf{F} denotes the vector of end-effector forces of the dimension r , $r \in \mathbb{N}$, of the operational space of interest. Analogous to the relationship between the joint and end-effector space at velocity level, the mapping between joint and end-effector space at force level can be illustrated as in fig. 2.4.

Similar to joint motion in the null space of the Jacobian that do not affect end-effector displacements, there exist end-effector forces which do not affect joint torques of a redundant manipulator in motion. These end-effector forces act within the null space $\mathcal{N}(\mathbf{J}^T)$ of the transpose of the Jacobian matrix and denote a subspace of \mathbb{R}^r . At a singular configuration, for example, the manipulator remains in its given posture no matter what end-effector force is acting. The range space $\mathcal{R}(\mathbf{J}^T)$ of the transposed Jacobian expresses the subspace of \mathbb{R}^n of those joint torques that are able to balance the applied end-effector forces [107].

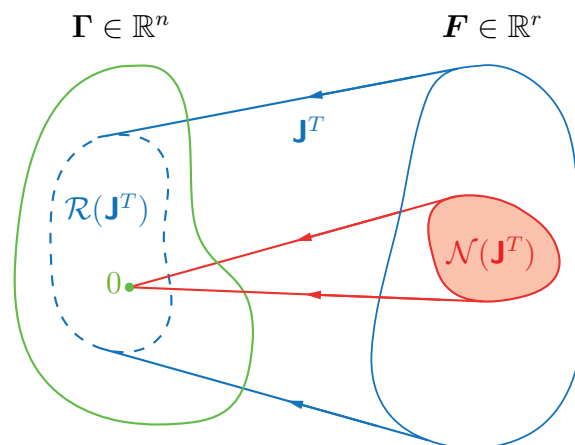


Figure 2.4: Mapping between end-effector and joint space at force level, inspired by [107].

3 Measurement and model

3.1 Sit-to-stand motion capture measurements

In order to generate reference data for the STS motion simulation, full body movement data of a healthy 31-year old female adult was recorded using a 3D motion tracking system from Vicon Motion Systems Ltd. This system includes seven cameras of type MX13 NIR for the motion capturing, two force platforms of type AMTI OR6-7-2000 for the recording of ground reactions and two high-speed cameras of type Basler A602FC to create video footage.

The process of recording movement is based on the principle that retroreflective markers, which are tracked by infrared cameras, reverberate the light back into the camera lenses in order to allow for the determination of two-dimensional marker positions w.r.t. each camera. Combining each camera data with calibration data, the equivalent digital motion of the body in three dimensions can be reconstructed.

In the experimental setup, motion capturing was enabled through 45 reflective markers that were placed on predefined body positions based on the Vicon Plug-in Gait model (see fig. 3.1).

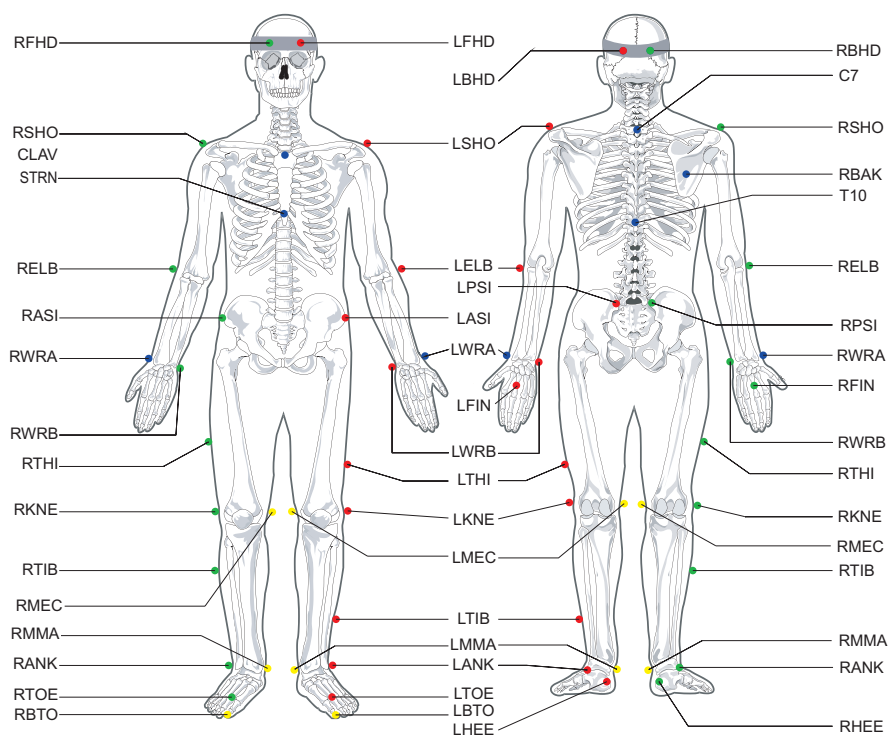


Figure 3.1: Marker designations and positions according to Plug-in Gait model [92].

The force platforms were positioned below the participants' feet and below the chair, respectively. A schematic of the experimental setup is shown in fig. 3.2.

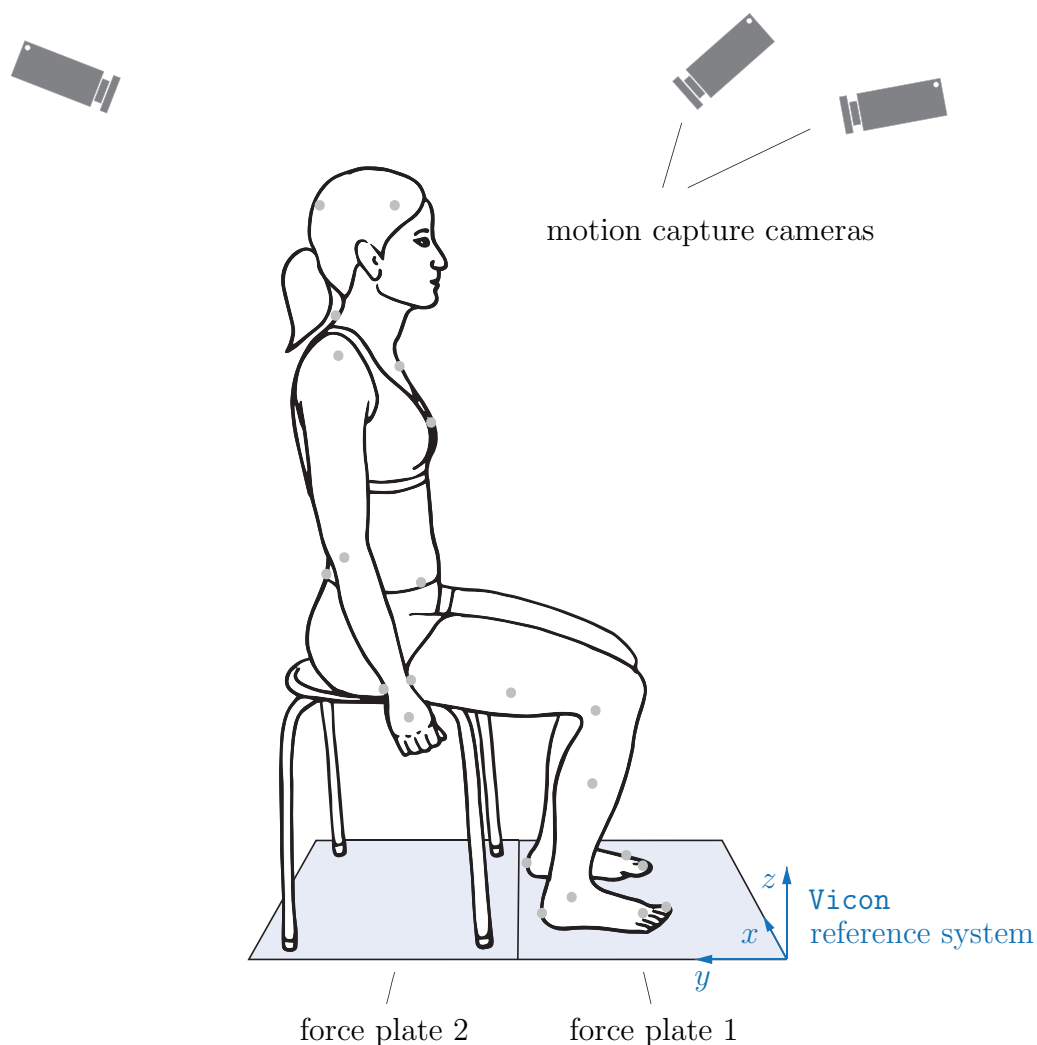


Figure 3.2: Schematic representation of the experimental setup for STS-measurements.

Every trial started with the participant sitting on a four legged hard-surface chair (height 0.45 m) without any arm or back support. After a “ready” signal, the participant counted to five, then stood up at a comfortable speed and counted to five again while standing until the trial was concluded. In order to be conform with the momentum transfer strategy mentioned in chapter 1, the test subject was instructed not to lift the feet from the ground and not to use the hands to push down on the chair or the thighs while performing the STS motion. In total, five valid measurements were recorded, from which three measurements were performed with arms hanging loosely next to the body and two with arms crossed in front of the chest. Those trials were

completed in one session with identical marker placement.

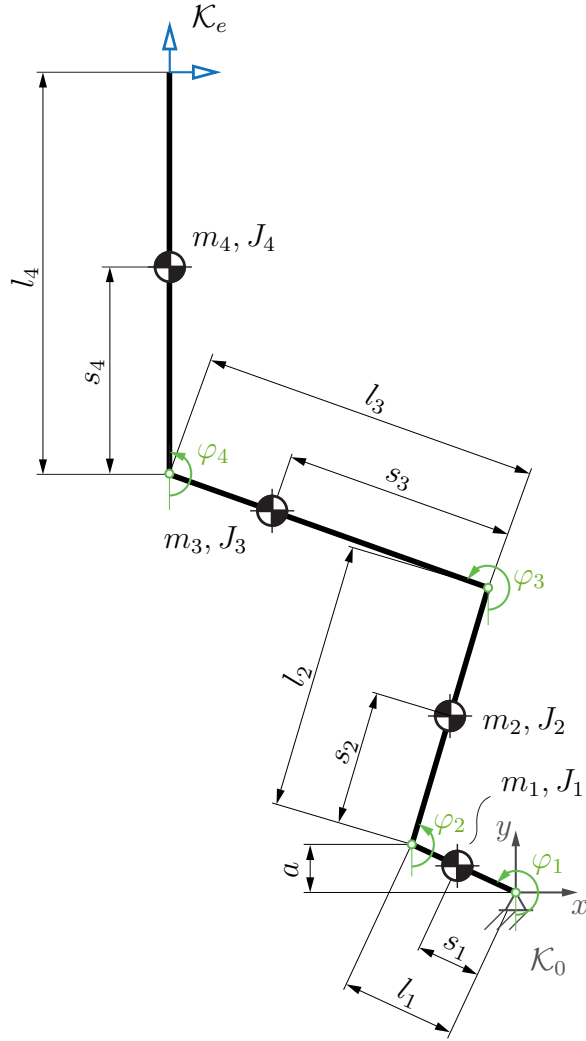
Measurement data were recorded with a sampling rate of 100 Hz in a synchronized manner by the use of the software *Vicon Nexus 2* and saved as a .c3d file. On the basis of marker position data for each frame, joint center positions are calculated through an algorithm of the Plug-in Gait model that provides 17 ideal joints and 17 segments (see fig. 3.1). The rigid body segments are connections between the joint centers. They originate in the pelvis joint, from which the lower body model is constructed. The upper body model is constructed in relation to the thorax. Segment positions and orientations are implicitly represented through segment coordinate systems and calculated based on the joint center positions to reconstruct 3D body motion.

The segment length, i.e. the distance between two relevant joint centers, is calculated frame by frame based on marker positions on the body. Continuous skin deformation and displacement relative to the underlying bone lead to relative marker movement. The soft tissue artifacts affect the rigid body kinematics in a sense that joint center and rotation axis estimations are not computed precisely and consistently and segment lengths of one trial differ over time. Possible error quantification and compensation depending on body segment and movement are described in the literature [7, 61, 66].

3.2 Biomechanical model

In this work, the complex human body is mechanically represented through a biomechanical model that consists of a planar 4R-mechanism (see fig. 3.3), in order to take the rocking of the feet into account that could be observed in the experiments.

The skeletal model is composed of four rigid bodies that are connected through four revolute joints: link one (l_1) is connected to the ground in the origin of the toe joint, illustrated through the base frame \mathcal{K}_0 , and represents both feet, link two (l_2) is connected to link one through the ankle joint and depicts both shanks that are, in turn, coupled at the knee joint with link three (l_3), representing both thighs. Head, arms and trunk are composed of a composite object in link four (l_4), which is connected with link three at the hip joint. The upper body constitutes the end-effector whose pose is represented through coordinate frame \mathcal{K}_e .

**Notation:**

\mathcal{K}_0	base frame
\mathcal{K}_e	end-effector frame
φ_i	joint angle, with $i = 1, \dots, 4$
m_i	segment mass
J_i	moment of inertia w.r.t. segment center of mass
l_i	segment length
s_i	distal offset of segment center of mass
a	ankle height

Figure 3.3: Quadruple pendulum model.

It is assumed that both feet are in continuous contact with the ground and that joint friction can be neglected. Furthermore, only movement in the sagittal plane is considered. Due to the planar restriction, each joint has one DOF, thus the model itself has four DOFs. Joint angles φ_i , with $i = 1, \dots, 4$, are measured w.r.t. the vertical y .

3.2.1 Anthropometric model data

As described in section 3.1, measurements of segment lengths vary over time due to skin artifacts. In order to utilize constant segment lengths for the quadruple pendulum model, link lengths l_i are in general computed as the mean value of the aforementioned five valid measurements:

First, shank length l_2 and thigh length l_3 were calculated as the mean value of right

and left side of the lengths computed by the Plug-In Gait model for each measurement, in order to allow for a transmission to the sagittal plane. These variable mean values are illustrated in fig. 3.4 (named measurement 1 to 5).

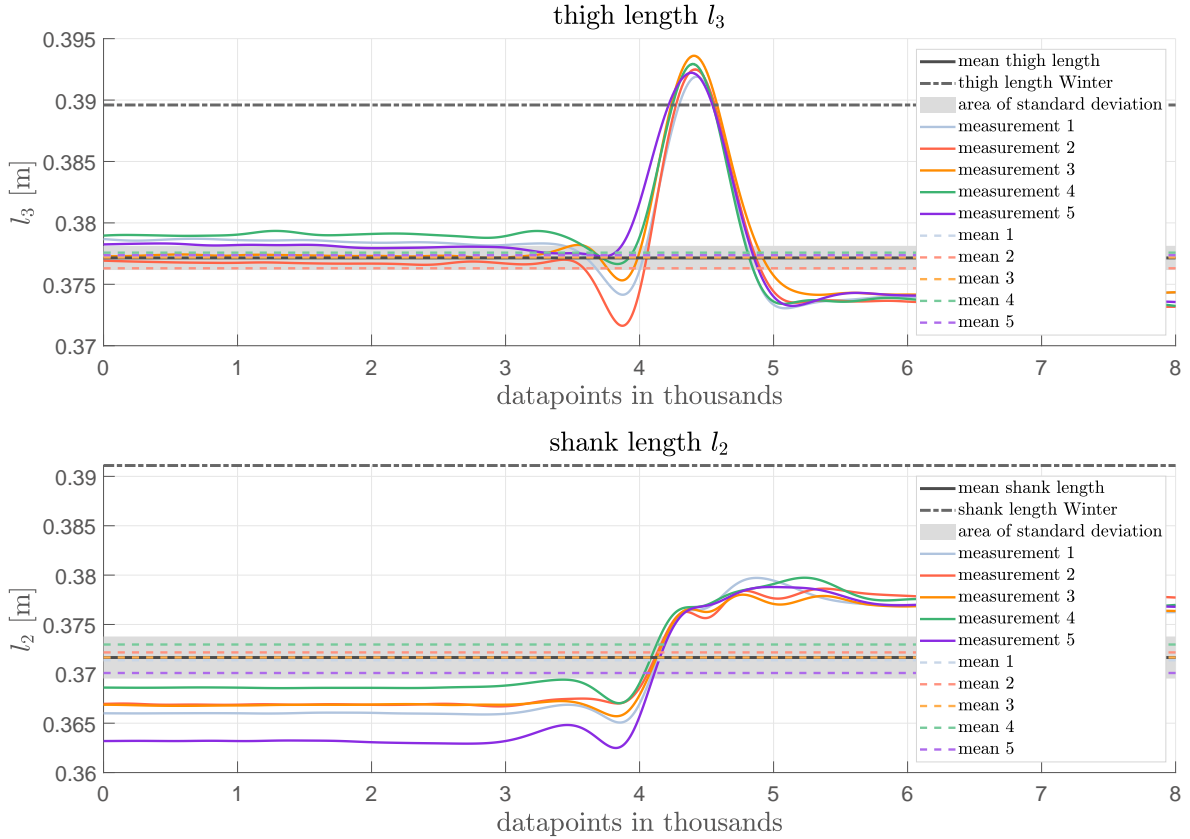


Figure 3.4: Mean thigh and shank segment lengths (l_3 and l_2) of five valid STS-measurements over time: mean thigh and shank lengths over measurements (black lines); dimensions according to literature (black dashed/dotted lines) [114, 17].

Since every measurement differs in its time duration, the curves have been aligned in time in order to synchronize the moment of seat-off, i.e. the time where the buttocks just loses contact to the seat. Over the different lengths for various STS-measurements, the mean value over time was then computed with respect to each measurement (dashed lines, named mean 1 to 5). On the basis of those five means, again, the total mean value was calculated (black line) and employed in the model.

As a comparison, segment lengths according to Drillis and Contini [17] mentioned in Winter [114] are illustrated in dashed/dotted black lines (fig. 3.4). In their work, dimensions are expressed as a percentage of body height in order to serve as an approximation in the absence of individual measured data. Hence, it is not surprising

that these segment lengths do not lie within the standard deviation interval (area highlighted in gray) with regard to the particular test subject, as these values cover a grouping of varying individuals of different gender, origin and age. Such a general description of body dimensions is not useful for this thesis, since measurement data exist for realistically representing the test subjects dimensions.

The upper body length l_4 was approximated based on the total body height h , the segment lengths of shank l_2 and thigh l_3 and the ankle joint height a , because no measurement data was available regarding the end point of the head:

$$l_4 = h - a - l_2 - l_3 .$$

For the calculation of the constant upper body length l_4 , the ankle joint height a , again, was computed as the average of right and left side over five measurements and over time.

Segment length l_1 regarding the feet was measured on the test subject itself, since *Vicon* does not calculate any toe joint center and Winter [114] does not provide any general formula concerning the distance between ankle joint and toe joint, either.

Based on the segment lengths, the anthropometric data for the biomechanical model were computed according to Winter [114], as in *Vicon's* Plug-in Gait model. The anatomical parameters include each segment mass m_i , radius of gyration ρ_i w.r.t. the segment center of mass, moment of inertia $J_i = m_i \rho_i^2$ w.r.t. the segment center of mass as well as distal distance s_i of the segment center of mass (see fig. 3.3). Segment masses m_1 to m_3 were doubled, since left and right side of legs and feet were modeled as a single entity implying perfect symmetry.

The anatomical parameters of the test subject with a body height of 1.59 m and a body mass of 48 kg are shown in tab. 3.1.

Anthropometric data	foot ($i = 1$)	shank ($i = 2$)	thigh ($i = 3$)	HAT ($i = 4$)
m_i [kg]	1.3920	4.4640	9.6000	32.5440
l_i [m]	0.1700	0.3717	0.3771	0.7742
ρ_i [m]	0.0808	0.1123	0.1218	0.6991
J_i [kg m ²]	0.0091	0.0563	0.1424	15.9057
s_i [m]	0.0850	0.2108	0.2138	0.2896

Table 3.1: Anthropometric data of the biomechanical model for the considered test subject, where HAT is the entity consisting of head, arms and trunk.

3.2.2 Orientation data transmission to the model

For the quadruple pendulum model, measurement data of segment orientations and corresponding angular velocities as well as accelerations provide the basis for

- (i) the initial model pose in the form of an initial condition for the forward STS-simulation (explained in chapter 4.5), and
- (ii) calculating the head trajectory, which, in turn, serves as input datum for the employed operational space control method (described in chapter 4).

The orientation data are gathered from the .c3d file of the corresponding **Vicon** measurement mentioned in chapter 3.1, which, among others, contains marker trajectories, ground reaction forces and angle trajectories of the body segments. These angles, delivered frame by frame, were projected onto the sagittal plane and interpolated using splines of order five without any smoothing factor. In this way, angles between body segments and their corresponding time derivatives were described as functions dependent on time. In the following, the transmission of the measured segment orientations onto the biomechanical model is briefly presented.

For the ankle and knee joint angles φ_2 and φ_3 , respectively, the mean of right and left side was calculated and its description transformed w.r.t. the vertical, i.e. the y -axis of the base frame \mathcal{K}_0 .

The upper body orientation φ_4 was computed based on the angle of link l_4 w.r.t. the vertical. Link l_4 arises from the connection of the pelvis joint center and the position of the last cervical vertebra at the middle of the head. Since **Vicon**'s head joint center

lies outside the head – contrary to its documentation [92, 112] for unknown reasons and currently still under investigation – a constant shift of 0.1536 m into the approximate middle of the head was manually performed.

As **Vicon** does not generate a toe joint center and the distance l_1 was measured on the test subject itself (see chapter 3.2.1), foot angle φ_1 was calculated based on the variable ankle height a taken from the measurement data:

$$\varphi_1 = \frac{3}{2}\pi - \arcsin\left(\frac{a}{l_1}\right). \quad (3.1)$$

3.2.3 Dynamic model description

The dynamics of the four-link rigid-body model depicted in fig. 3.3 are described by a set of nonlinear differential equations, compactly written in matrix form (cf. eq. (2.14)):

$$\mathbf{A}(\mathbf{q})\ddot{\mathbf{q}} + \mathbf{b}(\mathbf{q}, \dot{\mathbf{q}}) - \mathbf{g}(\mathbf{q}) - \mathbf{Q}(\mathbf{q}, \dot{\mathbf{q}}) = \mathbf{\Gamma}.$$

The equations in joint space were derived through **LAGRANGE**'s equation of the second kind and are shown in appendix C. The composition of the vector of general external forces $\mathbf{Q}(\mathbf{q}, \dot{\mathbf{q}})$ is based on modeled horizontal and vertical contact forces F_{b_x} and F_{b_y} between chair and buttocks, as explained subsequently.

For this purpose, measured horizontal and vertical ground reaction forces F_{measured_x} and F_{measured_y} were transmitted to the center of pressure (COP) on the chair surface at height s , as illustrated in fig. 3.5. Arising moments are canceled out by the corresponding shift $\Delta r_x = s \cdot \frac{F_{b_x}}{F_{b_y}}$ of the chair's COP w.r.t. the COP on the ground. Note, that the force plate was initialized with the rigid chair on top. That is why the weight of the chair is not taken into account and the ground reaction forces, that are illustrated in fig. 3.5, are meant to act on the body.

However, the horizontal shift Δr_x is widely overstated in the illustration. While sitting motionless, the COP on the chair surface is only shifted by $\Delta r_x = 0.007\text{ m}$. The shift reaches a maximum of $\Delta r_x = 0.08\text{ m}$ shortly before seat-off. This is shown in fig. 3.6, where measured ground reaction forces, corresponding x -positions of the COPs regarding the ground and the chair as well as the difference Δr_x between those COPs are plotted for an exemplary measurement.

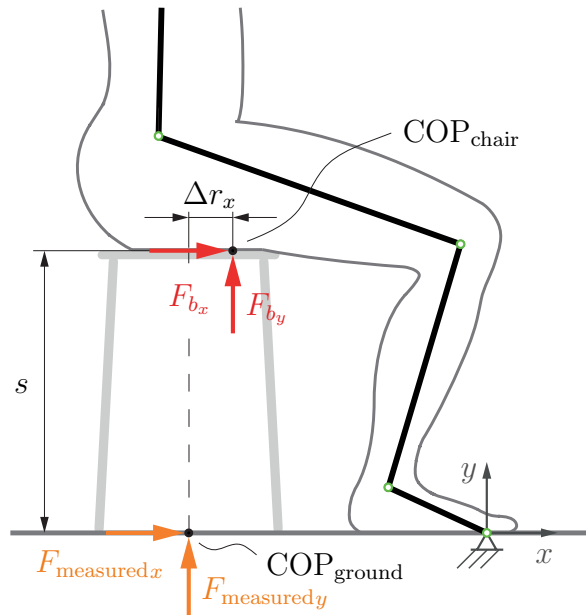


Figure 3.5: Transmission of measured ground reaction forces onto the chair surface.

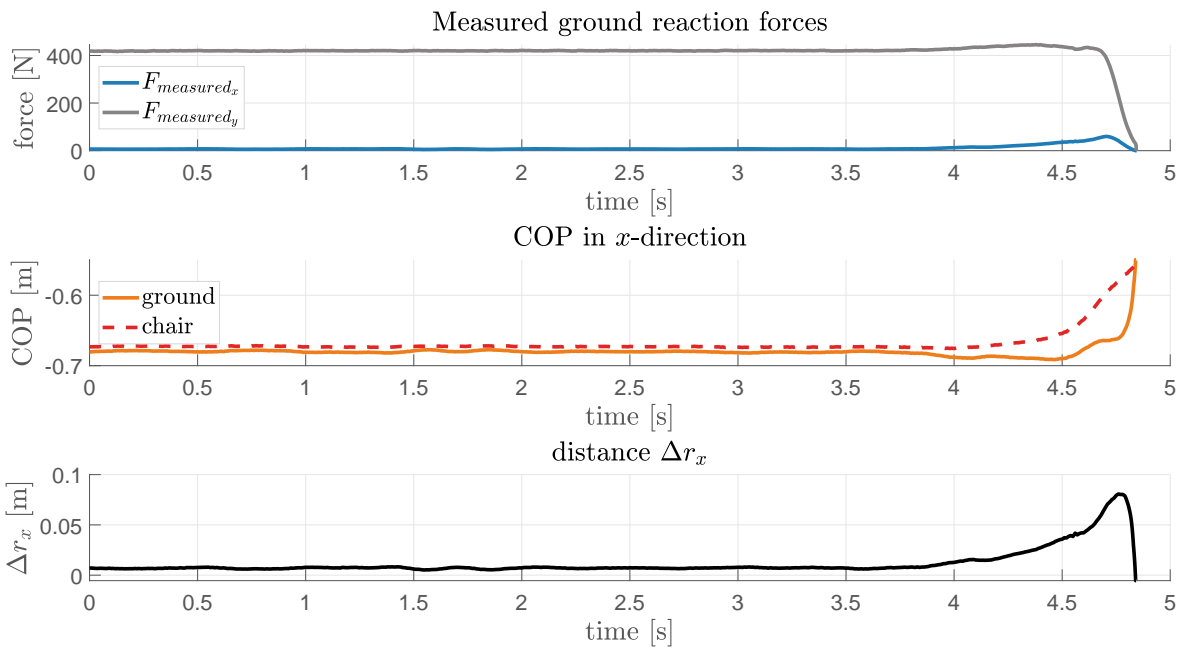


Figure 3.6: Measured ground reaction forces under the chair (upper plot) including COP-positions of measured forces as well as of transmitted forces on the chair surface (middle plot) and corresponding distance Δr_x between both COPs (lower plot).

As the difference Δr_x between the chair's COP and the COP on the ground is relatively small, it was omitted for the transmission onto the model itself. Moreover, due to the lack of a concrete model regarding the rolling of the chair's COP, the resulting points

of force application were assumed to be located on the bone structure on link l_3 in constant distances b_x and b_y w.r.t. the hip joint, as illustrated in fig. 3.7.

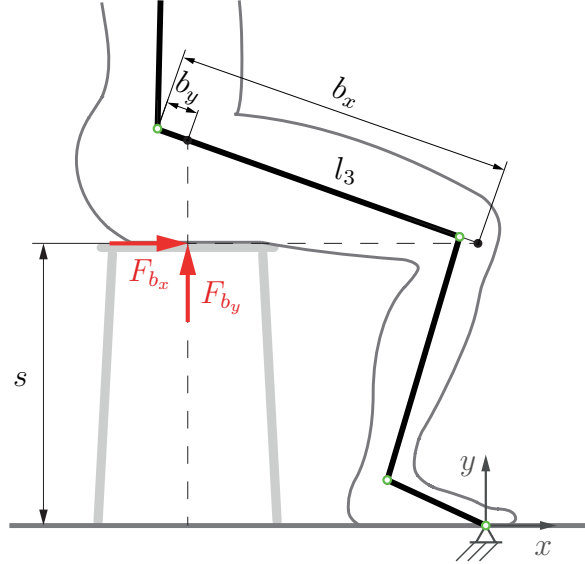


Figure 3.7: Transmission of forces onto the model.

The distance $b_x = 0.3156 \text{ m}$ of the point of action of F_{b_x} and the offset $b_y = 0.0403 \text{ m}$ regarding the point of force application of F_{b_y} w.r.t. the hip joint were calculated as the mean values of the initial points of load application based on the valid STS-measurements with an experimental setup as described in chapter 3.1.

The result for the projected buttocks force then is:

$$\begin{aligned} \mathbf{Q} &= \mathbf{J}_b^T \cdot \begin{bmatrix} F_{b_x} \\ F_{b_y} \end{bmatrix} \\ &= \begin{bmatrix} l_1 \cos \varphi_1 & l_2 \cos \varphi_2 & (l_3 - b_x) \cos \varphi_3 & 0 \\ l_1 \sin \varphi_1 & l_2 \sin \varphi_2 & (l_3 - b_y) \sin \varphi_3 & 0 \end{bmatrix}^T \cdot \begin{bmatrix} F_{b_x} \\ F_{b_y} \end{bmatrix}, \end{aligned} \quad (3.2)$$

where \mathbf{J}_b is the Jacobian matrix comprising the partial derivatives of the corresponding position vectors of the buttocks forces w.r.t. the joint angles.

3.2.4 Buttocks contact force model

During the initial state of STS motion the buttocks are transmitting a great amount of body weight while sitting, according to the literature up to 79 percent depending on the seating condition [83, 81], according to our measurements even around 89 percent due to a straight sitting position without any support. The large contact force between chair and buttocks that is acting while sitting and vanishing in the moment of seat-off – schematically illustrated in fig. 3.8 – has a huge impact on the overall joint torques and, therefore, is important to be modeled as precise as possible for realistic STS-prediction.

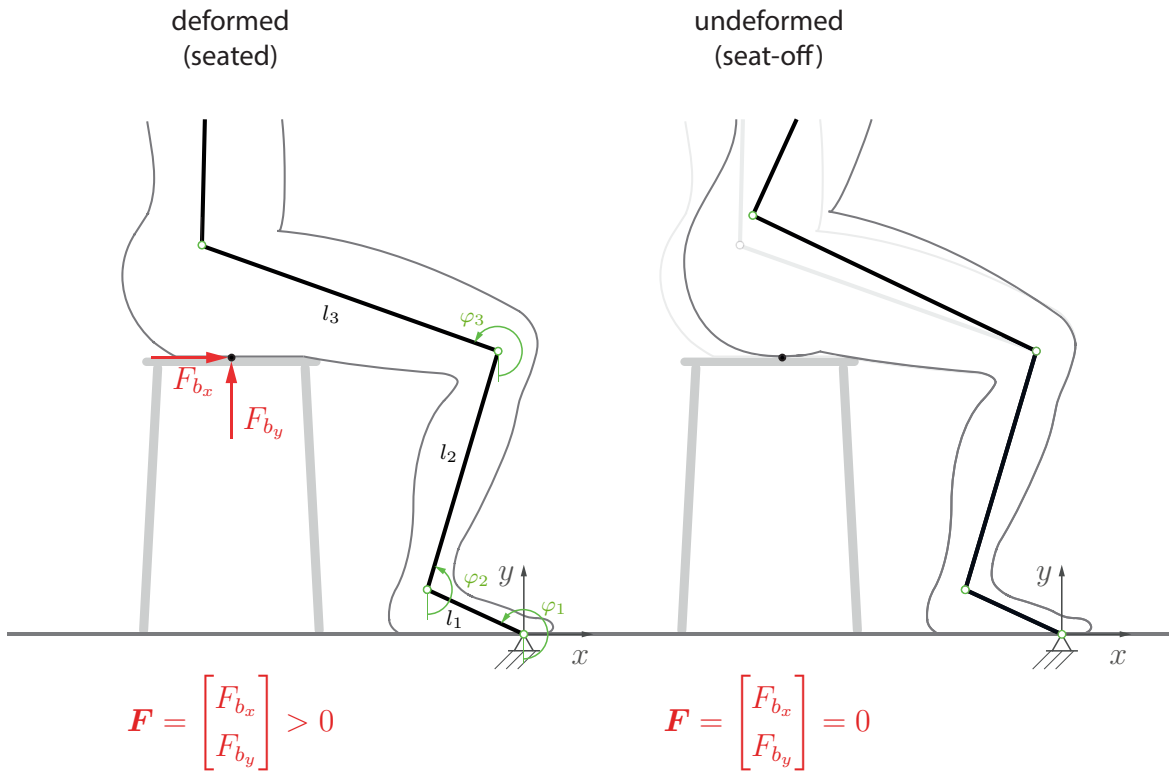


Figure 3.8: Contact forces between chair and buttocks in the deformed and undeformed state.

In the literature, some models for the subcutaneous adipose tissue, a connective tissue between the dermis and the aponeurosis and fasciae of the muscles for small or large ranges of deformation, exist. One was introduced by Geerligs et al. [21] in order to describe the linear visco-elastic behavior of this layer of tissue. This model, however, is limited to small strain behavior and provides limited descriptions of the overall mechanical behavior. In Sommer et al. [109], the quasi-static multiaxial mechanical response of human adipose tissue was determined and mathematically represented in

terms of parameters of a hyper-elastic strain-energy function. Parameters were identified based on experiments on the abdominal fat tissue to serve as a basis for soft tissue simulations using the finite element method. In Palevski et al. [87], measured data was fitted to a biexponential equation based on tests regarding the compression of porcine gluteus muscles perpendicular to the direction of muscle fibers, which provided the characterization of shear moduli and the time course of viscoelastic stress relaxation of in vitro tissue. However, the literature lacks a validated model of buttocks tissues in particular as well as information required for mathematical modeling.

For the sitting posture, an experimental model for the estimation of the shear force acting on the skin surface of the buttocks for comfortable sitting while leaning against a backrest was given by Kobara et al. [57] without considering the legs. In order to study the dynamic responses to vertical vibration excitation, a spring-damper-component was used in several biodynamic models of seated human subjects to connect the chair and the human model, which can be found amongst others in a study of Liang and Chiang [62].

Within the STS forward simulation, aforementioned buttocks force considerations are rare and do mostly not contain an explicit model of the contact forces. Ozsoy and Yang [84] for example do not model the vertical buttocks force per se, but consider it in an objective function as the minimization of the difference in the vertical support reaction forces between the right and left side of the body. In Prinz et al. [91], the effects of a chair on a seated individual were simulated by considering the sufficiency of joint torques to lift the biomechanical model from the chair's surface without the use of an explicit chair or buttocks model. Sadeghi et al. [98] used a soft point contact model in horizontal and vertical direction on the hip by two couples of non-linear spring-damper elements with manually adjusted parameters. A parallel connection of a spring and damper element, i.e. the Kelvin-Voigt model, is also used by Norman-Gerum [81] who claims to have firstly introduced a physically meaningful force-deformation description of the buttocks.

In this thesis, two models for the vertical as well as the horizontal buttocks force component (F_{b_y} and F_{b_x} , respectively) are presented: (a) A Kelvin-Voigt model, inspired by Norman-Gerum [81], and (b) a Gaussian function model. Both are based on the assumptions presented in section 3.2.3 and mean values over five STS-measurements (see chapter 3.1) form the basis for the construction of the models presented hereafter.

3.2.4.1 Kelvin-Voigt model

At first, a mechanical buttocks model inspired by Norman-Gerum [81] was examined. Therein the biological tissue is represented by a visco-hyperelastic material, which is modeled through the Kelvin-Voigt model as can be seen in fig. 3.9. The idea is to limit the extent of the deformation of the tissue at the buttocks with the help of the spring and to slow down the speed of deformation with the help of the damper. Since the deformation only prevails while sitting, the contact force between chair and buttocks is modeled until the moment of seat-off, where the buttocks is no longer in contact with the seat and the spring is not deformed any more. After seat-off, the contact force is set to be zero due to the undeformed state of the tissue.

Vertical buttocks force model

The vertical buttocks force F_{b_y} is represented through a vertical spring-damper-element between chair and point of force application (see fig. 3.9) and is therefore generated as the sum of the spring and damper force until the moment of seat-off.

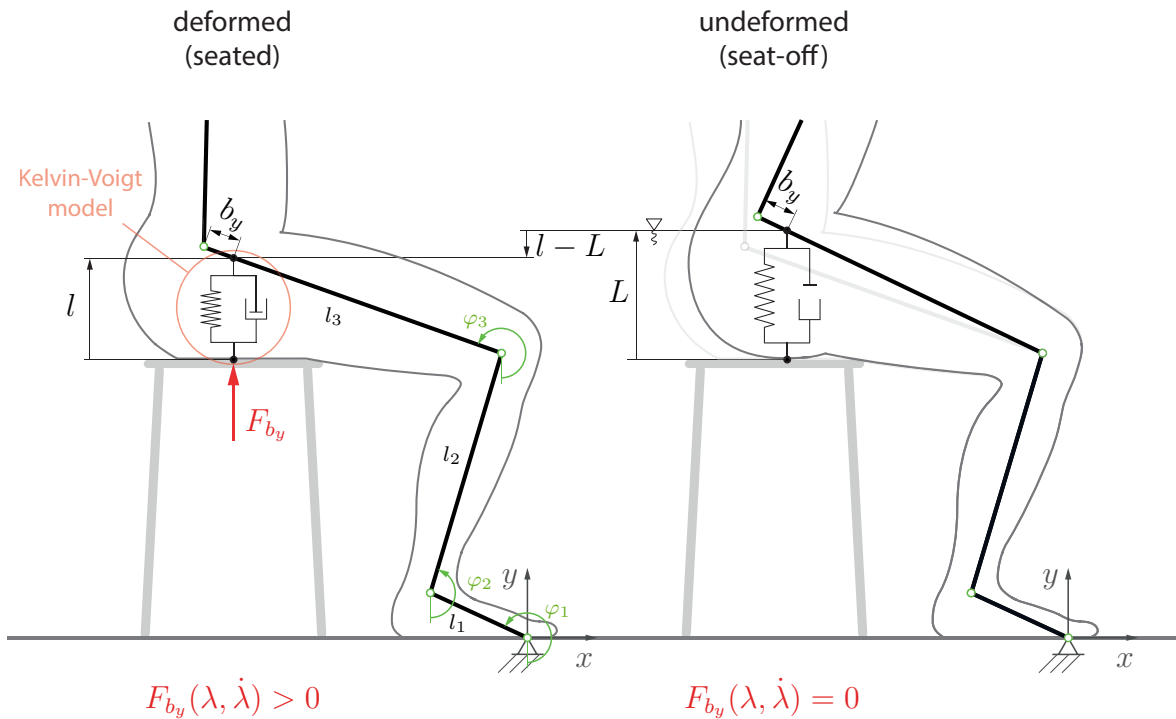


Figure 3.9: Mechanical model of vertical buttocks contact force.

The spring force is computed by a non-linear spring element characterized through a

Mooney-Rivlin function

$$F_{\text{spring}} = \mu_1(\lambda - \lambda^{-2}) + \mu_2(\lambda^{-3} - 1),$$

where the stretch ratio λ

$$\lambda = \frac{l}{L} \quad (3.3)$$

describes the relation of the distance $l = l(\varphi_1, \varphi_2, \varphi_3)$ between seat and point of force application in the deformed state and $L = l_{\text{seat-off}}$, which is distance l during the undeformed buttocks state at seat-off. μ_1 and μ_2 are material constants that need to be identified.

The damping force is in general proportional to the speed of deformation

$$\begin{aligned} F_d &= c \cdot \frac{d}{dt} (l - L) \\ &= c L \dot{\lambda} \end{aligned}$$

with damping constant c and $\dot{\lambda} = \frac{d}{dt} \left(\frac{l}{L} \right)$. This force is activated and deactivated depending on the spring force:

$$F_{\text{damper}} = \begin{cases} F_{\text{spring}} & , F_d < F_{\text{spring}} \\ -F_{\text{spring}} & , F_d > -F_{\text{spring}} \\ F_d & , \text{else.} \end{cases}$$

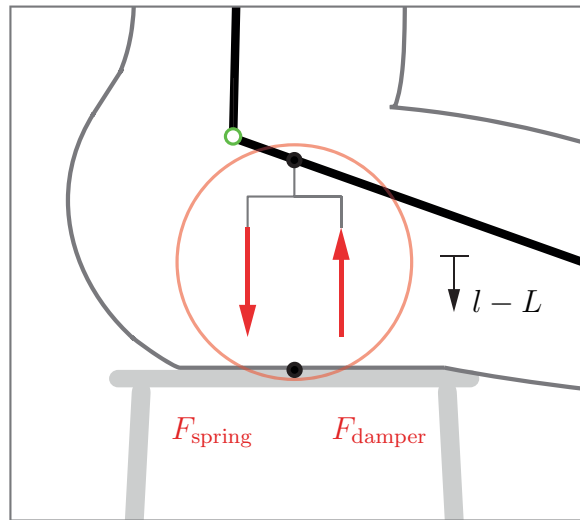


Figure 3.10: Mechanical model of vertical buttocks contact force.

As the spring force is a negative compressive force due to $\lambda < 1$ until seat-off (see fig.

3.11, middle plot), the total vertical buttocks contact force is computed by

$$F_{b_y} = -F_{\text{spring}} + F_{\text{damper}} \quad (3.4)$$

according to the definition of positive spring and damper forces in fig. 3.10. With a computed mean distance $L = 0.1388 \text{ m}$ at seat-off, the parameters μ_1 , μ_2 and c in tab. 3.2 were found through constrained optimization. The optimization was performed using the MATLAB routine `fmincon`, which finds the minimum of a constrained nonlinear multivariable function. The cost function is specified by the squared difference between the modeled and measured vertical contact force $F_{\text{diff}}(\mathbf{z}) = (F_{b_y}(\mathbf{z}) - F_{\text{measured}_y})$, where F_{b_y} represents the model in eq. (3.4) that is dependent on the material constants μ_1 , μ_2 and the damping constant c collected in a vector $\mathbf{z} = [\mu_1 \ \mu_2 \ c]^T$. The routine computes the positive parameters in \mathbf{z} by solving the optimization problem

$$\begin{aligned} &\text{minimize} \quad F_{\text{diff}}^2(\mathbf{z}) \\ &\text{subject to} \quad \mathbf{z} \geq \mathbf{0}. \end{aligned}$$

The options were set to be `StepTolerance = 1.0e - 5`, `OptimalityTolerance = 1.0e - 3` and `MaxIterations = 500`, while all other options were left to their default settings. After several runs with various initial values within a reasonable range for the model, the program always found the same two distinct solutions. Using those solutions as initial values did not improve the result. Only one of the two yielded cost optimal parameters that are shown in tab. 3.2. Here for example, the initial values $\mathbf{z}_0 = [1.0 \ 20.0 \ 500.0]^T$ were set.

Parameter	Value
μ_1 [kg m/s ²]	332.6555
μ_2 [kg m/s ²]	104.7953
c [kg/s]	1315.7

Table 3.2: Kelvin-Voigt parameter settings for vertical contact force.

The modeled vertical contact force under the specified parameter values of tab. 3.2 are illustrated in red dashed lines below. Fig. 3.11 shows the mean value of the five measured vertical contact forces F_{b_y} as well as the modeled force and corresponding force components over time until seat-off. At this point, which is marked through a vertical dashed line, the contact force is zero and the stretch ratio becomes one, which is shown in the middle plot. The plot at the bottom shows the velocity of the stretch ratio, which is relevant for the actual damping force F_d .

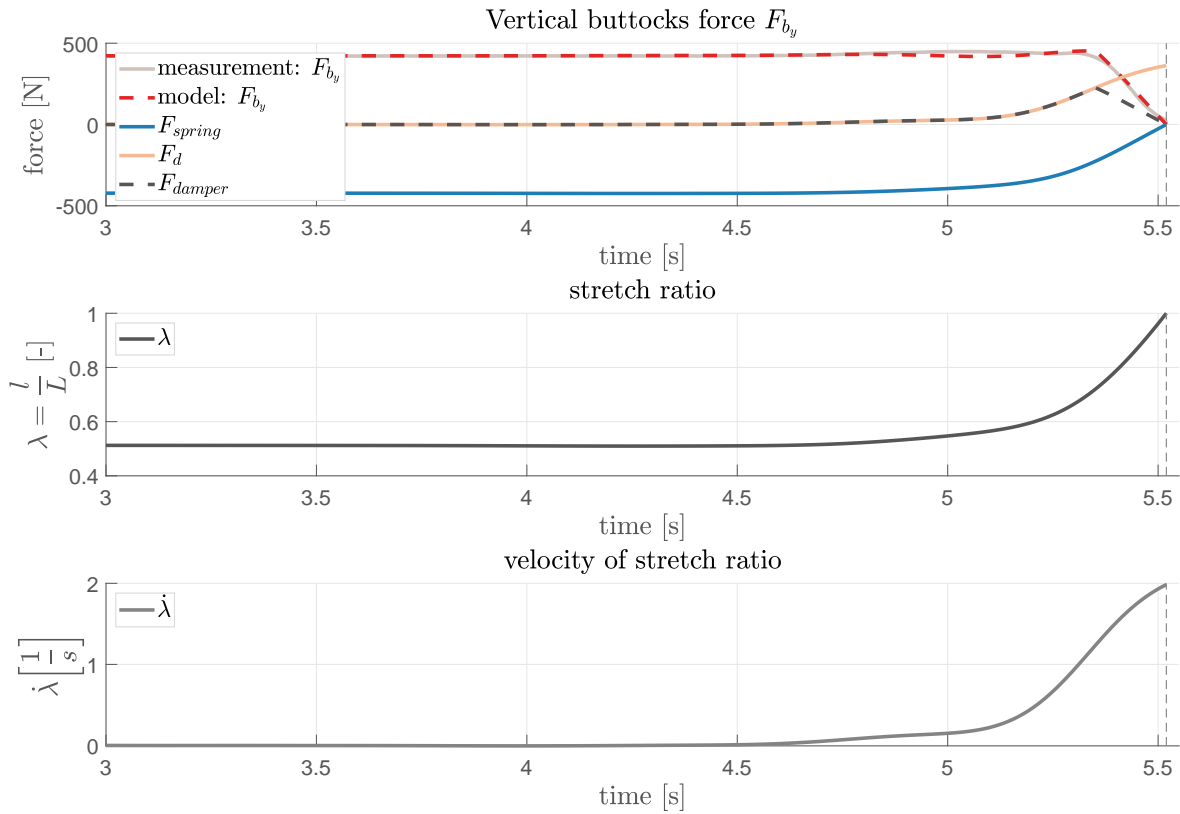


Figure 3.11: Approximated vertical contact force F_{b_y} using Kelvin-Voigt model (upper plot, red dashed line) and corresponding vertical stretch ratio (middle plot) and its velocity w.r.t. time (lower plot).

Since the model is dependent on the stretch ratio, the vertical buttocks force F_{b_y} is plotted as a percentage of body weight and a function of λ in its measured and modeled state in fig. 3.12. It becomes clear, that the Kelvin-Voigt model provides only a vague approximation to the problem.

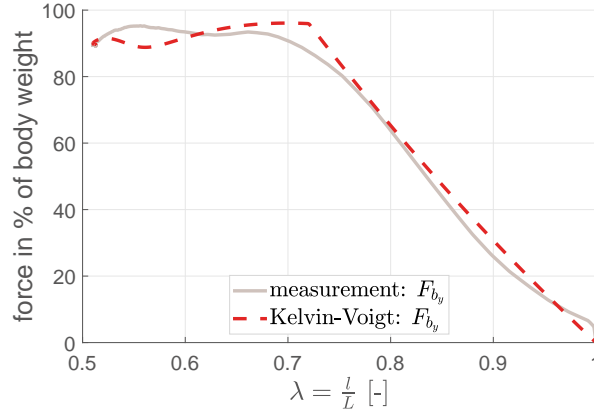


Figure 3.12: Measured and modeled vertical contact force F_{by} as a percentage of body weight w.r.t. λ .

Horizontal buttocks force model

Using the Kelvin-Voigt model, the horizontal buttocks force is computed in a similar way compared to the above presented approach. As shown in fig. 3.13, the spring-damper-element is placed horizontally between the hip joint and the point of force application on the height of the chair in order to model the horizontal contact force F_{bx} between chair and buttocks. As in the Kelvin-Voigt model for the vertical force, the horizontal contact force is generated as the sum of the spring and damper force until the moment of seat-off. The spring force, again, is computed via a non-linear spring element given by a Mooney-Rivlin function

$$F_{\text{spring}} = \mu_1(\eta - \eta^{-2}) + \mu_2(\eta^{-3} - 1),$$

where the horizontal displacement ratio η

$$\eta = \frac{r}{R} \quad (3.5)$$

describes the relation of the distance $r = r(\varphi_1, \varphi_2, \varphi_3)$ between hip joint and point of force application in the deformed state and $R = r_{\text{seat-off}}$, which is distance r during the undeformed buttocks state at seat-off. μ_1 and μ_2 , again, are material constants that need to be identified.

The damping force is also proportional to the speed of deformation

$$\begin{aligned} F_d &= c \cdot \frac{d}{dt} (r - R) \\ &= c R \dot{\eta} \end{aligned}$$

with damping constant c and $\dot{\eta} = \frac{d}{dt} \left(\frac{r}{R} \right)$. This force is activated and deactivated

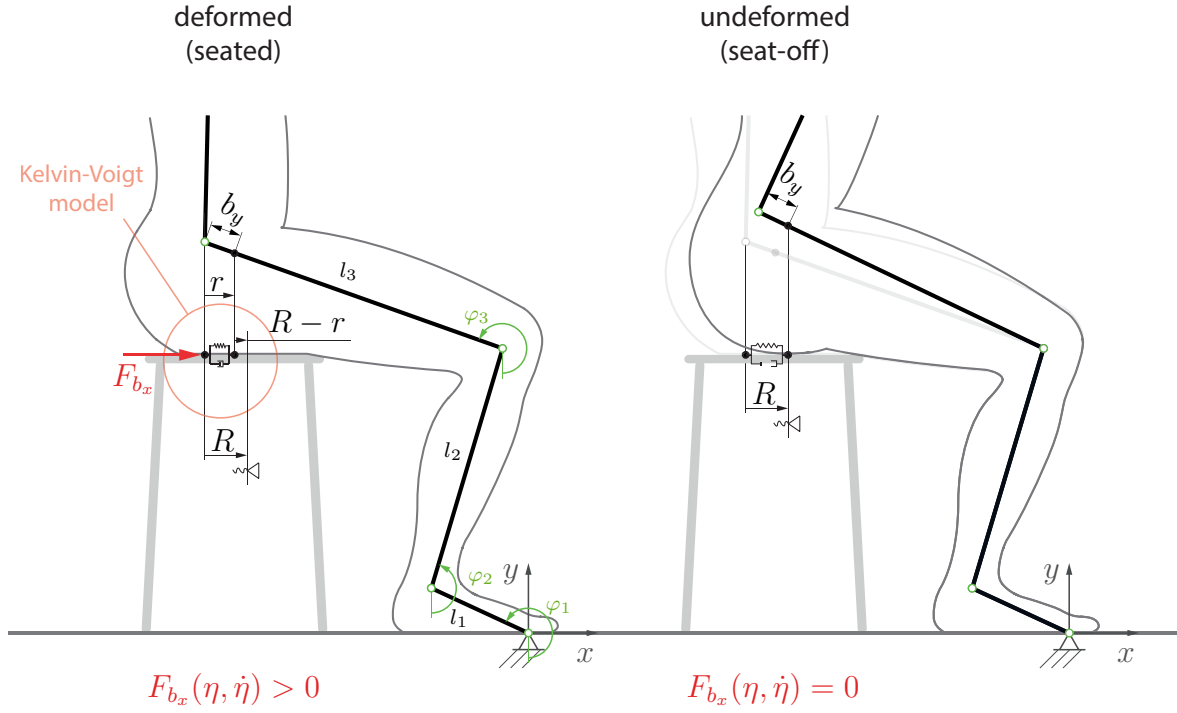


Figure 3.13: Mechanical model of horizontal buttocks contact force.

depending on the spring force:

$$F_{\text{damper}} = \begin{cases} F_{\text{spring}} & , F_d < F_{\text{spring}} \\ -F_{\text{spring}} & , F_d > -F_{\text{spring}} \\ F_d & , \text{else.} \end{cases}$$

Equally to the vertical force model, the total horizontal buttocks contact force is computed by

$$F_{b_x} = -F_{\text{spring}} + F_{\text{damper}} . \quad (3.6)$$

With a computed mean distance $R = 0.1148 \text{ m}$ at seat-off, the parameters μ_1 , μ_2 and c in tab. 3.2 were found through constrained optimization. As with the vertical Kelvin-Voigt model, the optimization was performed using the MATLAB routine `fmincon`. The cost function is analogously specified by the squared difference between the modeled and measured horizontal contact force $F_{\text{diff}}(\mathbf{z}) = (F_{b_x}(\mathbf{z}) - F_{\text{measured}_x})^2$, where F_{b_x} represents the model in eq. (3.6) that is dependent on the material constants μ_1 , μ_2 and the damping constant c collected in a vector $\mathbf{z} = [\mu_1 \ \mu_2 \ c]^T$. Again, the routine computes the positive parameters in \mathbf{z} by solving the optimization problem

$$\begin{aligned} & \text{minimize } F_{\text{diff}}^2(\mathbf{z}) \\ & \text{subject to } \mathbf{z} \geq \mathbf{0} . \end{aligned}$$

Same as before, the options were set to be `StepTolerance = 1.0e - 5`, `OptimalityTolerance = 1.0e - 3` and `MaxIterations = 500`, while all other options were left to default. The optimal solution is shown in tab. 3.3 using the initial values $\mathbf{z}_0 = [60.0 \ 50.0 \ 30.0]^T$.

Parameter	Value
μ_1 [kg m/s ²]	23.6660
μ_2 [kg m/s ²]	7.6945
c [kg/s]	88.9032

Table 3.3: Kelvin-Voigt parameter settings for horizontal contact force.

The modeled horizontal contact force under the specified parameter values of tab. 3.3 are illustrated in red dashed lines below. Fig. 3.14 shows the mean value of the measured horizontal contact forces F_{b_x} as well as the modeled force and corresponding force components over time until seat-off. At this point, which is marked through a vertical dashed line, the contact force is zero and the horizontal displacement ratio becomes one, which is shown in the middle plot. The plot at the bottom shows the velocity of the displacement ratio, which is relevant for the actual damping force F_d .

Since the model is dependent on the horizontal displacement ratio, the horizontal buttocks force F_{b_x} is plotted as a function of η in its measured and modeled state in fig. 3.15, again as a percentage of body weight. The Kelvin-Voigt model for the horizontal buttocks force with the parameter setting from tab. 3.3 provides only a rough approximation to the problem.

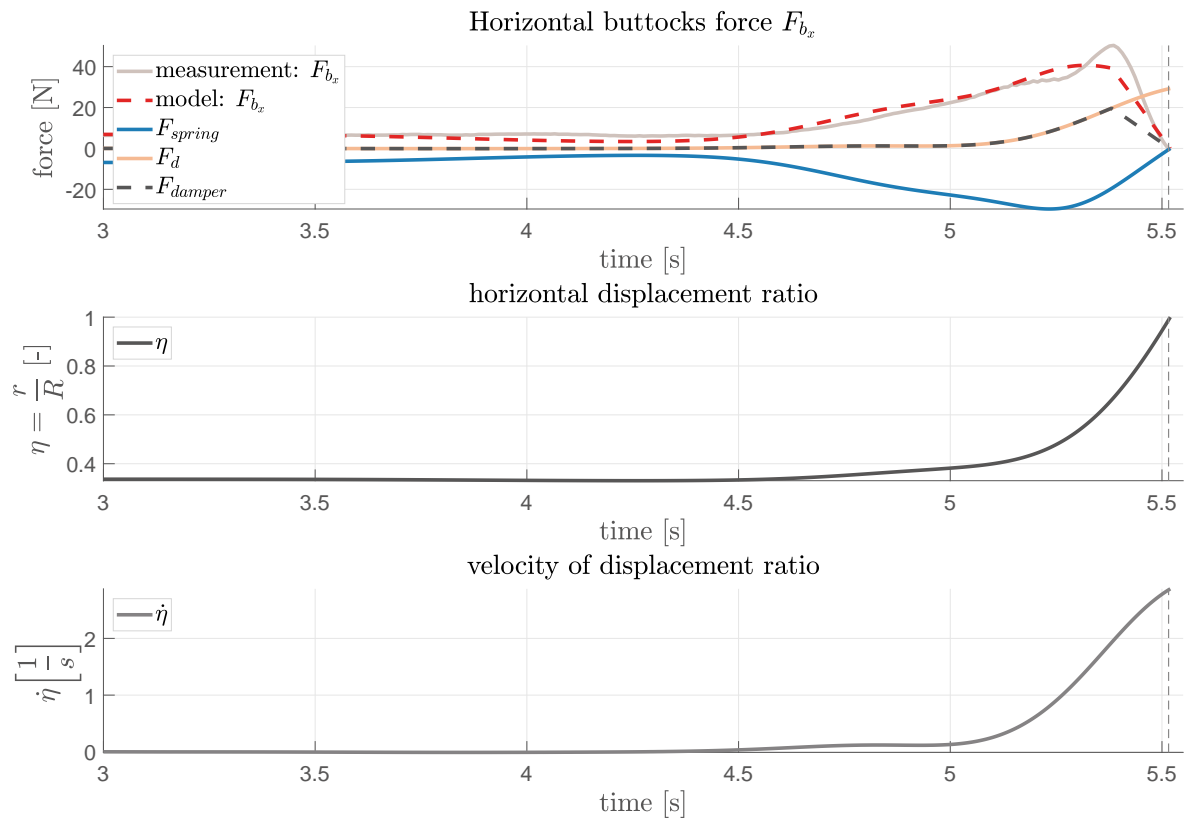


Figure 3.14: Approximated horizontal contact force F_{b_x} using Kelvin-Voigt model (upper plot, red dashed line) and corresponding horizontal displacement ratio (middle plot) and its velocity w.r.t. time (lower plot).

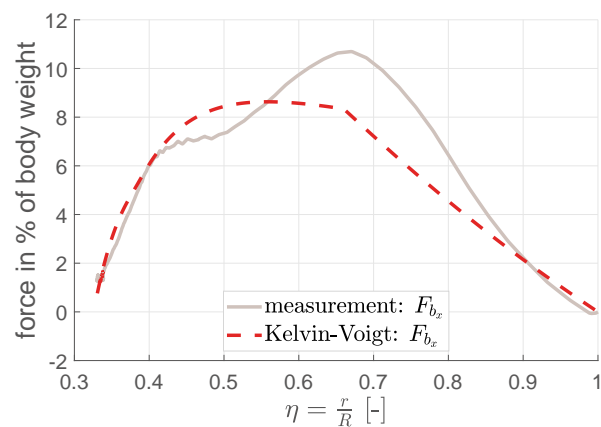


Figure 3.15: Measured and modeled horizontal contact force F_{b_x} as a percentage of body weight w.r.t. η .

3.2.4.2 Gaussian function model

As an alternate modeling approach for the buttocks force, a Gaussian function fit was performed using the MATLAB routine `fit` of `fitType` 'gauss5' with options left to default. Here, the contact force is of the form

$$F_b = a_1 \cdot e^{\left(\frac{-\hat{x}-b_1}{c_1}\right)^2} + a_2 \cdot e^{\left(\frac{-\hat{x}-b_2}{c_2}\right)^2} + a_3 \cdot e^{\left(\frac{-\hat{x}-b_3}{c_3}\right)^2} + a_4 \cdot e^{\left(\frac{-\hat{x}-b_4}{c_4}\right)^2} + a_5 \cdot e^{\left(\frac{-\hat{x}-b_5}{c_5}\right)^2} \quad (3.7)$$

until seat-off, where \hat{x} is a variable compatible with the problem and $a_1, b_1, c_1, a_2, b_2, c_2, a_3, b_3, c_3, a_4, b_4, c_4, a_5, b_5, c_5$ are the parameters, that need to be identified.

Vertical buttocks force model

For the vertical buttocks force, \hat{x} is replaced by the stretch ratio $\lambda = \frac{l}{L}$ as in eq. (3.3) and F_{b_y} is then defined as

$$F_{b_y} = \begin{cases} a_1 e^{\left(\frac{-\lambda-b_1}{c_1}\right)^2} + a_2 e^{\left(\frac{-\lambda-b_2}{c_2}\right)^2} + a_3 e^{\left(\frac{-\lambda-b_3}{c_3}\right)^2} + a_4 e^{\left(\frac{-\lambda-b_4}{c_4}\right)^2} + a_5 e^{\left(\frac{-\lambda-b_5}{c_5}\right)^2}, & \lambda < 1 \\ 0, & \text{else,} \end{cases}$$

where the parameters were found according to the values in tab. 3.4.

Parameter	a_1	a_2	a_3	a_4	a_5
Value [$kg\ m/s^2$]	179.6	433.2	$5.524e + 12$	10.55	9.619
Parameter	b_1	b_2	b_3	b_4	b_5
Value [-]	0.5201	0.6752	0.07867	0.5259	0.809
Parameter	c_1	c_2	c_3	c_4	c_5
Value [-]	0.07856	0.1988	0.08442	0.01201	0.06298

Table 3.4: Gaussian fit parameter settings for vertical contact force.

This force model is a direct fit to the measurement data depending on the stretch ratio λ . Even though this model is physically not intuitively interpretable, it provides an almost perfect fit to the actual force values. This can be seen in the comparison between the Kelvin-Voigt and the Gaussian function model for the vertical force in fig. 3.16 and in appendix D (fig. 4), where the modeled vertical contact force is also plotted w.r.t. time.

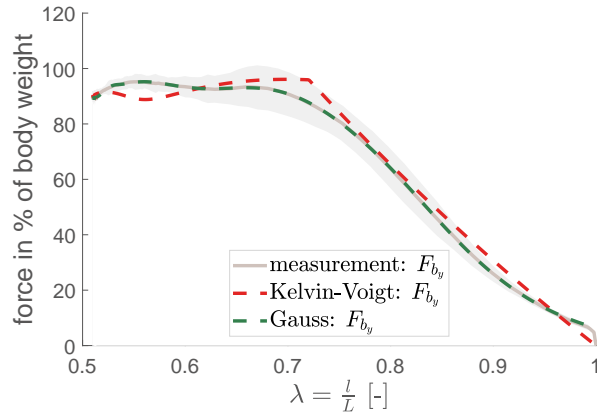


Figure 3.16: Vertical contact force F_{b_y} as a percentage of body weight w.r.t. λ : Comparison between Kelvin-Voigt (red dashed line) and Gaussian model (green dashed line) with regard to mean measured force (gray line) and standard deviation interval (gray area).

Horizontal buttocks force model

For the horizontal buttocks force \hat{x} is replaced by the displacement ratio $\eta = \frac{r}{R}$ as in eq. (3.5) and F_{b_x} is then defined as

$$F_{b_x} = \begin{cases} a_1 e^{\left(\frac{-\eta-b_1}{c_1}\right)^2} + a_2 e^{\left(\frac{-\eta-b_2}{c_2}\right)^2} + a_3 e^{\left(\frac{-\eta-b_3}{c_3}\right)^2} + a_4 e^{\left(\frac{-\eta-b_4}{c_4}\right)^2} + a_5 e^{\left(\frac{-\eta-b_5}{c_5}\right)^2}, & \eta < 1 \\ 0, & \text{else,} \end{cases}$$

where the parameters were found according to the values in tab. 3.5.

Parameter	a_1	a_2	a_3	a_4	a_5
Value [$kg\ m/s^2$]	$-1.265e + 12$	-0.9263	51.89	11.32	12.11
Parameter	b_1	b_2	b_3	b_4	b_5
Value [-]	19.4	0.6161	0.6589	0.4527	0.3976
Parameter	c_1	c_2	c_3	c_4	c_5
Value [-]	3.579	0.0391	0.2072	0.06709	0.04703

Table 3.5: Gaussian fit parameter settings for horizontal contact force.

The direct comparison between the Kelvin-Voigt and the Gaussian function model for the horizontal force is illustrated in fig. 3.17. Again, the Gaussian model provides an almost perfect fit, which can also be seen in the graph of measured and gaussian modeled horizontal force over time in appendix D (fig. 5).

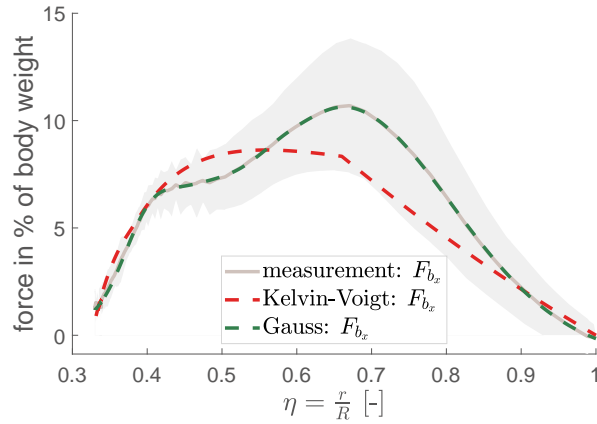


Figure 3.17: Horizontal contact force F_{b_x} as a percentage of body weight w.r.t. displacement ratio η : Comparison between Kelvin-Voigt (red dashed line) and Gaussian model (green dashed line) with regard to mean measured force (gray line) and standard deviation interval (gray area).

3.2.4.3 Discussion of buttocks force models

The contact force between chair and buttocks was measured and modeled in two different ways, with a Kelvin-Voigt model and a Gaussian function model:

The visco-hyperelastic Kelvin-Voigt model provides a possibility of representing buttocks forces through a spring-damper-element of type Mooney-Rivlin. This has a physical meaning in a sense that it can be interpreted as a mechanical model of expressing the buttocks tissue deformation behavior. However, it provides only vague approximations at best and, to some extent, they even lie outside the standard deviation area w.r.t. the experiment data (see fig. 3.16). Furthermore, the Kelvin-Voigt model has to be re-parameterized for subjects of considerably different mass.

The Gaussian function model provides plausible forces through a good fit and accurately represents the data collected in the STS-experiments. Compared to the Kelvin-Voigt model, the modeled curves are much closer to the measurements for the considered test subject, although parameters have to be re-fitted as well, if test subjects of different mass are of interest. The Gaussian function model provides a mathematical modeling approach, which is valid within the context of simulations on a purely mathematical computer basis, even though it does not provide a physical interpretation at this point. Since it is important to replicate reality in an accurate manner for simulation purposes, the Gaussian function model is utilized within the direct dynamics of the STS motion prediction in this thesis.

4 Operational space formulation and control

4.1 Operational space dynamic model

In case of a non-redundant manipulator the dynamic model can be determined using the Lagrange formulation with operational space variables, since these variables provide a set of generalized coordinates, so that the system motion can be described completely. For a redundant manipulator, a set of independent operational coordinates describing the end-effector's location and orientation is not enough to fully depict the manipulator's configuration since the operational variables do not constitute a complete set of generalized coordinates for the description of the entire system dynamics [107, 40]. Hence the complete dynamic behavior of the redundant system cannot be described by a dynamic model in operational space, as internal motions of the structure can occur without altering the end-effector's pose. Yet, the end-effector's dynamic behavior can still be constituted by establishing its equations of motion in operational space. A general approach based on the universal dynamic model in joint space (here without the consideration of external forces for reasons of simplicity) applies to both non-redundant as well as redundant manipulators [107] and will be shown hereafter.

Solving eq. (2.14) for the joint accelerations yields

$$\ddot{\mathbf{q}} = -\mathbf{A}^{-1}(\mathbf{q})\mathbf{b}(\dot{\mathbf{q}}, \mathbf{q}) + \mathbf{A}^{-1}(\mathbf{q})\mathbf{g}(\mathbf{q}) + \mathbf{A}^{-1}(\mathbf{q})\mathbf{J}^T(\mathbf{q})\mathbf{F} \quad (4.1)$$

with the simple force transformation of the operational forces \mathbf{F} that are produced by submitting the manipulator to the corresponding joint forces (see fig. 2.4 in section 2.2.3)

$$\mathbf{\Gamma} = \mathbf{J}^T(\mathbf{q})\mathbf{F}.$$

Inserting eq. (4.1) in the second-order differential kinematics equation (2.3) results in

$$\ddot{\mathbf{x}} = -\mathbf{J}\mathbf{A}^{-1}\mathbf{b} + \mathbf{J}\mathbf{A}^{-1}\mathbf{g} + \mathbf{J}\mathbf{A}^{-1}\mathbf{J}^T\mathbf{F} + \dot{\mathbf{J}}\dot{\mathbf{q}} \quad (4.2)$$

where functional dependencies are left out for conciseness. The operational forces then are

$$(\mathbf{J}\mathbf{A}^{-1}\mathbf{J}^T)^{-1}\ddot{\mathbf{x}} + (\mathbf{J}\mathbf{A}^{-1}\mathbf{J}^T)^{-1}\mathbf{J}\mathbf{A}^{-1}\mathbf{b} - (\mathbf{J}\mathbf{A}^{-1}\mathbf{J}^T)^{-1}\dot{\mathbf{J}}\dot{\mathbf{q}} - (\mathbf{J}\mathbf{A}^{-1}\mathbf{J}^T)^{-1}\mathbf{J}\mathbf{A}^{-1}\mathbf{g} = \mathbf{F}. \quad (4.3)$$

This leads to the operational space dynamic model in the notation according to Khatib [39, 40, 49, 52]:

$$\boxed{\Lambda_r(\mathbf{q})\ddot{\mathbf{x}} + \boldsymbol{\mu}_r(\mathbf{q}, \dot{\mathbf{q}}) - \mathbf{p}_r(\mathbf{q}) = \mathbf{F}} \quad (4.4)$$

with

$$\Lambda_r(\mathbf{q}) = (\mathbf{J}(\mathbf{q}) \mathbf{A}^{-1}(\mathbf{q}) \mathbf{J}^T(\mathbf{q}))^{-1}, \quad (4.5)$$

$$\boldsymbol{\mu}_r(\mathbf{q}, \dot{\mathbf{q}}) = \Lambda_r(\mathbf{q}) \mathbf{J}(\mathbf{q}) \mathbf{A}^{-1}(\mathbf{q}) \mathbf{b}(\mathbf{q}, \dot{\mathbf{q}}) - \Lambda_r(\mathbf{q}) \dot{\mathbf{J}}(\mathbf{q}, \dot{\mathbf{q}}) \dot{\mathbf{q}}, \quad (4.6)$$

$$\mathbf{p}_r(\mathbf{q}) = \Lambda_r(\mathbf{q}) \mathbf{J}(\mathbf{q}) \mathbf{A}^{-1}(\mathbf{q}) \mathbf{g}(\mathbf{q}). \quad (4.7)$$

Eq. (4.4) describes the dynamic response of the end-effector to the application of an operational force \mathbf{F} . The equations of motion in operational space are formally analogous to the equations of motion in joint space. $\Lambda_r(\mathbf{q})$ can be considered to be a pseudo kinetic energy matrix which is symmetric, positive definite and of dimension $m \times m$, similar to matrix $\mathbf{A}(\mathbf{q})$. The centrifugal, gyroscopic and Coriolis forces acting on the end-effector are represented by $\boldsymbol{\mu}_r(\mathbf{q}, \dot{\mathbf{q}})$, and $\mathbf{p}_r(\mathbf{q})$ are the gravitational forces. It is worth mentioning that the matrix $\mathbf{J} \mathbf{A}^{-1} \mathbf{J}^T$ is only invertible if \mathbf{J} has full-rank, thus the manipulator configuration has to be non-singular.

In a non-singular configuration of a non-redundant manipulator, the expressions eq. (4.5) to eq. (4.7) simplify to:

$$\Lambda(\mathbf{q}) = \mathbf{J}(\mathbf{q})^{-T} \mathbf{A}(\mathbf{q}) \mathbf{J}(\mathbf{q})^{-1}, \quad (4.8)$$

$$\boldsymbol{\mu}(\mathbf{q}, \dot{\mathbf{q}}) = \mathbf{J}(\mathbf{q})^{-T} \mathbf{b}(\mathbf{q}, \dot{\mathbf{q}}) - \Lambda(\mathbf{q}) \dot{\mathbf{J}}(\mathbf{q}, \dot{\mathbf{q}}) \dot{\mathbf{q}}, \quad (4.9)$$

$$\mathbf{p}(\mathbf{q}) = \mathbf{J}(\mathbf{q})^{-T} \mathbf{g}(\mathbf{q}). \quad (4.10)$$

According to Khatib [42, 43], the operational space formulation provides a means of dealing with kinematic singularities. In the neighborhood of singularities the manipulator can be treated as redundant w.r.t. the motion of the end-effector within the subspace of operational space orthogonal to the singular direction. This approach, however, is not pursued in this thesis, since the four-link planar model is by definition redundant.

4.2 Direct dynamics in operational space

With regard to the operational space, the *direct dynamics* problem refers to the calculation of the end-effector motion in terms of $\ddot{\mathbf{x}}(t)$, $\dot{\mathbf{x}}(t)$ and $\mathbf{x}(t)$ on the basis of given joint torques $\boldsymbol{\Gamma}(t)$. However, eq. (4.4) cannot be utilized directly since eq. (2.16) only has a solution if $\boldsymbol{\Gamma}(t) \in \mathcal{R}(\mathbf{J}^T)$ (see figure 2.4). That is why the solution to the problem is typically gathered in joint space through eq. (2.14) in order to obtain $\mathbf{q}, \dot{\mathbf{q}}$

and $\ddot{\mathbf{q}}$, whereas \mathbf{x} , $\dot{\mathbf{x}}$ and $\ddot{\mathbf{x}}$ respectively are then calculated with the direct kinematics equations.

4.3 Inverse dynamics in operational space

The *inverse dynamic* problem in operational space consists of the resolution of the joint torques $\mathbf{\Gamma}(t)$ that are needed to achieve desired end-effector motions specified by $\mathbf{x}_{\text{des}}(t)$, $\dot{\mathbf{x}}_{\text{des}}(t)$ and $\ddot{\mathbf{x}}_{\text{des}}(t)$. There exist two solution approaches that take redundancy resolution into account. One solves redundancy resolution at dynamic level as in [107] or in Khatib's original formulation, where the joint torques can be computed by the general solution:

$$\mathbf{\Gamma} = \mathbf{J}^T(\mathbf{q})\mathbf{F} + [\mathbf{I} - \mathbf{J}^T(\mathbf{q})\bar{\mathbf{J}}^T(\mathbf{q})]\mathbf{\Gamma}_0, \quad (4.11)$$

where \mathbf{I} is the $n \times n$ identity matrix and $\mathbf{\Gamma}_0$ is a vector of arbitrary joint torques. $\bar{\mathbf{J}}(\mathbf{q})$ represents the right pseudo-inverse of the Jacobian matrix that is weighted by the inertia matrix:

$$\bar{\mathbf{J}} = \mathbf{A}^{-1} \mathbf{J}^T (\mathbf{J} \mathbf{A}^{-1} \mathbf{J}^T)^{-1} \quad (4.12)$$

and, physically speaking, minimizes the instantaneous kinetic energy of the system. As the projector matrix \mathbf{P} in the null space of \mathbf{J} was chosen according to eq. (2.13), the choice of the generalized pseudo-inverse in this case is bound to be $\bar{\mathbf{J}}$ in order to be consistent with the dynamic equations of the manipulator and end-effector [42]. As discussed by Khatib, the inertia weighted generalized inverse is the only pseudo-inverse that is dynamically consistent with the task in that no additional end-effector acceleration occurs for any $\mathbf{\Gamma}_0$. A derivation of these circumstances can be seen in appendix E. In analogy to eq. (2.12), the torques in eq. (4.11) are classified by a minimum-norm term and a homogeneous solution. The minimum-norm term corresponds to forces acting at the end-effector with \mathbf{F} used as the control vector. The homogeneous solution contains joint torques that act along directions of the null space, and thus do not affect the resulting forces reflected at the end-effector, since only the internal joint motions are controlled by the selection of $\mathbf{\Gamma}_0$.

Minimizing the system's kinetic energy makes sense for applications in the field of robotics. However, in biomechanics it does not necessary apply to every human action. Finding the fundamental objective that is processed by the neural system and that underlies a specific motion comprises an optimization problem in itself and is solved in operational space control by the choice of a suitable pseudo-inverse of the Jacobian

matrix \mathbf{J}^\dagger . A strategy, that does not restrict the choice of the pseudo-inverse, solves redundancy resolution at kinematic level. Here, the corresponding inverse kinematics problem, which is embedded in the feedback loop of the control scheme, is resolved first to determine the joint variables, on the basis of which the required torques can be computed with the inverse dynamics model (eq. (2.14)) in joint space. Such a solution approach is utilized for the STS motion generation and will be presented in the next section.

4.4 Operational space control method

To solve the direct dynamics problem in joint space, an inverse dynamics control in operational space is utilized as shown in fig. 4.1.

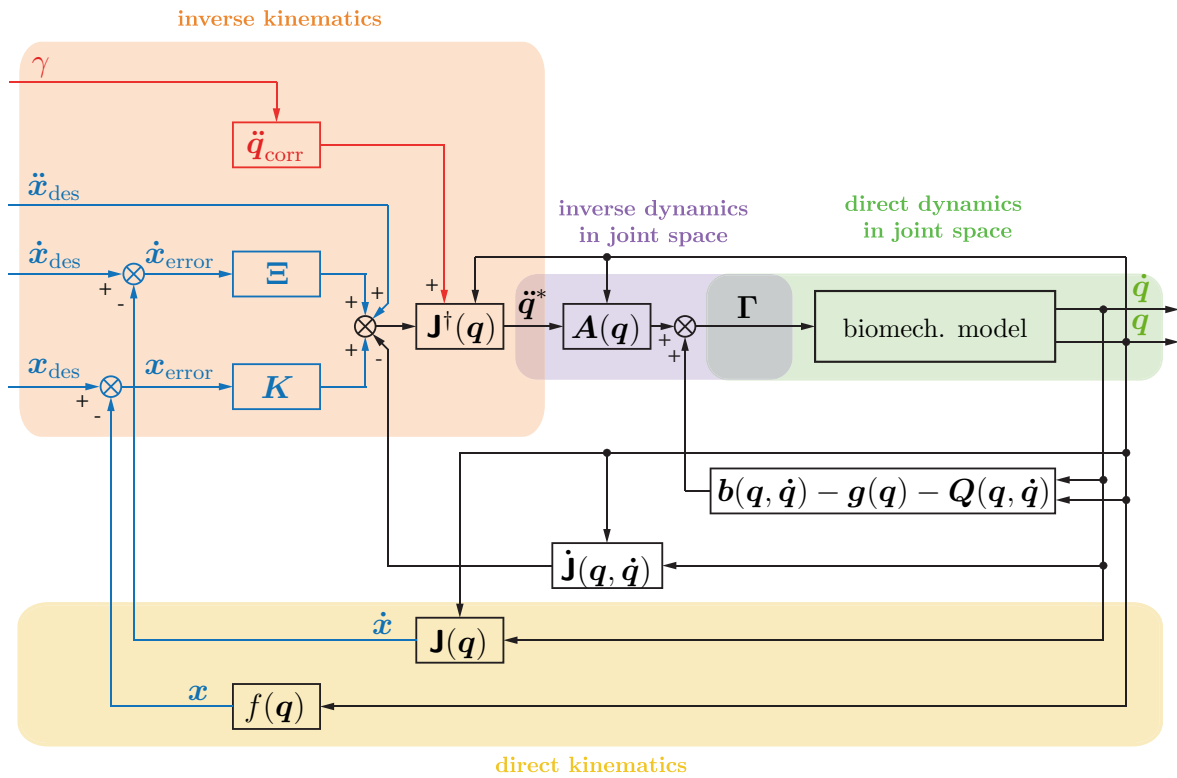


Figure 4.1: Block scheme of inverse dynamics control in operational space, inspired by [107].

The operational space control method relies on the specification of the desired end-effector motion regarding operational space variables $\mathbf{x}_{des}(t)$, $\dot{\mathbf{x}}_{des}(t)$ and $\ddot{\mathbf{x}}_{des}(t)$ in order for the end-effector to track an operational space trajectory. Starting from measured joint space variables, the actual end-effector coordinates are calculated online through

direct kinematics functions $f(\mathbf{q})$ and $\mathbf{J}(\mathbf{q})$. The operational space error dynamics is then computed with the motion control law in operational space

$$\ddot{\mathbf{x}}^* = \ddot{\mathbf{x}}_{\text{des}} + \mathbf{\Xi}(\dot{\mathbf{x}}_{\text{des}} - \dot{\mathbf{x}}) + \mathbf{K}(\mathbf{x}_{\text{des}} - \mathbf{x}) \quad (4.13)$$

as a function of the desired and the actual motion, where the end-effector position error in fig. 4.1 is defined by $\mathbf{x}_{\text{error}} = \mathbf{x}_{\text{des}} - \mathbf{x}$ and the velocity error by $\dot{\mathbf{x}}_{\text{error}} = \dot{\mathbf{x}}_{\text{des}} - \dot{\mathbf{x}}$, respectively. $\mathbf{\Xi}$ and \mathbf{K} describe positive definite and diagonal gain matrices, that determine the error convergence rate to zero. The control law characterizes a feedback loop where coordinate transformations replace trajectory inversion, as opposed to joint space control schemes [107].

In this thesis, a redundancy handling technique is embedded within the inverse kinematics at acceleration level. Analogous to the approach described in section 2.1.2.1, solving eq. (2.3) for $\ddot{\mathbf{q}}$ in case of a redundant manipulator yields

$$\ddot{\mathbf{q}} = \mathbf{J}^\dagger(\ddot{\mathbf{x}} - \dot{\mathbf{J}}\dot{\mathbf{q}}) + \ddot{\mathbf{q}}_{\text{corr}} \quad (4.14)$$

with a general pseudo-inverse of the Jacobian \mathbf{J}^\dagger , that complies with $\mathbf{J}\mathbf{J}^\dagger = \mathbf{I}$, and a correction term $\ddot{\mathbf{q}}_{\text{corr}}$ that fulfills

$$\mathbf{J}\ddot{\mathbf{q}}_{\text{corr}} = \mathbf{0}.$$

This way, $\ddot{\mathbf{q}}_{\text{corr}}$ lies within the null space of $\mathbf{J}(\mathbf{q})$. Thus, $\ddot{\mathbf{q}}_{\text{corr}}$ is considered a redundancy resolution term that affects manipulator posture without altering end-effector motion. In order to influence the posture within the null space, a specific input γ is inserted into the correction term. The choice of γ and $\ddot{\mathbf{q}}_{\text{corr}}$ for this thesis will be illustrated in detail below.

Inserting eq. (4.13) in eq. (4.14), where the desired end-effector motion $\ddot{\mathbf{x}}^*$ serves as the control input of the decoupled end-effector, gives the general description of desired joint accelerations that are necessary for the manipulator to track a predefined end-effector trajectory. The equation can be partitioned in a control part and a correction part:

$$\ddot{\mathbf{q}}^* = \underbrace{\mathbf{J}^\dagger(\ddot{\mathbf{x}}^* - \dot{\mathbf{J}}\dot{\mathbf{q}})}_{\substack{\text{control part} \\ \ddot{\mathbf{q}}_{\text{contr}}}} + \underbrace{\ddot{\mathbf{q}}_{\text{corr}}}_{\substack{\text{correction part} \\ \text{with } \mathbf{J}\ddot{\mathbf{q}}_{\text{corr}} \stackrel{!}{=} \mathbf{0}}} . \quad (4.15)$$

Ultimately, based on the desired joint motion the corresponding joint torques $\mathbf{\Gamma}$ are generated using the inverse dynamics model in joint space.

Choice of correction part $\ddot{\mathbf{q}}_{\text{corr}}$ and projector matrix \mathbf{P}

Analogous to eq. (2.12), the correction part is of the form

$$\ddot{\mathbf{q}}_{\text{corr}} = \mathbf{P} \ddot{\mathbf{q}}_{\text{any}}. \quad (4.16)$$

The projector matrix \mathbf{P} can have any form, as long as it projects onto the null space of \mathbf{J} so that the conditions $\mathbf{J} \ddot{\mathbf{q}}_{\text{corr}} = \mathbf{0}$ and $\mathcal{R}(\mathbf{P}) \equiv \mathcal{N}(\mathbf{J})$ are fulfilled, as mentioned earlier in chapter 2.1.1.3.

In this thesis, the projector matrix is chosen to be

$$\mathbf{P} = N(\mathbf{J}) N(\mathbf{J})^T, \quad (4.17)$$

where $N(\mathbf{J}) = [\mathbf{n}_1 \ \mathbf{n}_2 \ \dots \ \mathbf{n}_s]$, with $\mathbf{n}_i \in \mathbb{R}^n$, $1 \leq i \leq s \in \mathbb{N}$, is a set of orthonormal basis vectors for the null space of \mathbf{J} . Since $N(\mathbf{J})$ is dependent on \mathbf{J} , it does not have the full dimension in the degenerate case. The linear combination $N(\mathbf{J}) N(\mathbf{J})^T$ within the null space of \mathbf{J} artificially inflates the dimension and provides the necessary square matrix of dimension $n \times n$ in order to fulfill:

$$\ddot{\mathbf{q}}_{\text{corr}} = N(\mathbf{J}) N(\mathbf{J})^T \ddot{\mathbf{q}}_{\text{any}}, \quad (4.18)$$

where $\ddot{\mathbf{q}}_{\text{any}}$ is disassembled by \mathbf{P} in the directions of the unit vectors \mathbf{n}_i . Thereby, $\ddot{\mathbf{q}}_{\text{corr}}$ contains as much as possible of $\ddot{\mathbf{q}}_{\text{any}}$, since only those parts of $\ddot{\mathbf{q}}_{\text{any}}$ get blocked out that are not displayable in the basis of the null space of the Jacobian matrix. This definition of \mathbf{P} represents an alternate way of projecting the vector of arbitrary joint accelerations in the null space of the Jacobian (compare eq. (2.13) at velocity level) so as to comply with the primary constraint. Furthermore, the representation method is independent of the choice of the pseudo-inverse of the Jacobian.

Task and posture decomposition

Eq. (4.15) allows for a decomposition of the total joint acceleration into two dynamically decoupled vectors, that are the acceleration which corresponds to the commanded end-effector performance, termed the task, and the acceleration that projects into the null space of the task and only affects postural behavior, which is referred to as the posture or subtask.

The *task control* (index t)

$$\ddot{\mathbf{x}}_t^* = \ddot{\mathbf{x}}_{t_{\text{des}}} + \mathbf{\Xi}_t (\dot{\mathbf{x}}_{t_{\text{des}}} - \dot{\mathbf{x}}_t) + \mathbf{K}_t (\mathbf{x}_{t_{\text{des}}} - \mathbf{x}_t) \quad (4.19)$$

put in eq. (4.14) yields

$$\ddot{\mathbf{q}}_t^* = \underbrace{\mathbf{J}_t^\dagger (\ddot{\mathbf{x}}_t^* - \dot{\mathbf{J}}_t \dot{\mathbf{q}})}_{\ddot{\mathbf{q}}_{t\text{contr}}} + N(\mathbf{J}_t) N(\mathbf{J}_t)^T \boxed{\ddot{\mathbf{q}}_{\text{any}}} \quad (4.20)$$

with \mathbf{J}_t^\dagger being the pseudo-inverse of the task Jacobian \mathbf{J}_t and $N(\mathbf{J}_t)$ equal to the orthonormal basis of the null space of the task Jacobian \mathbf{J}_t . The remaining freedom of the internal motion can now be assigned to various criteria related to the manipulator posture [54]. Therefore, $\ddot{\mathbf{q}}_{\text{any}}$ is chosen as to characterize a desired postural joint motion.

So, for the *posture control* (index p), the same idea of control

$$\ddot{\mathbf{x}}_p^* = \ddot{\mathbf{x}}_{p\text{des}} + \mathbf{\Xi}_p (\dot{\mathbf{x}}_{p\text{des}} - \dot{\mathbf{x}}_p) + \mathbf{K}_p (\mathbf{x}_{p\text{des}} - \mathbf{x}_p) \quad (4.21)$$

regarding a predefined secondary task behavior is inserted in eq. (4.14), yielding

$$\ddot{\mathbf{q}}_p^* = \mathbf{J}_p^\dagger (\ddot{\mathbf{x}}_p^* - \dot{\mathbf{J}}_p \dot{\mathbf{q}}). \quad (4.22)$$

Here, \mathbf{J}_p refers to the posture Jacobian which can be considered a secondary task with a different operational point of another end-effector in order to control manipulator posture.

In order to compensate for an acceleration induced by the task in the posture space, one can choose

$$\boxed{\ddot{\mathbf{q}}_{\text{any}}} \equiv \ddot{\mathbf{q}}_p^* - \ddot{\mathbf{q}}_{t\text{contr}} \quad (4.23)$$

similar to Khatib et al. in [54]. Then the overall control law becomes

$$\ddot{\mathbf{q}}_t^* = \underbrace{\mathbf{J}_t^\dagger (\ddot{\mathbf{x}}_t^* - \dot{\mathbf{J}}_t \dot{\mathbf{q}})}_{\ddot{\mathbf{q}}_{\text{task}}} + \underbrace{N(\mathbf{J}_t) N(\mathbf{J}_t)^T (\ddot{\mathbf{q}}_p^* - \ddot{\mathbf{q}}_{t\text{contr}})}_{\ddot{\mathbf{q}}_{\text{posture}}}. \quad (4.24)$$

This way, a task prioritization is achieved, where the posture goal is attained as long as it does not conflict with the primary task. In general, the approach can be extended by multiple subtasks to be controlled.

Finally, at force level the control generalized forces submit to

$$\mathbf{\Gamma} = \underbrace{\mathbf{A} \ddot{\mathbf{q}}_{t\text{contr}} + \mathbf{b} - \mathbf{g} - \mathbf{Q}}_{\mathbf{\Gamma}_{\text{task}}} + \underbrace{\mathbf{A} N(\mathbf{J}_t) N(\mathbf{J}_t)^T (\ddot{\mathbf{q}}_p^* - \ddot{\mathbf{q}}_{t\text{contr}})}_{\mathbf{\Gamma}_{\text{posture}}}. \quad (4.25)$$

This decomposition of the overall control of a mechanism into dynamically decoupled task behavior and posture behavior was introduced by Brock and Khatib at force level

[5]. For reasons of comparison, the formulation is shown below:

$$\boldsymbol{\Gamma} = \underbrace{\mathbf{J}^T(\mathbf{q})\mathbf{F}}_{\boldsymbol{\Gamma}_{\text{task}}} + \underbrace{[\mathbf{I} - \mathbf{J}^T(\mathbf{q})\bar{\mathbf{J}}^T(\mathbf{q})]}_{\boldsymbol{\Gamma}_{\text{posture}}}\boldsymbol{\Gamma}_{\text{desposture}}. \quad (4.26)$$

According to the authors, the dynamically consistent pseudo-inverse $\bar{\mathbf{J}}$ (see eq. (4.12)) is used to minimize the manipulator's instantaneous kinetic energy, as in eq. (4.11). The desired posture torque is introduced by $\boldsymbol{\Gamma}_{\text{desposture}}$, which, projected into the null space, yields the posture torque $\boldsymbol{\Gamma}_{\text{posture}}$ that is applied to the manipulator and consequently does not interfere with the task dynamics. In general this approach can be extended by other posture related torques like obstacle avoidance and constraint satisfaction performed in the null space of the task as to guarantee task-consistent behavior. However, the integration of task execution, obstacle avoidance and posture behavior generally can only be realized as long as the torques that are mapped into the null space produce sufficient motion to achieve the desired overall behavior [5, 50, 105].

4.5 Application to quadruple pendulum model performing STS motion

The control method presented above was applied to the quadruple pendulum through eq. (4.24). The aforementioned control instances, considering the primary task and a subtask that is to be controlled in the posture space, are described as follows.

4.5.1 Task definition for STS motion

The primary *task* refers to the desired end-effector motion described as the model's head trajectory (cf. fig. 4.2), i.e. the path with specified velocities and accelerations at each point. The time sequence of these variables is to be followed and given as input to the control method.

If all three possible command variables for the end-effector position and orientation of the model in the sagittal plane are specified, i.e. the end-effector positions $x_{t_{\text{des}}}$, $y_{t_{\text{des}}}$ of the origin of \mathcal{K}_e w.r.t. the base frame \mathcal{K}_0 and orientation $\varphi_{t_{\text{des}}}$ of \mathcal{K}_e as well as corresponding velocities $\dot{x}_{t_{\text{des}}}$, $\dot{y}_{t_{\text{des}}}$, $\dot{\varphi}_{t_{\text{des}}}$ and accelerations $\ddot{x}_{t_{\text{des}}}$, $\ddot{y}_{t_{\text{des}}}$, $\ddot{\varphi}_{t_{\text{des}}}$, then the control law is:

$$\begin{bmatrix} \ddot{x}_t^* \\ \ddot{y}_t^* \\ \ddot{\varphi}_t^* \end{bmatrix} = \begin{bmatrix} \ddot{x}_{t_{\text{des}}} \\ \ddot{y}_{t_{\text{des}}} \\ \ddot{\varphi}_{t_{\text{des}}} \end{bmatrix} + \begin{bmatrix} \xi_1 & 0 & 0 \\ 0 & \xi_2 & 0 \\ 0 & 0 & \xi_3 \end{bmatrix} \cdot \begin{bmatrix} \dot{x}_{t_{\text{des}}} - \dot{x}_t \\ \dot{y}_{t_{\text{des}}} - \dot{y}_t \\ \dot{\varphi}_{t_{\text{des}}} - \dot{\varphi}_t \end{bmatrix} + \begin{bmatrix} k_1 & 0 & 0 \\ 0 & k_2 & 0 \\ 0 & 0 & k_3 \end{bmatrix} \cdot \begin{bmatrix} x_{t_{\text{des}}} - x_t \\ y_{t_{\text{des}}} - y_t \\ \varphi_{t_{\text{des}}} - \varphi_t \end{bmatrix}. \quad (4.27)$$

In eq. (4.27), x_t, y_t , and φ_t as well as \dot{x}_t, \dot{y}_t and $\dot{\varphi}_t$ describe the actual end-effector position and orientation w.r.t. the base frame \mathcal{K}_0 as well as corresponding velocities, respectively. The position gain factor k_1 refers to the end-effector x -position error, k_2 refers to the position gain in corresponding y -direction and k_3 is the gain factor that relates to the end-effector orientation error. Same references apply to the velocity gains ξ_1, ξ_2 and ξ_3 at velocity level. In total, six gain factors have to be defined for the direct dynamics of the STS-task behavior. The input in terms of end-effector kinematics was computed based on the model geometry and joint angle data $\mathbf{q}, \dot{\mathbf{q}}$ and $\ddot{\mathbf{q}}$ of a measurement.

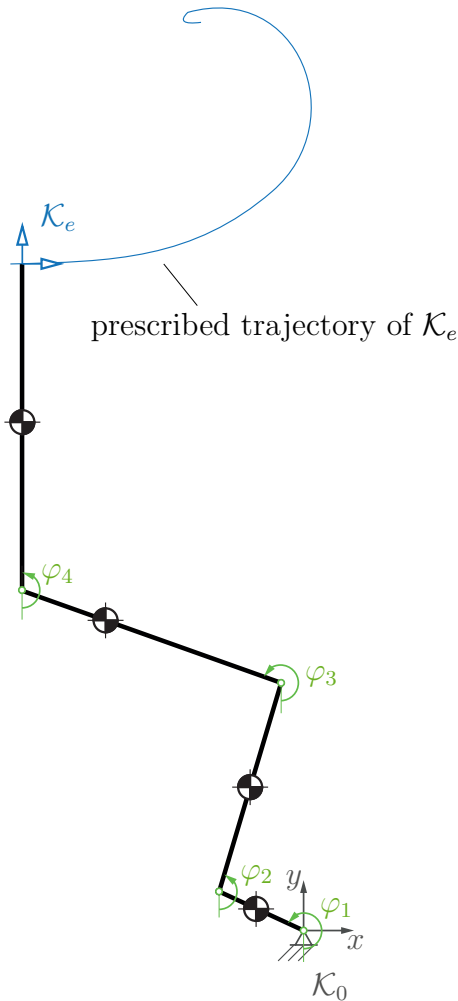


Figure 4.2: Quadruple pendulum model with schematic end-effector trajectory.

First, as in Khatib [43, 49], the pseudo-inverse for the task was chosen to be the inertia weighted generalized inverse:

$$\mathbf{J}_t^\dagger = \mathbf{A}^{-1} \mathbf{J}_t^T (\mathbf{J}_t \mathbf{A}^{-1} \mathbf{J}_t^T)^{-1}. \quad (4.28)$$

In order to test the effect of choosing a different pseudo-inverse, a general weighted pseudo-inverse

$$\mathbf{J}_t^\dagger = \mathbf{W}^{-1} \mathbf{J}_t^T (\mathbf{J}_t \mathbf{W}^{-1} \mathbf{J}_t^T)^{-1}, \quad (4.29)$$

that locally minimizes the norm of weighted joint accelerations was tested as well for a bandwidth of different values and combinations of the diagonal entries of the symmetric positive definite weighting matrix \mathbf{W} of dimension $n \times n$. As it turned out for values specified close to zero up to $1.0e^4$, the weighting does not seem to have any influence within task control and the choice between eq. (4.28) and eq. (4.29) does not yield any differences in the simulation results of the STS motion. That is why the inertia weighted pseudo-inverse of eq. (4.28) was chosen for the task control. Instead, the accuracy of simulation results in terms of following the desired end-effector trajectory is greatly influenced by the choice of the gain factors k_i , ξ_i for the task control.

4.5.2 Posture definition for STS motion

In order for the redundant manipulator to perform the STS motion under biomechanical constraints, the angular acceleration of the foot $\ddot{\varphi}_p^*$ was chosen as the *posture* control. With the aim of regulating the model through as few predefined guidelines as possible, only the foot orientation $\varphi_{p_{\text{des}}}$ of the standing model was used as a constant input variable. The foot center of mass position then becomes redundant to pass as an input. Since the foot should not move any more in stable standing, desired angular velocity $\dot{\varphi}_{p_{\text{des}}}$ and acceleration $\ddot{\varphi}_{p_{\text{des}}}$ of the foot were set to zero. The control law for the posture was then reduced from its general matrix form to a scalar:

$$\begin{aligned} \begin{bmatrix} \ddot{x}_p^* \\ \ddot{y}_p^* \\ \ddot{\varphi}_p^* \end{bmatrix} &= \begin{bmatrix} \ddot{x}_{p_{\text{des}}} \\ \ddot{y}_{p_{\text{des}}} \\ \ddot{\varphi}_{p_{\text{des}}} \end{bmatrix} + \begin{bmatrix} \xi_{p_1} & 0 & 0 \\ 0 & \xi_{p_2} & 0 \\ 0 & 0 & \xi_{p_3} \end{bmatrix} \cdot \begin{bmatrix} \dot{x}_{p_{\text{des}}} - \dot{x}_p \\ \dot{y}_{p_{\text{des}}} - \dot{y}_p \\ \dot{\varphi}_{p_{\text{des}}} - \dot{\varphi}_p \end{bmatrix} + \begin{bmatrix} k_{p_1} & 0 & 0 \\ 0 & k_{p_2} & 0 \\ 0 & 0 & k_{p_3} \end{bmatrix} \cdot \begin{bmatrix} x_{p_{\text{des}}} - x_p \\ y_{p_{\text{des}}} - y_p \\ \varphi_{p_{\text{des}}} - \varphi_p \end{bmatrix} \\ \Leftrightarrow \begin{bmatrix} 0 \\ 0 \\ \ddot{\varphi}_p^* \end{bmatrix} &= \begin{bmatrix} 0 \\ 0 \\ 0 \end{bmatrix} + \begin{bmatrix} \xi_{p_1} & 0 & 0 \\ 0 & \xi_{p_2} & 0 \\ 0 & 0 & \xi_{p_3} \end{bmatrix} \cdot \begin{bmatrix} 0 \\ 0 \\ 0 - \dot{\varphi}_p \end{bmatrix} + \begin{bmatrix} k_{p_1} & 0 & 0 \\ 0 & k_{p_2} & 0 \\ 0 & 0 & k_{p_3} \end{bmatrix} \cdot \begin{bmatrix} 0 \\ 0 \\ \varphi_{p_{\text{des}}} - \varphi_p \end{bmatrix} \\ \Leftrightarrow \ddot{\varphi}_p^* &= -\xi_{p_3} \dot{\varphi}_p + k_{p_3} (\varphi_{p_{\text{des}}} - \varphi_p). \end{aligned} \quad (4.30)$$

This way, only the two gain factors $\xi_{p_3} = \xi_{\text{posture}}$ and $k_{p_3} = k_{\text{posture}}$ have to be defined for the posture direct dynamics. The constant value for $\varphi_{p_{\text{des}}}$ was taken from measurement data.

For the posture control, three different pseudo-inverses of the postural Jacobian matrix were tested. Those are

- (a) the inertia weighted pseudo-inverse:

$$\mathbf{J}_p^\dagger = \mathbf{A}^{-1} \mathbf{J}_p^T (\mathbf{J}_p \mathbf{A}^{-1} \mathbf{J}_p^T)^{-1} \quad (4.31)$$

- (b) the weighted pseudo-inverse, that results in locally minimizing the norm of weighted joint accelerations:

$$\mathbf{J}_p^\dagger = \mathbf{W}^{-1} \mathbf{J}_p^T (\mathbf{J}_p \mathbf{W}^{-1} \mathbf{J}_p^T)^{-1}, \quad (4.32)$$

- (c) and a general pseudo-inverse with tuned entries under the condition that

$$\mathbf{J}_p \mathbf{J}_p^\dagger = \mathbf{I}. \quad (4.33)$$

Since the Jacobian matrix

$$\mathbf{J}_p = \begin{bmatrix} 1.0 & 0.0 & 0.0 & 0.0 \end{bmatrix} \quad (4.34)$$

only addresses the foot orientation φ_1 , the pseudo-inverses are naturally reduced to a 4×1 vector. Furthermore, due to the specific Jacobian matrix of the posture space (eq. (4.34)), the weighted pseudo-inverse in eq. (4.32) is simplified to non weighted Moore-Penrose pseudo-inverse $\mathbf{J}_p^\dagger = \mathbf{J}_p^T (\mathbf{J}_p \mathbf{J}_p^T)^{-1}$, where $\mathbf{J}_p^\dagger = \begin{bmatrix} 1.0 & 0.0 & 0.0 & 0.0 \end{bmatrix}^T$.

4.5.3 Direct dynamics integration

The direct dynamics was based on integrating an initial value problem. The MATLAB routine `ode45` was utilized to solve the differential equations numerically over a period of time on the basis of predefined initial conditions. The solver is based on an explicit single-step Runge-Kutta(4,5) algorithm, aka the Dormand-Prince pair [82]. The initial state of the system in terms of joint angles $\mathbf{q}(t_0)$ and angular velocities $\dot{\mathbf{q}}(t_0)$ were taken from the measurement. The integration time interval was defined as 0.0 s to 7.0 s with a step size of 1 ms. Further integration options were defined as `RelTol` = 10^{-5} and `AbsTol` = 10^{-9} , while all other options were left to their default settings. The output is the STS motion in the form of a matrix of values for \mathbf{q} and $\dot{\mathbf{q}}$ corresponding to the predefined times specified in the vector of the integration time interval.

5 Simulation results

The simulation results presented in this thesis refer to an experimental STS trial where the arms are crossed over the chest and the upper body remains one entity. Based on the measurement data, the inverse dynamics was calculated for the quadruple pendulum model as a reference to the predictions.

The control scheme of fig. 4.1 was adapted to the specific motion, decomposed in task and posture control. Therefore, $\ddot{\mathbf{q}}_{\text{corr}}$ was replaced by $\ddot{\mathbf{q}}_{\text{posture}}$ that was introduced in eq. (4.24):

$$\ddot{\mathbf{q}}_{\text{posture}} = N(\mathbf{J}_t) N(\mathbf{J}_t)^T (\mathbf{J}_p^\dagger (\ddot{\mathbf{x}}_p^* - \dot{\mathbf{J}}_p \dot{\mathbf{q}}) - \mathbf{J}_t^\dagger (\ddot{\mathbf{x}}_t^* - \dot{\mathbf{J}}_t \dot{\mathbf{q}})). \quad (5.1)$$

On posture level, $\varphi_{p_{\text{des}}}$ represents the only input from outside that is applied to the posture control law $\ddot{\mathbf{x}}_p^*$ of eq. (4.21) yielding eq. (4.30), by which values for two postural gain factors are determined, as described in chapter 4. As such, $\varphi_{p_{\text{des}}}$ now replaces γ . Omitting to introduce block elements for the gain factors, the projector matrix, the postural Jacobian matrix, its pseudo-inverse and derivative as well as dispensing with internal dependencies due to reasons relating to complexity, fig. 5.1 shows the overall operational space control method for the STS motion generation.

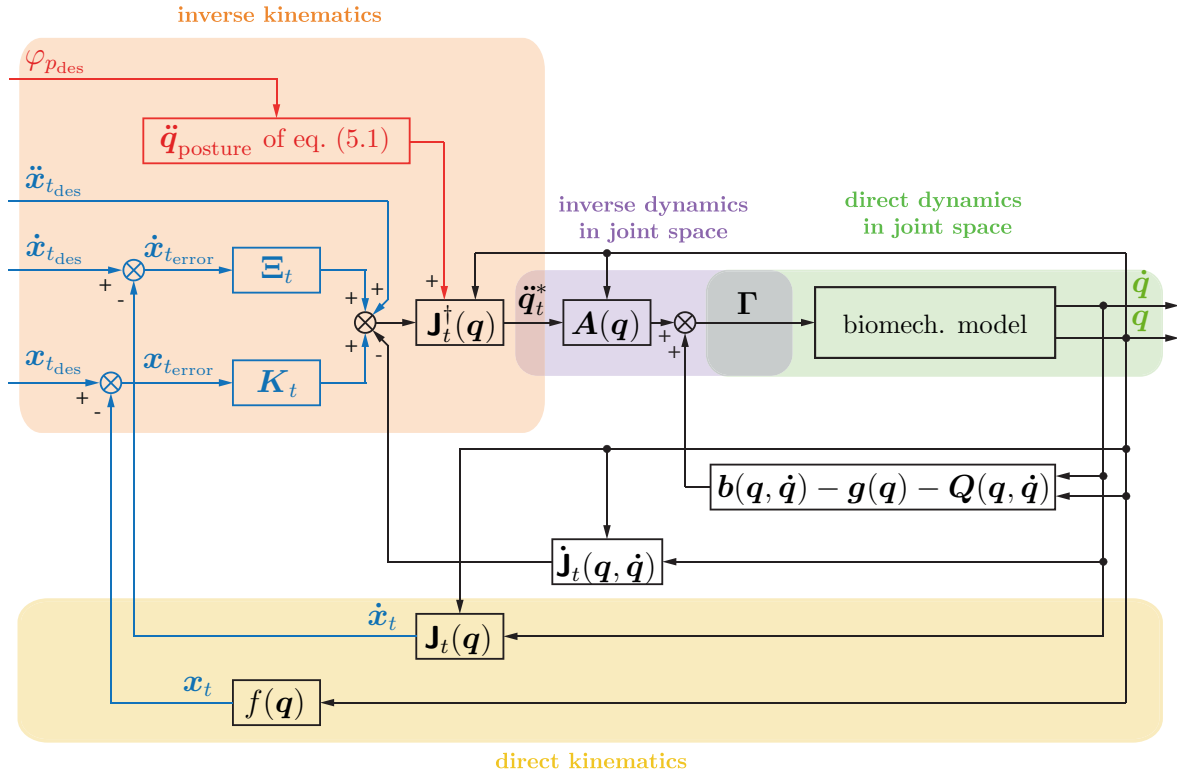


Figure 5.1: Block scheme of inverse dynamics control in operational space used for STS motion generation.

Based on this control scheme, two different simulation strategies were pursued:

First, the full set of command variables for the task x_{t_des} , y_{t_des} and φ_{t_des} along with the corresponding velocities and accelerations were given as input. The resulting task Jacobian \mathbf{J}_{t_1} for the quadruple pendulum model in this approach one was defined as

$$\mathbf{J}_{t_1} = \begin{bmatrix} l_1 \cos(\varphi_1) & l_2 \cos(\varphi_2) & l_3 \cos(\varphi_3) & l_4 \cos(\varphi_4) \\ l_1 \sin(\varphi_1) & l_2 \sin(\varphi_2) & l_3 \sin(\varphi_3) & l_4 \sin(\varphi_4) \\ 0.0 & 0.0 & 0.0 & 1.0 \end{bmatrix}. \quad (5.2)$$

As aforementioned, the inertia-weighted Jacobian matrix \mathbf{J}_t^\dagger was used for the task (eq. (4.28)). For the posture control, the foot orientation φ_{p_des} of the standing model with no angular velocity or acceleration was applied as a constant input. As far as the matrix \mathbf{J}_p^\dagger is concerned, the inertia-weighted pseudo-inverse, the joint accelerations minimizing pseudo-inverse as well as a general pseudo-inverse were tested (cf. section 4.5.2). The direct dynamics then leads to the motion of the model which is ideally supposed to be as close as possible to the solution of the inverse dynamics reference motion. An overview of this approach is given in fig. 5.2. Control parameter settings and simulation results are shown in section 5.1.

In view of reducing the number of command variables in order to have as few predefined values as possible, subsequently only $y_{t_{\text{des}}}$ and $\varphi_{t_{\text{des}}}$ and corresponding velocities as well as accelerations were regarded as input to the control method on task level (cf. fig. 5.2). The relevant task Jacobian \mathbf{J}_{t_2} of approach two then was

$$\mathbf{J}_{t_2} = \begin{bmatrix} l_1 \sin(\varphi_1) & l_2 \sin(\varphi_2) & l_3 \sin(\varphi_3) & l_4 \sin(\varphi_4) \\ 0.0 & 0.0 & 0.0 & 1.0 \end{bmatrix}. \quad (5.3)$$

The definition of the pseudo-inverse of the task Jacobian plus the posture control of the standing foot orientation remained the same. Again, the aforementioned three different posture Jacobian pseudo-inverses were tested against each other. Relevant simulation settings and results are illustrated in section 5.2.

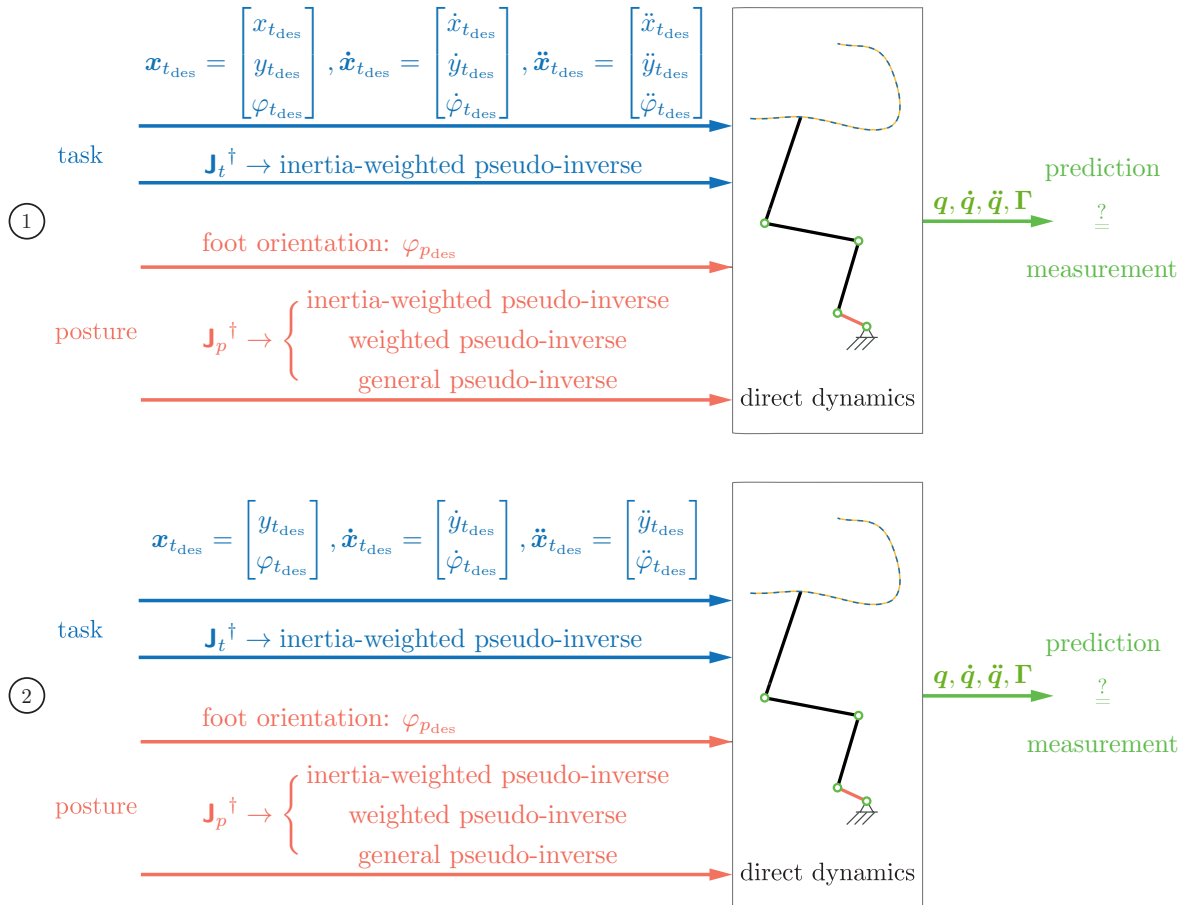


Figure 5.2: Overview of two control approaches using different sets of input variables within task and posture control.

5.1 Approach one: command variables $x_{t_{\text{des}}}$, $y_{t_{\text{des}}}$ and $\varphi_{t_{\text{des}}}$

For control approach one, six control parameters for the task as well as two control parameters for the posture are necessary in order to entirely control end-effector motion behavior through a full set of command variables in terms of $x_{t_{\text{des}}}$, $y_{t_{\text{des}}}$ and $\varphi_{t_{\text{des}}}$. The parameter settings chosen for the gain factors k_i , ξ_i within the task control of STS motion prediction as well as the gain factors k_{posture} and ξ_{posture} of the posture control are shown in tab. 5.1.

Parameter	Value
k_1	50.0
k_2	50.0
k_3	50.0
ξ_1	20.0
ξ_2	20.0
ξ_3	20.0
k_{posture}	100.0
ξ_{posture}	70.0

Table 5.1: Parameter settings for the entire control of end-effector motion behavior.

For reasons of comparability, posture gain factor settings k_{posture} and ξ_{posture} remain the same throughout the testing of various pseudo-inverses of the Jacobian matrix w.r.t. the posture control. With regard to the joint angle trajectories, the results of varying the pseudo-inverses are illustrated in fig. 5.3 for the hip, knee, ankle and toe joint angle, respectively. The joint angle time series of the measurement is depicted in gray. In order to see the effect of posture control within the direct dynamics control in general, the forward simulation was first run without any posture control (dotted lines). Then the inertia weighted pseudo-inverse was employed (dot-dashed lines), followed by the weighted pseudo-inverse (dashed lines) and a general pseudo-inverse (solid green lines). For the general pseudo-inverse, parameters were tuned to be $\mathbf{J}_p^\dagger = \begin{bmatrix} 1.0 & -0.1 & 0.1 & 0.0 \end{bmatrix}^T$. This parameter set provides good results in comparison to inverse dynamics joint angle values as well as angular velocities and accelerations with regard to the avoidance of singularities. For the sake of clarity, the display of angular rates is dispensed with in the context of posture control variations. Corresponding angular errors w.r.t. reference data is shown on the right side of the graphic.

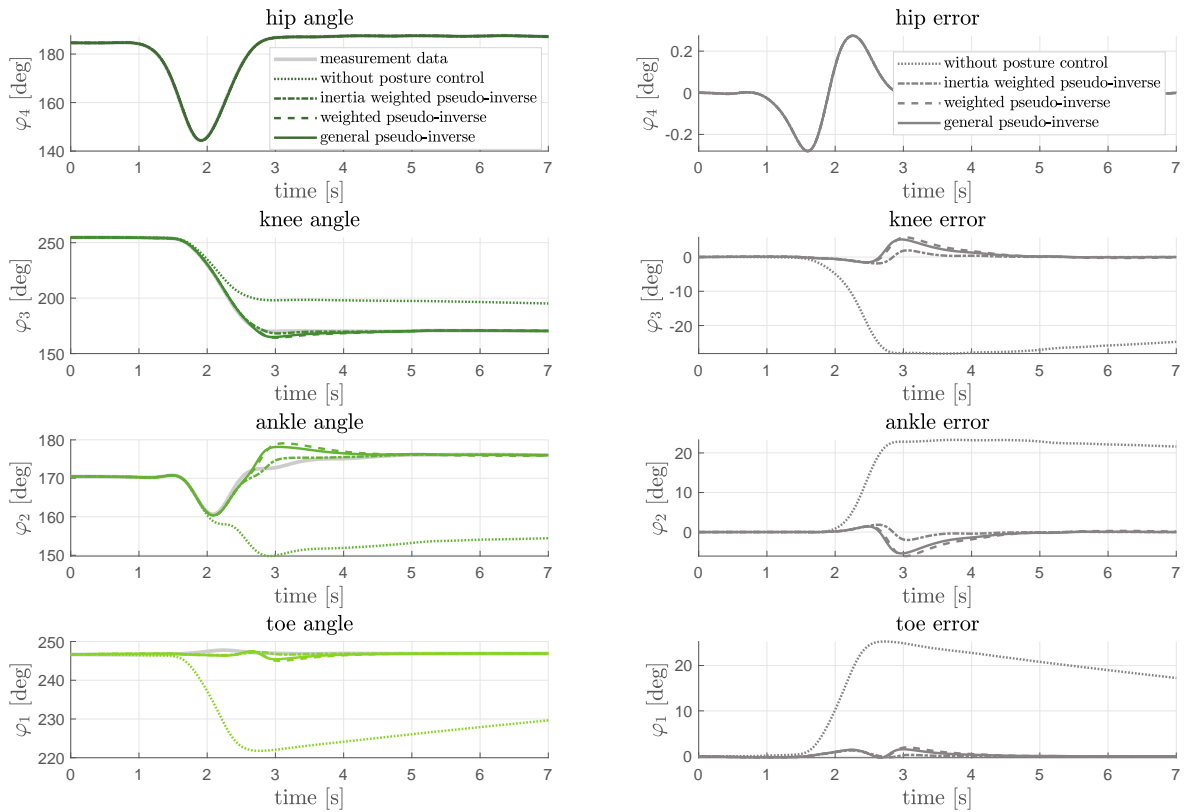


Figure 5.3: Joint angle trajectories in the context of employing various pseudo-inverses of the postural Jacobian matrix.

As can be seen, employing any posture control at all has a strong impact on manipulator free motion. No posture control leads to extreme deviations compared to human motion paths. The inertia weighted pseudo-inverse at posture level provides the best results in the sense of the lowest error w.r.t. the reference angular values. With this choice of postural control in mind, approach one is ultimately based on the input variables shown in fig. 5.4 and all following simulation results relate to it.

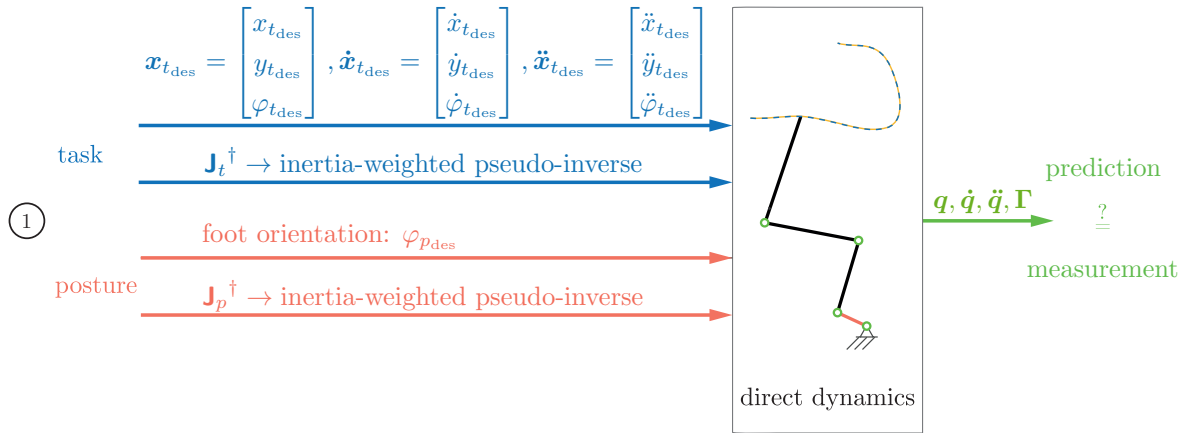


Figure 5.4: Approach one: Input data definition and desired outcome.

The joint angles and angular rates with corresponding errors between the direct and inverse dynamics values are illustrated in fig. 5.5 from left to right. From top to bottom, hip, knee, ankle and toe joint are outlined, respectively.

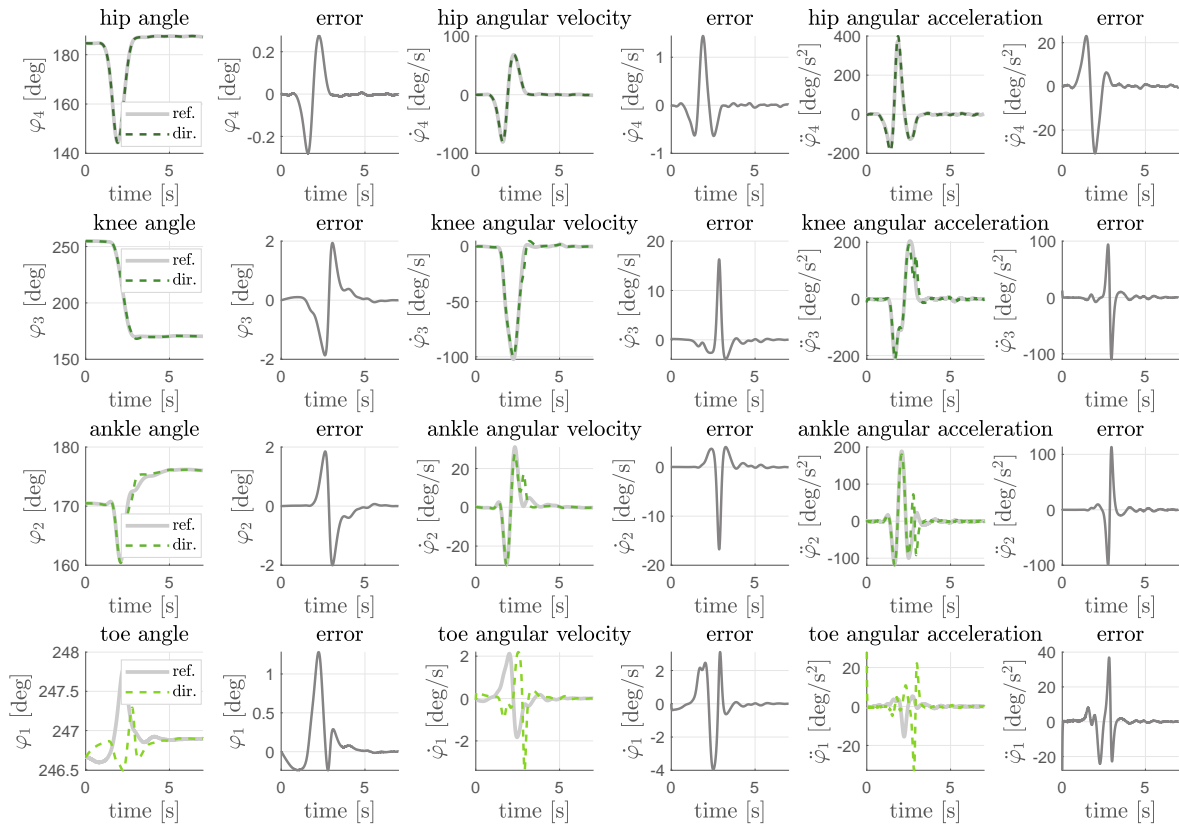


Figure 5.5: Time series of joint angles, angular velocities and angular accelerations of reference data (ref.) and direct dynamics computations (dir.) with corresponding errors.

As fig. 5.5 shows, a very accurate match of all trajectories with total angular errors of only 2 deg was achieved. Discrepancies in joint velocities lie at maximum 17 deg/s , whereas larger variances exist on acceleration level with 114 deg/s^2 .

The simulation results for the actual end-effector position, velocity and acceleration in x - and y -direction over time are shown in fig. 5.6. Respective errors present the deviations between desired and controlled end-effector trajectories.

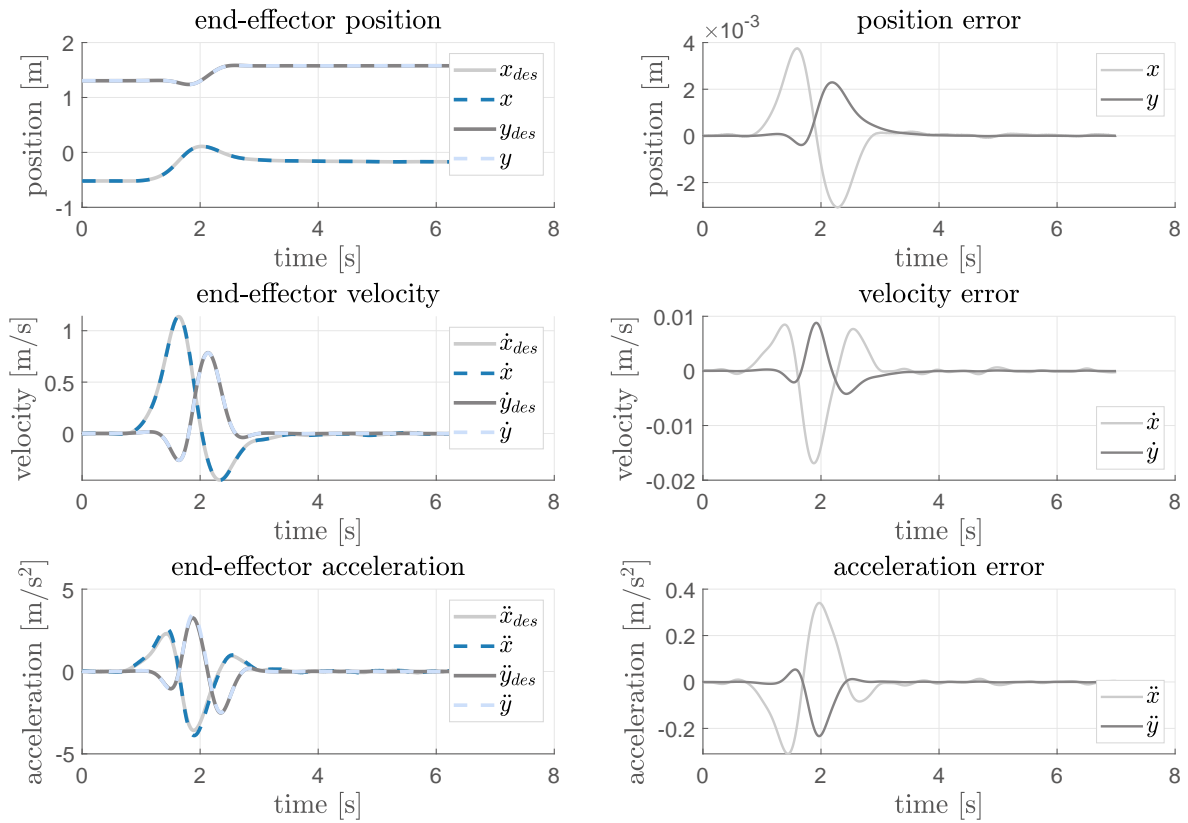


Figure 5.6: End-effector position, velocity, acceleration and corresponding errors w.r.t. actual and desired trajectories.

With a deviation factor of $10^{-3} m$ the end-effector follows the target trajectory very precisely with a maximum discrepancy of 4 mm . At velocity level, the end-effector tracks the target velocity accurately up to 16 mm/s . At acceleration level, the biggest error arises with 0.34 m/s^2 . It is worth mentioning that, since the end-effector is following desired trajectories on a control level, a small time delay in reaching a desired value is not surprising. A vertical error computation w.r.t. time therefore might seem big although the actual desired value was indeed attained milliseconds later.

Desired end-effector orientation $\varphi_{t_{des}}$ and actual orientation φ through simulation is

demonstrated in fig. 5.7. Again, end-effector orientation as well as angular velocity and acceleration are depicted on the left side, whereas according errors are shown on the right side. One can see that orientation errors are kept to a minimum with a range less than 0.3 deg . Angular velocity errors are less than 1.5 deg/s , angular acceleration errors less than 31 deg/s^2 .

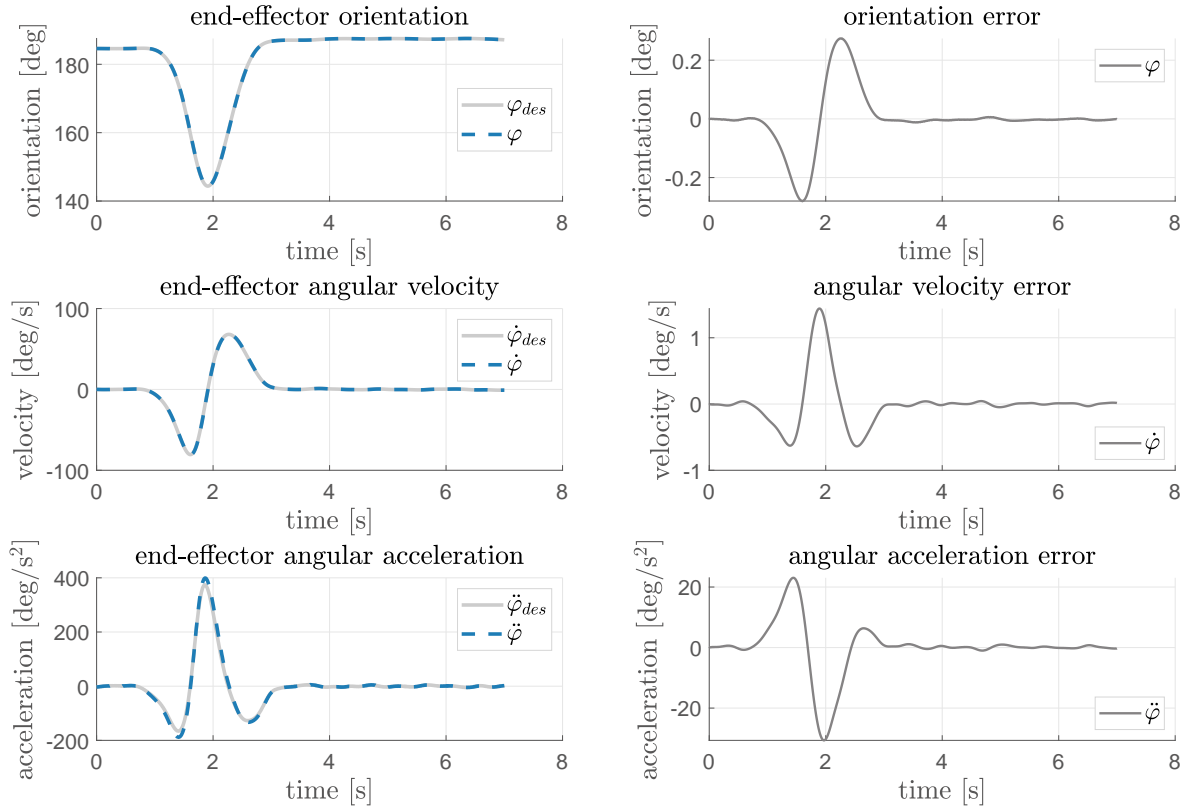


Figure 5.7: End-effector orientation, angular velocity, angular acceleration and corresponding errors w.r.t. actual and desired trajectories.

The joint torques of the biomechanical model with regard to hip extension, knee extension, ankle dorsiflexion and virtual toe joint variation w.r.t. time are outlined in fig. 5.8. The torques are shown for each individual joint of one side of the body. Within the inverse dynamics calculations, both the measured (orange lines) as well as the modeled (gray dashed lines) contact forces between chair and buttocks were implemented in order to show their differences within the application of a specific measurement. Direct dynamics simulation results are based on the modeled buttocks forces (purple dashed lines).

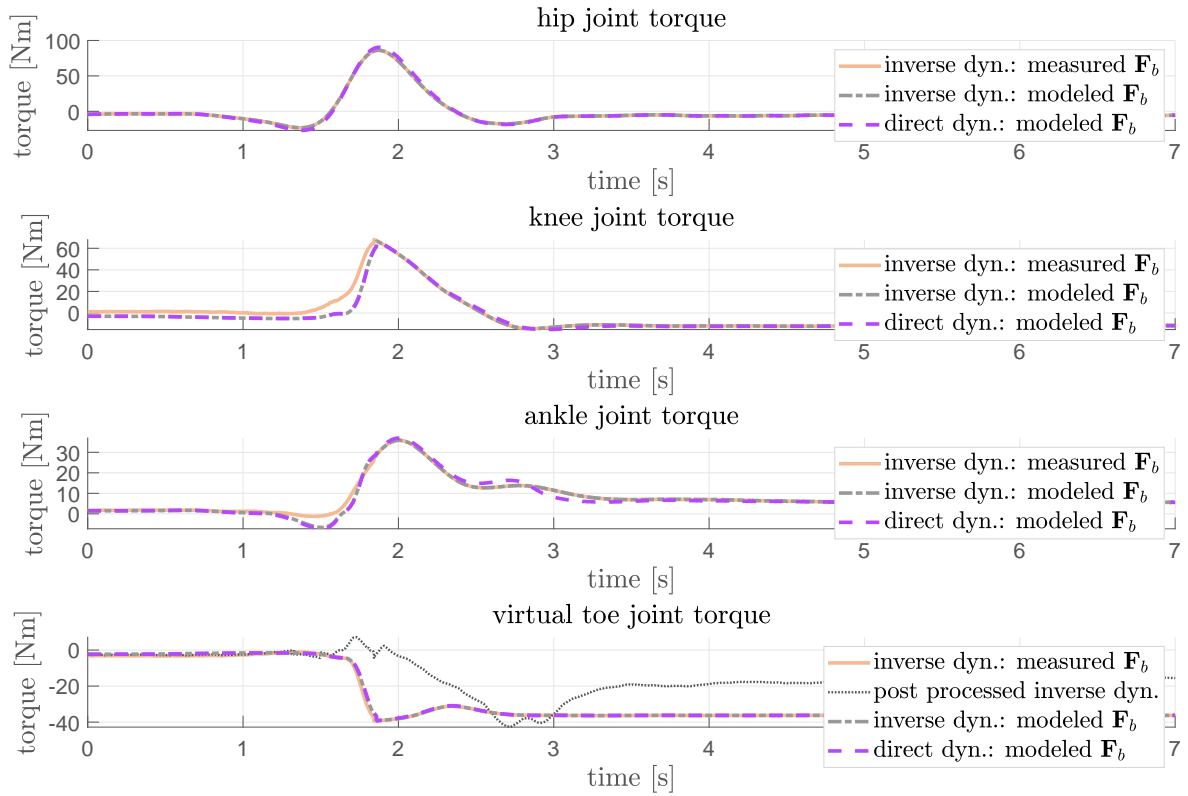


Figure 5.8: Joint torques regarding hip extension, knee extension, ankle dorsiflexion and virtual toe joint motion.

The virtual toe joint torque refers to the model based computed torque at the bottom joint of link l_1 and will be referred to as Γ_{virtual} (see fig. 5.9). Due to the moving point of force application (distance r) w.r.t. the measured ground reaction forces F_{mx} and F_{my} of the actual human STS motion in comparison to the modeled ground reaction forces F_x and F_y , the virtual toe joint torque Γ_{virtual} is not identical to the actually occurring joint torque Γ_{toe} .

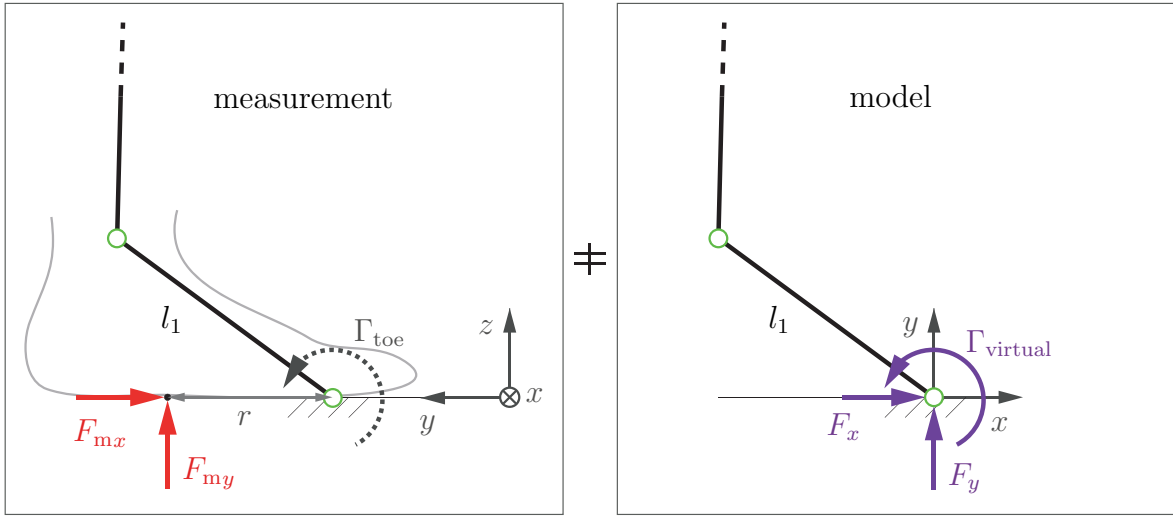


Figure 5.9: Discrepancy between measured and model based ground reaction forces.

In order to compute Γ_{toe} based on the simulation results Γ_{virtual} for the virtual toe joint, this variable is post processed within the inverse dynamics calculations and converted based on the measurement data:

$$\Gamma_{\text{toe}} = \Gamma_{\text{virtual}} + r \cdot F_{\text{my}}. \quad (5.4)$$

The post processed toe joint torque Γ_{toe} is portrayed in black dotted lines within the bottom plot of fig. 5.8 and represents the more realistic joint torque at the toe as a new reference. The simulation based toe joint torque, however, will always try to track Γ_{virtual} as a logical consequence to the model setup. This has to be kept in mind, but it is not further relevant to the simulation results regarding ankle, knee and hip joint torques.

On an inverse dynamics level, the joint torques resulting through employing the Gaussian function model for the buttocks contact forces (see chapter 3.2.4.2) are relatively close to those resulting through employing the measured contact forces. Since the Gaussian function model for the buttocks forces is based on mean values of five individual measurements, a small discrepancy between both inverse dynamics applications was to be expected for the utilization in one specific measurement. The error between both inverse dynamics torques can be seen as e_1 (orange lines) in fig. 5.10 for each the hip, the knee, the ankle and the virtual toe joint torque in time. The deviation of the simulated torques w.r.t. the inverse dynamics calculations based on the modeled buttocks forces are shown as e_2 (gray dot-dashed lines), and the one w.r.t. the inverse dynamics calculations based on the measured buttocks forces are depicted as e_3 (purple dashed lines).

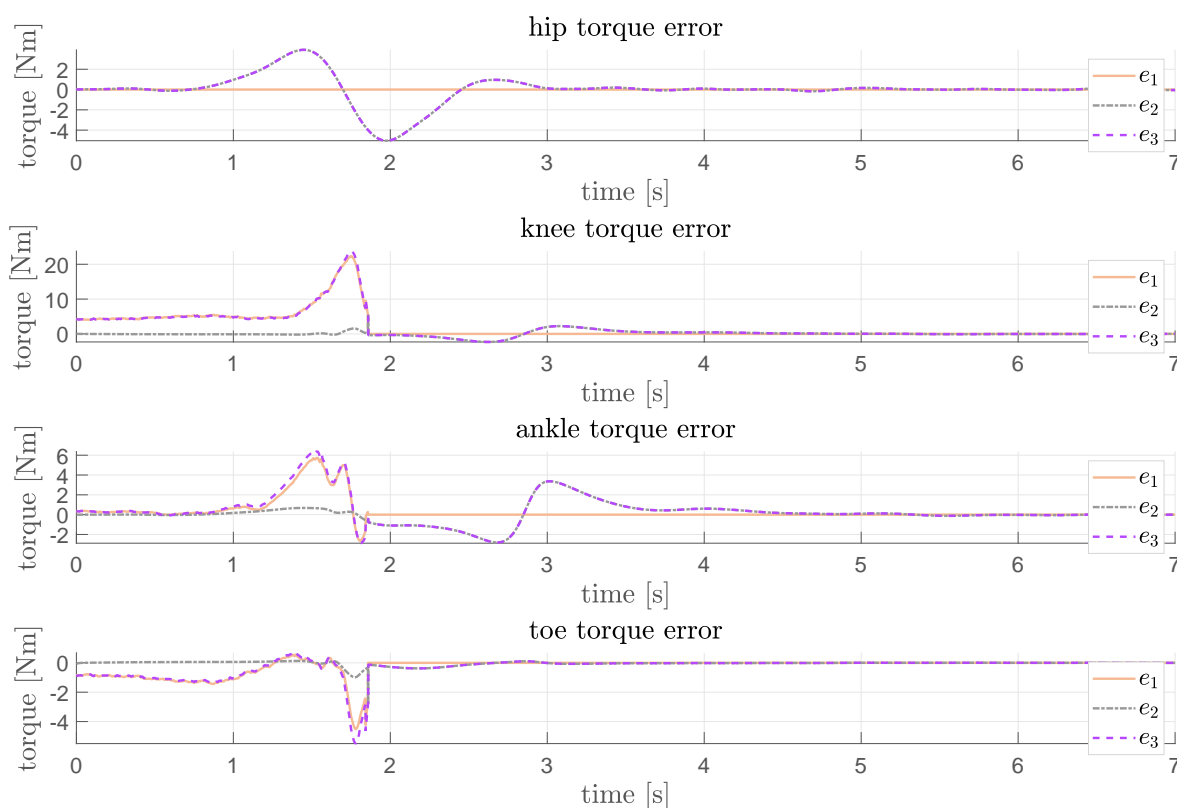


Figure 5.10: Joint torque errors: e_1 is the error between the inverse dynamics joint torques based on measured buttocks forces and based on modeled buttocks forces; e_2 is the error between the simulated torques and the torques resulting from inverse dynamics calculations with modeled buttocks forces; e_3 is the error between the simulated torques and the torques resulting from inverse dynamics calculations with measured buttocks forces.

The graphs in figures 5.8 and 5.10 show that the employment of the Gaussian function for the buttocks forces within the biomechanical model only matter for the knee torque up to a difference of $22 Nm$ w.r.t. the employment of the measured buttocks forces within the inverse dynamics model (cf. error e_1), of course only until the moment of seat-off, when the forces vanish anyway. For the ankle and virtual toe torque lower errors occur with $5.5 Nm$ and $4 Nm$, respectively, whereas for the hip torque no difference exists. Since the modeled buttocks forces are a part of the biomechanical model, the inverse dynamics calculations based on this model form the reference for comparing the simulation results to. As can be seen from error e_2 , non-conformance between simulated and calculated torques are kept to a minimum. The absolute maximum error occurs within the hip torque with $5 Nm$. As a result of deviations e_1 and e_2 , the variance between simulated torques and calculated torques based on the measured

buttocks forces (cf. error e_3) is naturally the largest.

As far as joint torque values are concerned, initial torques are almost zero due to the supporting chair contact forces in the sitting position. Joint torques then build up to peak torques with values for the hip of about $90 Nm$, for the knee of approximately $67 Nm$ and for the ankle of $37 Nm$. Joint torque values in stable stance are $-6 Nm$ regarding the hip, $-12 Nm$ for the knee and $6 Nm$ at the ankle.

Compared to Ozsoy and Yang [84], torque curves are similar with regard to their shapes. Peak torque values, however, are higher, since Ozsoy and Yang refer to $32.25 Nm$ for the hip extension, $46.63 Nm$ for the knee extension and $16.10 Nm$ for the ankle plantar flexion when converted to the model's anthropometry used in this thesis. The differences in torque peaks might result through differences in joint strength restriction, in model dimension setup and in the definition of the initial configuration: First of all, Ozsoy and Yang employ joint torque limit constraints and joint strengths that regulate the maximum occurring joint torque values. Although the chair without arm and back support and of the same height as used in this thesis seems to be equal, a three-dimensional model in constrained optimization simulations of unassisted STS for five male and five female healthy young virtual subjects with a mean mass of $66.6 kg$ and a mean height of $1.71 m$ is used, showing significantly bigger subject dimensions. Second of all, Ozoy and Yang's initial angle for the hip is $180.0 deg$, for the knee is $261.15 deg$ and for the ankle is $155.7 deg$, according to angle conversions w.r.t. the model definition of this thesis and as a mean value of right and left side. In this thesis, the initial configuration is defined as $184.6103 deg$ for the hip joint angle, $254.7995 deg$ for the knee and $170.4704 deg$ for the ankle. The qualitative curve progression of the presented simulation torque results are similar to those presented in Norman-Gerum [81] as well. Still, Norman-Gerum's peak values are lower with roughly $35 Nm$ for the hip, $65 Nm$ for the knee and $20 Nm$ for the ankle joint torque. These values refer to a healthy female subject of unknown anthropometric data represented as a three-link planar model with modeled buttocks forces through a one-dimensional Kelvin-Voigt element added to the HAT. Predictions are performed for STS transitions from an armless and backless chair of $0.46 m$ height. However, the presented peak joint torques lie within the limits of literature values for joint torque strengths reported in Schultz et al. [102]. Joint torque values for healthy young females per body side are reported to be $126 Nm$ for the hip extension, between $160 Nm$ and $183 Nm$ for the knee extension and between $44 Nm$ and $49 Nm$ for the ankle dorsiflexion. The simulated joint torques presented in this thesis are therefore notably smaller than the minimal available joint torques.

Toe joint torques are not comparable to literature since most authors use biomechanical models that do not regard the toe joint in particular.

Discussion

Applying the operational space control method presented in chapter 4.4 with all possible command variables for the end-effector in the sagittal plane provides a good means of predicting STS motion in real-time. Not only the task itself, i.e. the attainment of the end-effector trajectory, but also human posture during the STS motion is accurately achieved through posture control regarding the foot orientation. Merely 42 seconds of computation time was needed for the forward dynamics computation on a processor Intel(R) Core(TM) i7-6700K CPU @ 4.00GHz with MATLAB routine settings as described in section 4.5.3, and 46 seconds for the complete inverse and direct dynamics calculations. The simulation is shown as a series of snapshots in fig. 5.11.

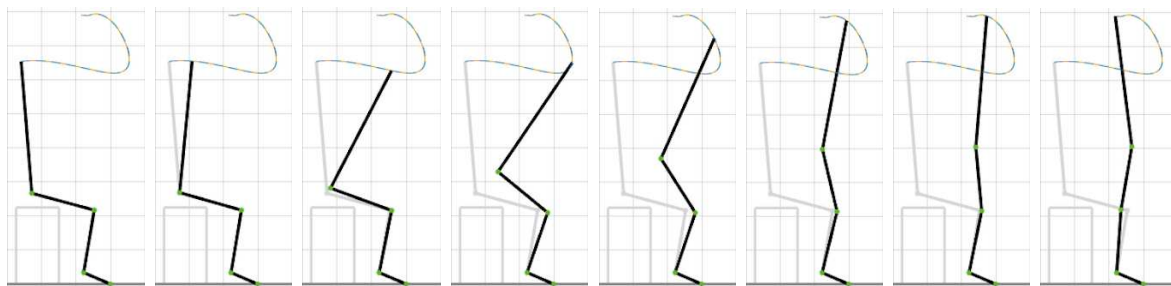


Figure 5.11: Simulation sequence of STS motion using a full set of command variables within the operational space control framework.

Hip, knee and ankle variables are in good agreement with measured joint angles. This already provides a meaningful comparison which is why a comparison of joint angle trajectories to the literature was omitted.

Conformance between simulated and calculated joint torques is very high as well. Qualitative curve progressions comply with literature torque curves for STS motions. The occurring differences in peak torque values compared to values reported in the literature can have several reasons: experimental studies show that each factor such as foot location during seat-off, chair height, muscle strength, speed, age etc. has an impact on the joint coordination strategy of a STS transition [84]. A comparison to simulation results of other authors, therefore, is only reasonable for similar STS task and model conditions. However, according to literature [81, 84, 102] knee extension torques are usually the largest, whereas in this thesis the hip torque is larger than the knee torque. This discrepancy with regard to the literature remains an open question at this point,

since simulation values are in accordance with measurement data.

A major contribution of this work constitutes the realistic reproduction of the foot rocking that could be observed in the STS experiments (cf. toe angle curve in fig. 5.5). Through implementing both feet as one rigid link with an additional revolute joint at the toe, the four-link model simulates the small movements of the feet of less than 2 deg . The quadruple pendulum model in combination with the proposed control method has therefore proven to be a simple but useful reflection of reality.

It is worth mentioning that simulations were run for the same model with a fixed ankle to emulate a triple pendulum, that naturally becomes a non-redundant system where the aforementioned posture control did not have to be applied. While the end-effector was urged to follow the same head-trajectory as before under the same system conditions and software settings with identical gain matrices and tolerances, the model configuration during the STS motion did not comply well with reference data. This can be seen in the simulation results of the triple pendulum shown in appendix F. Ankle and knee joint angles deviate up to 8 deg w.r.t. reference angles. This reflects on the corresponding joint torques, where errors between the direct and inverse dynamics calculations based on the modeled buttocks contact forces arise. For the knee joint torque maximum deviations of 9 Nm occur, whereas for the ankle joint torque 10.5 Nm of discrepancies can be observed (errors e_2 in fig. 10). End-effector position and orientation, however, match the desired trajectories in the same manner as before, although a slightly less accurate curve tracking on position level can be seen in comparison to the simulation results for the quadruple pendulum. All in all, the four-link model provides more accurate and thus more realistic results than the three-link model, in that small movements of the feet help to compensate for the errors in the joint angles. This is simply achieved through the postural control.

5.2 Approach two: command variables $y_{t_{\text{des}}}$ and $\varphi_{t_{\text{des}}}$

In order to control end-effector motion behavior through a reduced set of command variables in terms of $y_{t_{\text{des}}}$ and $\varphi_{t_{\text{des}}}$ as well as their velocities and accelerations, only four control parameters for the task as well as two control parameters for the posture are needed. The parameter settings chosen for this kind of STS motion prediction are shown in tab. 5.2.

Parameter	Value
k_2	30.0
k_3	50.0
ξ_2	15.0
ξ_3	20.0
k_{posture}	150.0
ξ_{posture}	140.0

Table 5.2: Parameter settings for a reduced set of command variables.

Hereinafter simulation results are presented. Plots follow the same pattern of design and order as in section 5.1 and are not described in detail again.

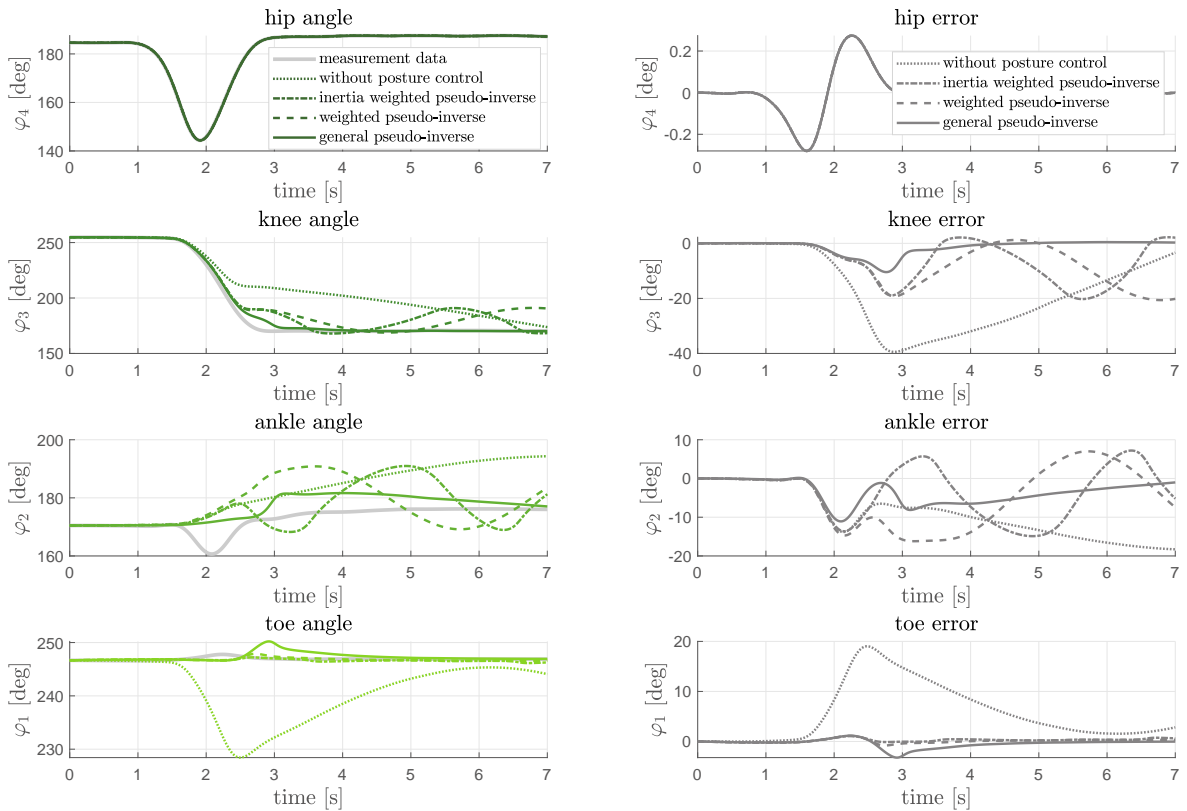


Figure 5.12: Joint angle trajectories in the context of employing various pseudo-inverses of the postural Jacobian matrix with regard to a reduced set of command variables.

Employing a general pseudo-inverse $\mathbf{J}_p^\dagger = [1.0 \quad -0.3 \quad 0.1 \quad 0.0]^T$ yields the best results in comparison to the kinetic-energy pseudo-inverse and the weighted pseudo-inverse. Simulations were therefore performed using this general pseudo-inverse within

the postural control framework (cf. fig. 5.13). The results are illustrated in figures 5.14 to 5.19.

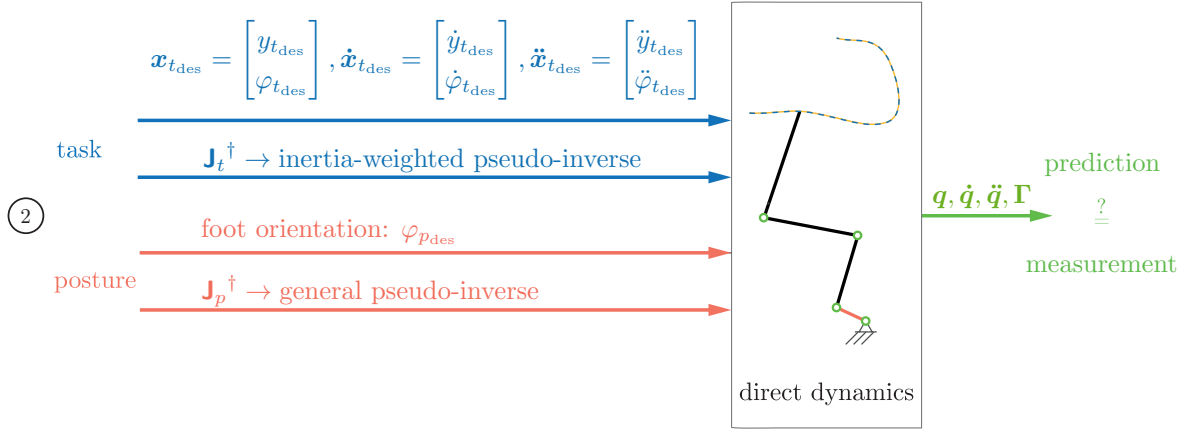


Figure 5.13: Approach two: Input data definition and desired outcome.

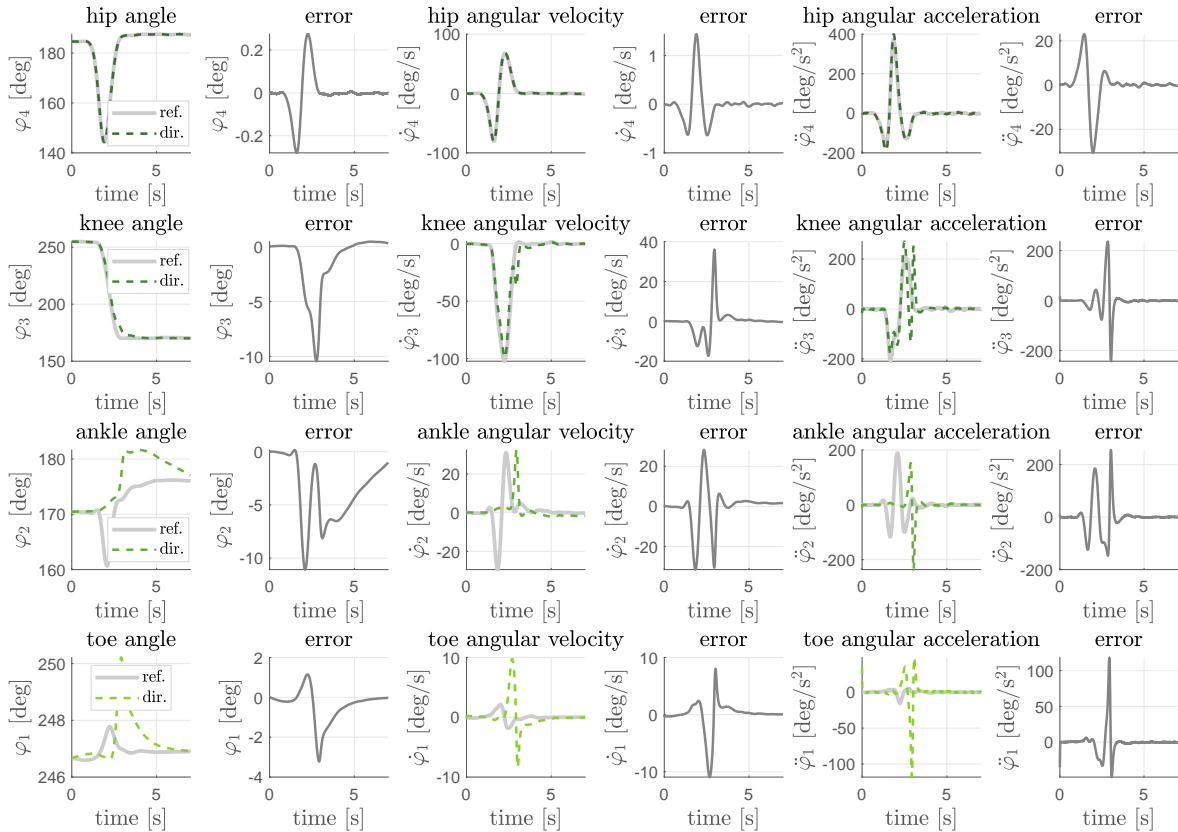


Figure 5.14: Time series of joint angles, angular velocities and angular accelerations of reference data (ref.) and direct dynamics computations (dir.) with corresponding errors for a reduced set of command variables.

Curve conformity of hip and knee angles as well as angular rates can be observed in fig. 5.14. Approximately after seat-off, when the knee starts moving, the progression of the angle of the ankle does not yield good results. The simulation fails in even getting close to the measured joint angle peak and then overshoots the goal trajectory. As a consequence, the toe angle overshoots its goal trajectory as well, the qualitative curve progression, however, is similar to the desired one. Corresponding angular velocities and accelerations of ankle and toe overstep measured trajectories as a result of more rapid angular changes than it is the case in reality.

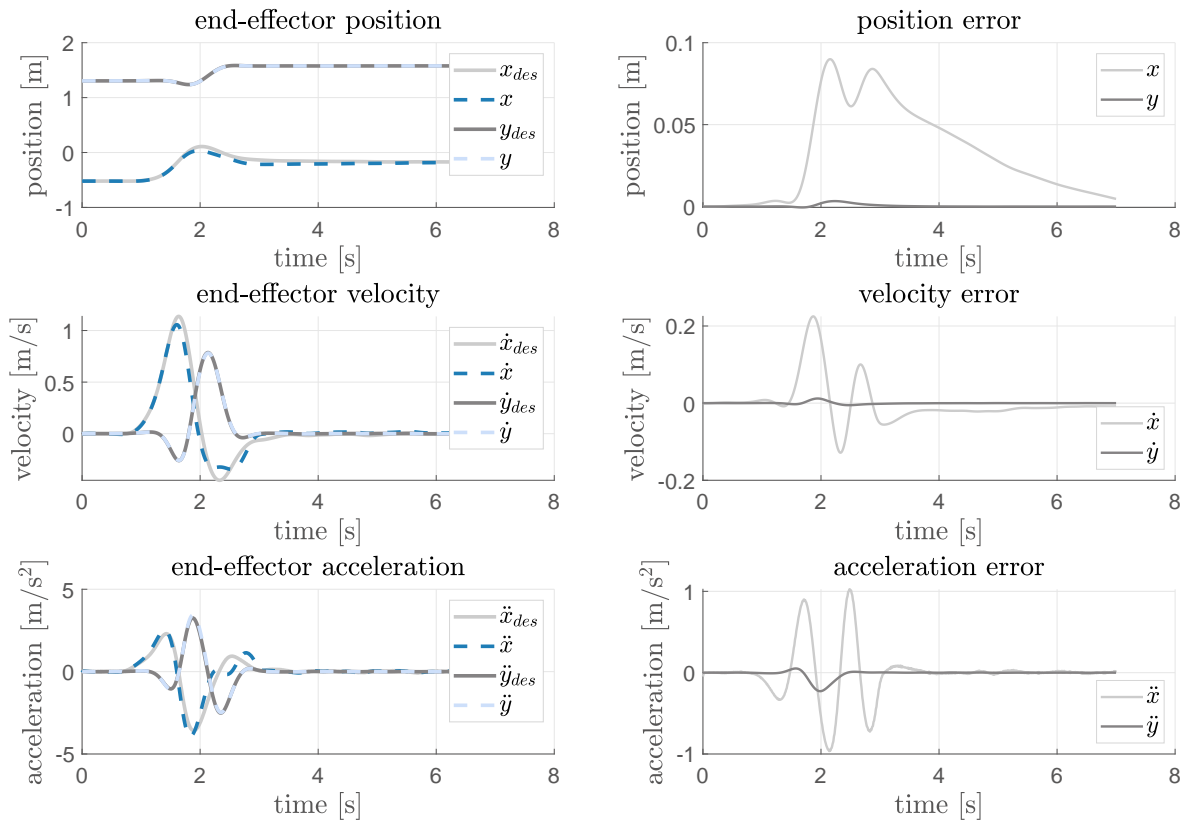


Figure 5.15: End-effector position, velocity, acceleration and corresponding errors w.r.t. actual and desired trajectories in the context of a reduced set of command variables.

Since $y_{t_{des}}$ is given as input, the simulated end-effector position, velocity and acceleration in y -direction is accurately conform to the desired trajectory with only marginal errors (cf. fig. 5.15). Desired end-effector x -position is tracked surprisingly well with less than 9 cm of horizontal shift w.r.t. the simulated end-effector trajectory. Bigger errors occur in x -direction with velocity and acceleration values of 0.21 m/s and 1 m/s², respectively.

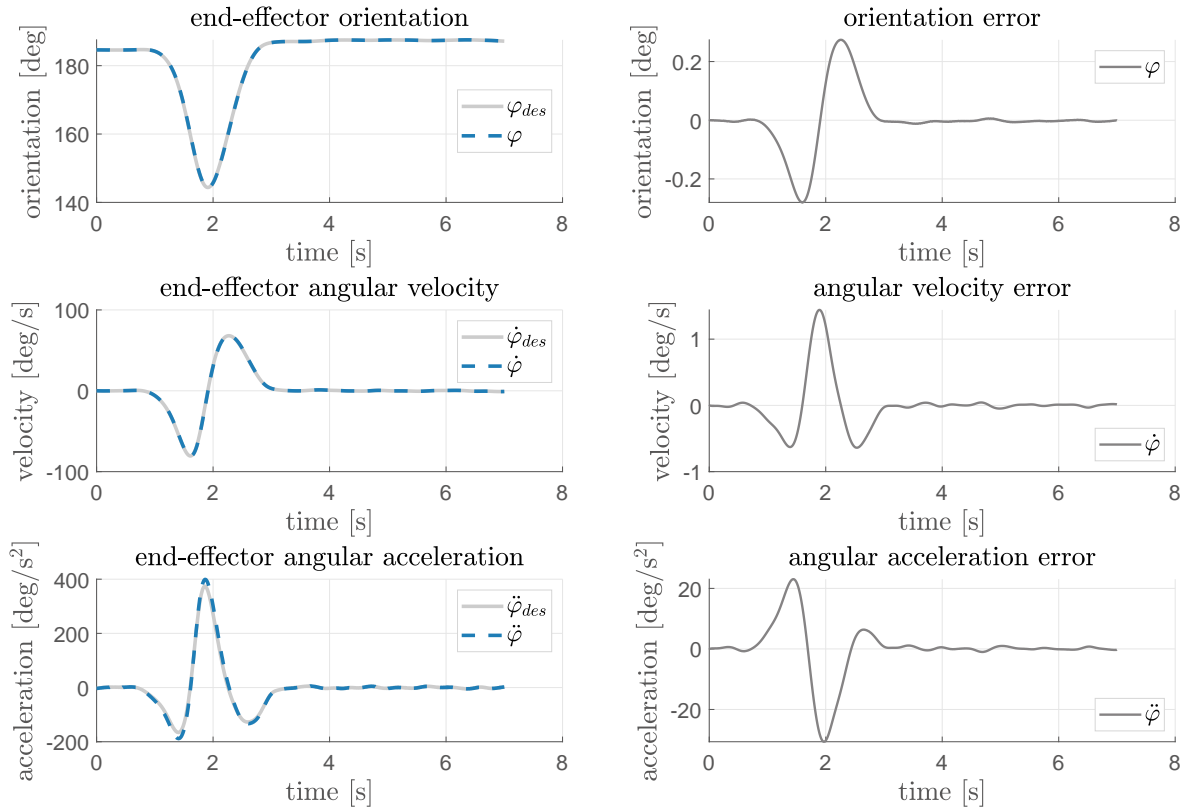


Figure 5.16: End-effector orientation, angular velocity, angular acceleration and corresponding errors w.r.t. actual and desired trajectories in the context of a reduced set of command variables.

Compared to the simulation results of employing a full set of command variables, same end-effector orientation errors occur which are kept to a minimum (see fig. 5.16). This was to be expected, since $\varphi_{t_{des}}$, again, is given as an input to the control method with the same values for the corresponding gain factors k_3 and ξ_3 .

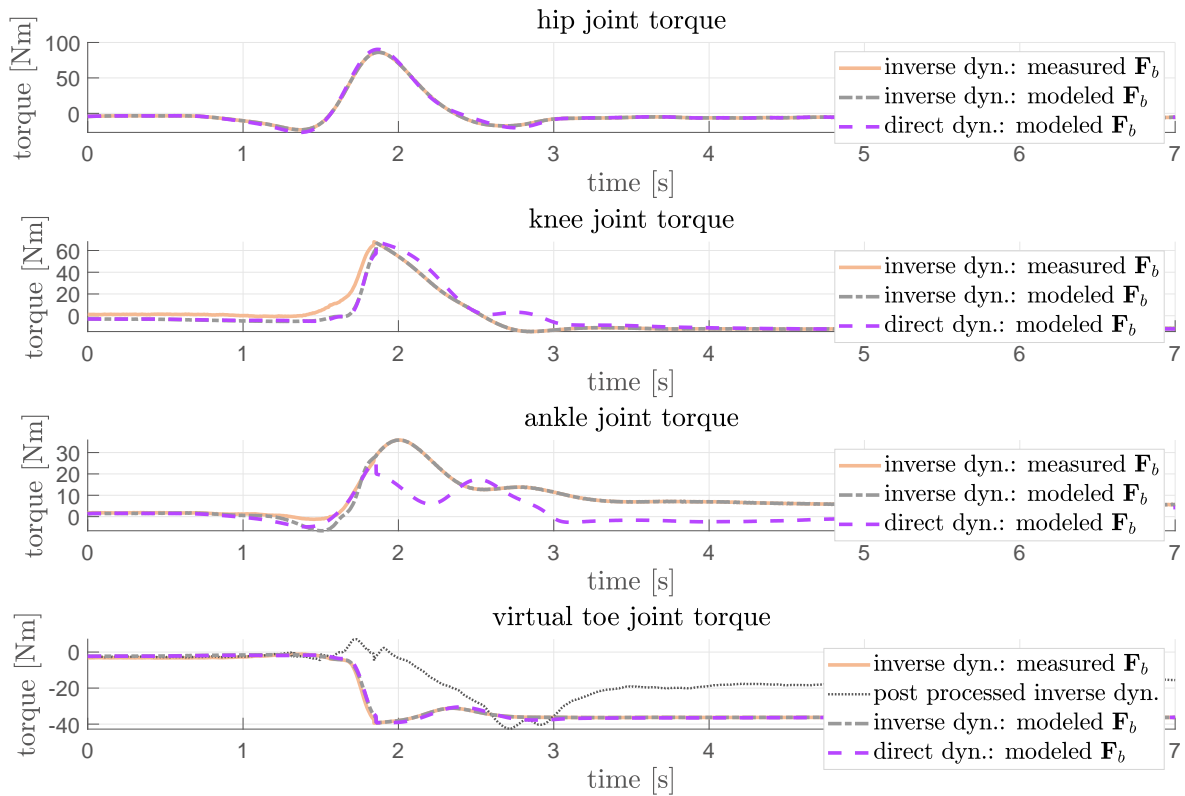


Figure 5.17: Joint torques regarding hip extension, knee extension, ankle dorsiflexion and virtual toe joint motion in the context of a reduced set of command variables.

In fig. 5.17 it is shown that joint torques regarding hip and virtual toe match their corresponding computed torques pretty precisely. Deviations exist for the knee joint torque, though larger deviations occur in the curve shape of the ankle joint torque. This correlates with the errors in angle, velocity and acceleration of the ankle joint seen in fig. 5.14. In stable stand, hip, knee and virtual toe joint torque all comply with their computed values very fast. Only the ankle joint torque slowly reaches the requested value.

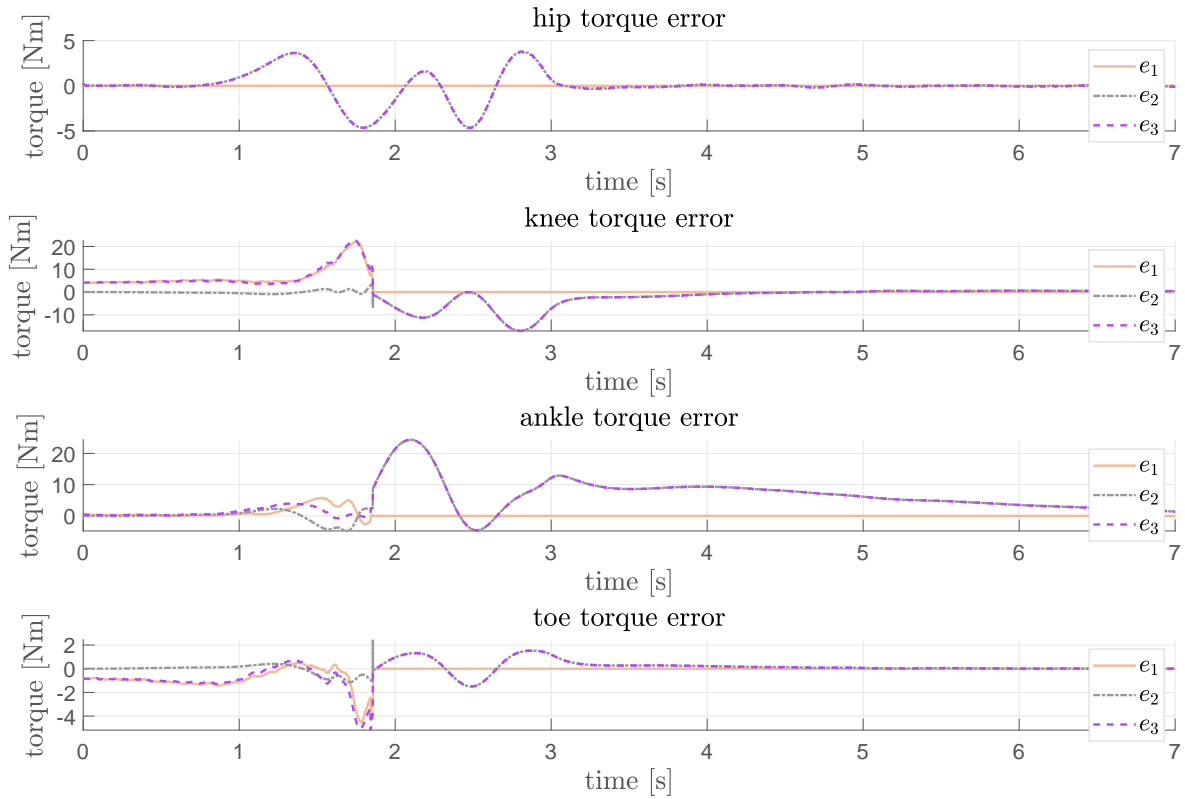


Figure 5.18: Joint torque errors in the context of command variables $y_{t_{des}}$ and $\varphi_{t_{des}}$: e_1 is the error between the inverse dynamics joint torques based on measured buttocks forces and based on modeled buttocks forces; e_2 is the error between the simulated torques and the torques resulting from inverse dynamics calculations with modeled buttocks forces; e_3 is the error between the simulated torques and the torques resulting from inverse dynamics calculations with measured buttocks forces.

Joint torque errors presented in fig. 5.18 validate aforementioned statements. Error e_1 between the inverse dynamics joint torques based on measured and modeled buttocks forces do not change, since the same measurement data were involved as reference. Errors between simulated and computed torques based on the buttock model implementation (e_2) are the highest for the ankle with torque deviations up to $24 Nm$ followed by knee joint errors of $17 Nm$. Hip torque errors, as before, stay within a range of $5 Nm$. Also virtual toe errors are similar with a peak height of $2.4 Nm$.

Discussion

STS motion prediction using operational space control with $y_{t_{des}}$ and $\varphi_{t_{des}}$ as the reduced set of command variables yields results that fulfill task completion to the extend that end-effector orientation and y -position is accurately met, but errors in x -direction

occur. Fig. 5.19 shows the task trajectory in blue dashed lines, while the desired trajectory is illustrated in yellow. Along with the smaller amplitude in x -direction compared to the desired end-effector trajectory, the ankle appears to be stiff and then deflects in opposite direction compared to experimental results. The stiff upwards movement does not precisely match the healthy human STS motion that is used as reference from measurement data, but still gives a good approximation. The torques match the computed values pretty closely, only the ankle torque is too small compared to the computed values. Furthermore, the computation time is even smaller than before with only 33 seconds for the forward dynamics and 36 seconds for complete inverse and direct dynamics evaluations on the same processor and for the same program settings as before.

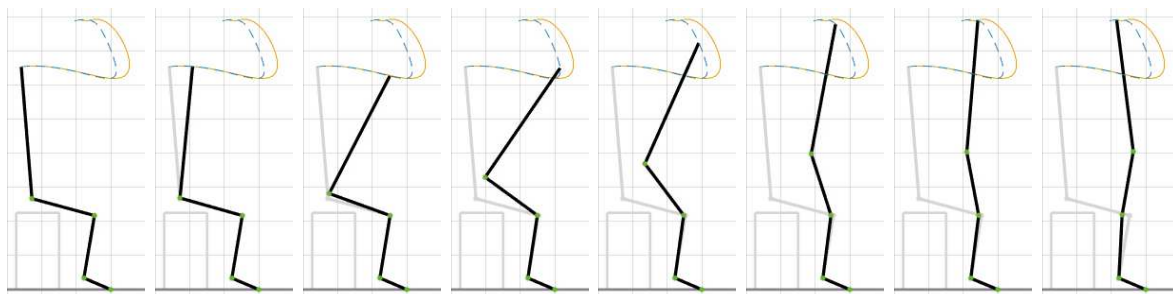


Figure 5.19: Simulation sequence of STS motion using a reduced set of command variables within the operational space control framework.

Even though it is not clear at this point how the general pseudo-inverse of the Jacobian matrix can be interpreted biomechanically, employing the general pseudo-inverse does lead to the best results compared to the application of the inertia weighted pseudo-inverse within the posture control.

6 Comparison to an optimization-based motion generation method

For validation purposes an optimization-based motion generation method (cf. chapter 1.1) was implemented in `Matlab`, since it represents the most common approach used nowadays in STS prediction. The dynamic optimization method based on the PhD thesis from Valerie Theresa Norman-Gerum [81] with supervisor Prof. Dr. John McPhee and external examiner Prof. Dr. Katja Mombaur was chosen for comparison, as this method comprises one of the latest works from 2019 in the same field of research with the inclusion of a buttocks model.

6.1 Optimization-based reference method

The iterative dynamic optimization method by Norman-Gerum [81] comprises a purely predictive simulation of STS motion that requires minimal effort according to the fundamental belief that natural, practiced motions are optimal in a sense that healthy people prioritize mechanical efficiency. A planar three-link model, the so far most comprehensive model in predicting STS, with arms crossed in front of the chest (cf. fig. 6.1) is employed. Body segment dimensions and anthropometry describe a healthy female based on general literature data without further information on the specifics. A foot segment is added to the ankle joint and a buttocks model is added to the upper body. The chair is assumed to be backless, armless, of steel construction and of adjustable height.

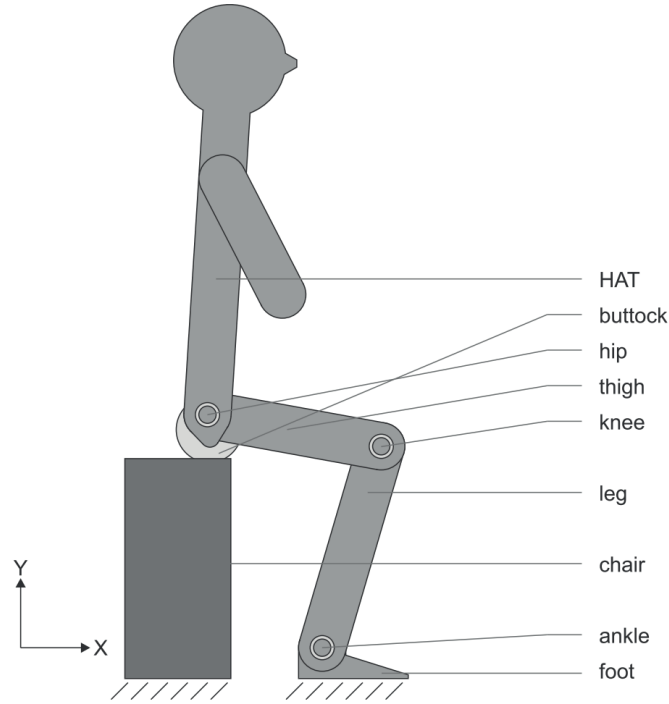


Figure 6.1: Schematic of the three-link sagittal plane model used by Norman-Gerum [81].

The optimal control framework is composed of a parameter optimization problem where the location of the hip joint center in X - and Y -direction relative to the ankle position as well as the angle of inclination of the HAT represent the control parameters. Three composite Bézier curves model the locations of the controls in time. These are smooth parametric curves described by points of the form

$$\mathbf{p}(u) = \sum_{i=0}^n \mathbf{p}_i \binom{n}{i} u^i (1-u)^{n-i} \quad u \in [0, 1], \quad (6.1)$$

where $n + 1$ is the number of two-dimensional control points \mathbf{p}_i of value and time, $\binom{n}{i}$ are the binomial coefficients and u is a parametric coordinate analogous to a percentage of motion. To transfer from u to time, u is multiplied by the final time. Fig. 6.2 shows the initial Bézier curves regarding the HAT inclination, the hip height and the relative anterior-posterior (AP) position of the hip. For still sitting, two control points (*) of the same value taken from literature parameterize the first half second of the desired motion. The motion itself is initially parameterized by two control points of sitting values and two control points of standing values each (o) and spans 4 seconds in time. The final part is composed by two control points of the standing component (+) for 0.5 seconds with coordinate values taken from literature.

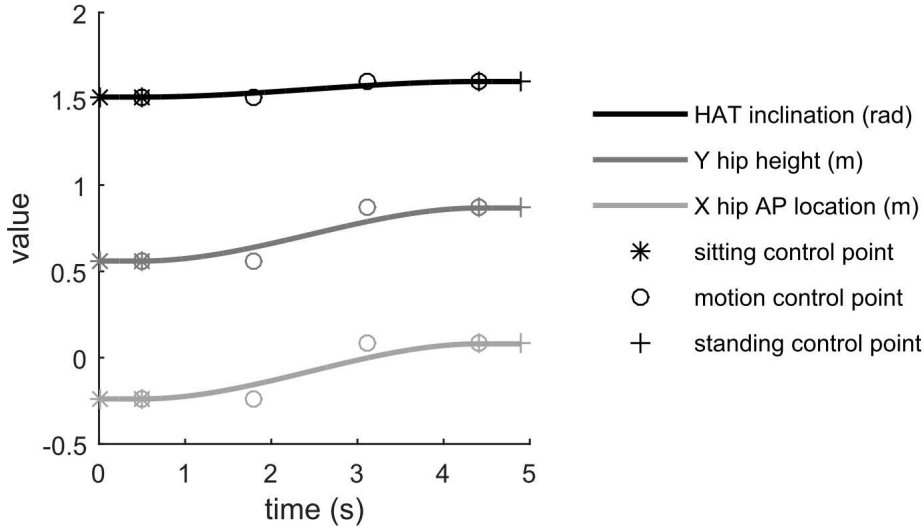


Figure 6.2: Initial Beziér curves used by Norman-Gerum [81] to describe the sitting, motion and standing components of STS motion.

In an initial optimization step possible STS motions are evaluated in order to determine a feasible STS starting point. By minimizing a weighted cost function

$$cost_{error} = w_h \int_0^5 error_h^2 dt + w_t \int_0^5 error_t^2 dt + w_l \int_0^5 error_l^2 dt + w_s \int_0^5 error_s^2 dt \quad (6.2)$$

that considers an error for impossible configurations of hip locations outside of the workspace $error_h$ as well as errors considering the static equilibrium of the foot for tipping $error_t$, lifting $error_l$ and slipping $error_s$, the position of the foot is predetermined and fixed to the ground (for detailed error definitions please refer to Norman-Gerum [81]). Weighting factors were chosen to be $w_h = 1 N^2$, $w_t = 10^3 N^2$, $w_l = 1 m^2$, $w_s = 1 m^2$. Certain control point locations of the Beziér curves are adjusted by `fmincon`, namely the two intermediate control points of each motion path that can change in time as well as the sitting hip height and the standing hip AP position that can change in value. The solution with zero associated error is then given to the solver in the iterative dynamic optimization routine.

Within the iterative dynamic optimization the objective function of eq. (6.2) and a cost function that considers the sum of the required joint torques squared

$$cost_{torque} = \int_0^5 A_M^2 dt + \int_0^5 K_M^2 dt + \int_0^5 H_M^2 dt \quad (6.3)$$

are minimized with A_M , K_M and H_M being the net ankle, knee and hip joint moments determined through inverse dynamics, respectively. Through the overall cost function

$$cost = cost_{error} + cost_{torque} \quad (6.4)$$

mechanical effort and motions contrary to standing like slipping or falling are minimized in order to account for minimal exertion of healthy everyday motion and feasibility of motion. In order to decrease the overall cost of eq. (6.4), control point locations are modified by `fmincon`. Control points are only bound in time sequence

$$\mathbf{p}_{i,time} = \mathbf{p}_{i-1,time} \quad i = 1, \dots, n + 1 \quad (6.5)$$

and hip height is bound to guarantee contact with the chair while sitting. The routine ends with optimal control points that minimize cost with zero associated error and iteratively starts over after elevating the degree of each path by an additional control point that is free to move in time and value. Through the process of degree elevation the degree of a Bézier curve is increased without changing its shape, that is, the previous and new set of control points $\mathbf{p}(u)$ and $\mathbf{p}'(u)$

$$\mathbf{p}'(u) = \mathbf{p}(u) \quad (6.6)$$

generate the same curve through

$$\sum_{i=0}^{n+1} \mathbf{p}'_i \binom{n+1}{i} u^i (1-u)^{n+1-i} = \sum_{i=0}^n \mathbf{p}_i \binom{n}{i} u^i (1-u)^{n-i}. \quad (6.7)$$

The iteration ends when solutions converge.

Optimization results taken from Norman-Gerum [81] are shown in fig. 6.3 for a 46 cm chair and an improved buttocks model. Higher order Bézier curves show the final paths of hip location and HAT inclination in solid lines with the beginning and ending of STS motion marked in dashed-dotted lines. (Dashed lines as well as vertical dotted lines represent results for an initial buttocks model that is of no further interest).

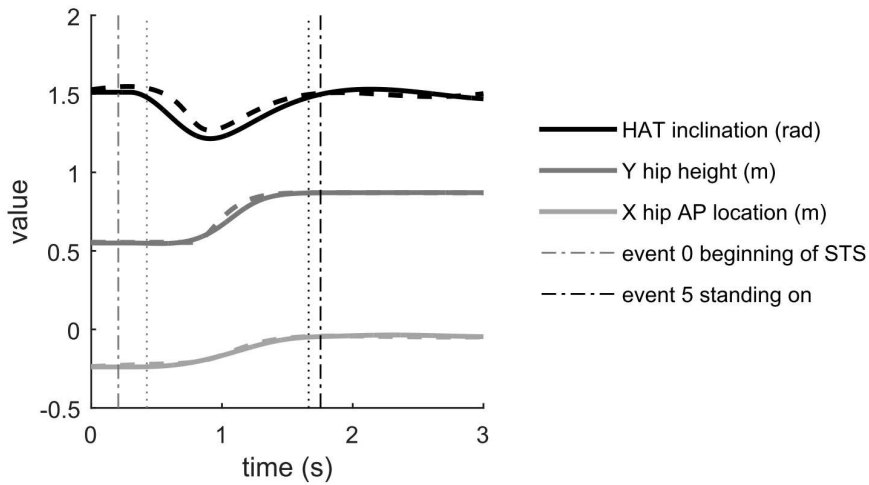


Figure 6.3: Optimized Bézier curves (solid lines) in Norman-Gerum [81].

Joint torques resulting from this optimization are illustrated in fig. 6.4. Again, only the solid lines are of interest, as they show the final results based on the implementation of Norman-Gerum’s Kelvin-Voigt buttocks model. She compares the joint torque values to joint torque strengths reported in Schultz et al. [102], marked as horizontal limit lines.

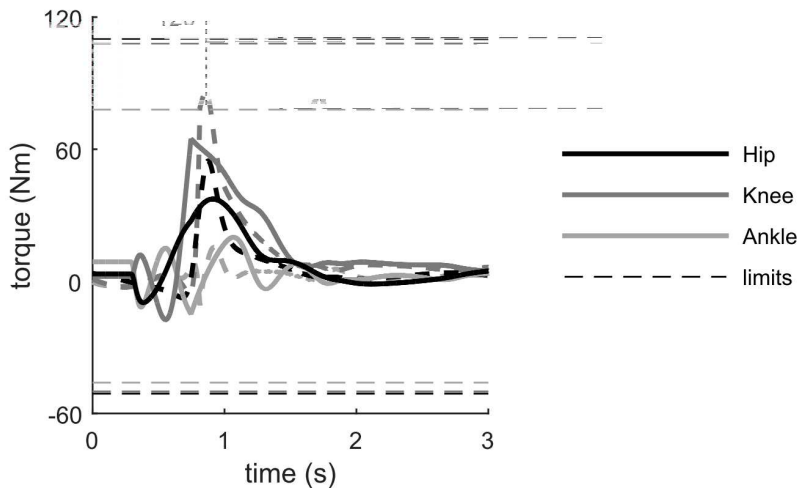


Figure 6.4: Joint torques reported by Norman-Gerum [81] for optimal STS from a 46 *cm* chair compared to joint torque strengths (horizontal lines) reported in Schultz et al [102].

In her thesis, the results are compared to normative data from the literature. It turns out that the prediction shortens the duration of STS. Possible reasons are the

human tendency of caution which is not displayed in the model, or missing checks if the muscles are physically able to produce joint torques in that amount of time, since no activation and deactivation times were given in the simulation. In addition, it does not accurately predict the standing posture, since the ankle is less flexed and the upper body is more tilted than expected. Norman-Gerum concludes that people favor more than just minimal effort during standing, such as spatial awareness. However, statically stable standing is still described. Other than that Norman-Gerum claims to predict STS motion physically plausible for healthy young adults and in general good agreement with literature data. Also, for the first time, Bézier curves are used in dynamic optimization of STS.

6.2 Implementation for quadruple pendulum model

The optimization method described in section 6.1 was implemented for the planar four-link model described in chapter 3 in order to ensure comparability to the operational space control method presented in chapters 4.4 and 4.5. However, the foot was fixed to the ground as described below so that the pendulum equals a triple pendulum such as in Norman-Gerum's model. Prediction results were compared to measurement data according to the measurement used in chapter 5.

Therefore, initial and final values for the hip X - and Y -position as well as the HAT inclination were taken from the measurement data and freedom to the values of the control points regarding the hip height while sitting and the hip AP position while standing was not given. Due to differences in the model itself, alterations regarding the fixed foot implications had to be executed. Since the foot is represented as a rigid link that is fixed to the ground at the toe joint, the ankle height a was passed as an additional control variable and the cost function eq. (6.2) regarding the foot position was reduced to

$$cost_{error} = w_h \int_0^5 error_h^2 dt + w_l \int_0^5 error_l^2 dt \quad (6.8)$$

with weighting factors that were left to the original values. The error functions were altered to be:

$$error_h = \begin{cases} \sqrt{X^2 + Y^2} - (l_1^2 + l_2^2 + l_3^2) & \sqrt{X^2 + Y^2} > l_1^2 + l_2^2 + l_3^2 \\ 0 & \text{otherwise} \end{cases} \quad (6.9)$$

$$error_l = \begin{cases} |a - a_0| & a \neq a_0 \\ 0 & \text{otherwise,} \end{cases} \quad (6.10)$$

where a_0 is the initial ankle height that was based on measurement data. However, the initial optimization step becomes redundant, since it is equal to passing the constant initial ankle height a_0 to the iterative dynamic optimizer in order for the foot to be fixed to the ground.

In the light of comparability to the method presented in this thesis and to the reference data, time intervals of sitting, motion and standing paths were tailored to measurement data. For the iterative optimization process, a small modification concerning the bound of the Y -position of the hip was necessary in order to avoid unrealistic motion. Although Norman-Gerum suggests that bounds in values are unnecessary when optimizing, an upper bound of the hip height to the final Y -position proved necessary.

Simulation results are shown in the following figures. In fig. 6.5 the Bézier curves of the upper body angle, the hip Y - as well as the hip X -position are depicted. Dashed lines illustrate the reference data based on the measurement. Dot-dashed lines show the corresponding initial Bézier curves with the initial control points of sitting, motion and standing paths. The optimized curves, represented in solid lines, are the result of the iterative dynamic optimization, minimizing the sum of $cost_{error}$ (eq. (6.8)) and $cost_{torques}$ (eq. (6.3)). The options for `fmincon` were set to be `OptimalityTolerance = 1.0e - 5`, `StepTolerance = 1.0e - 4` and `MaxFunctionEvaluations = 4000`.

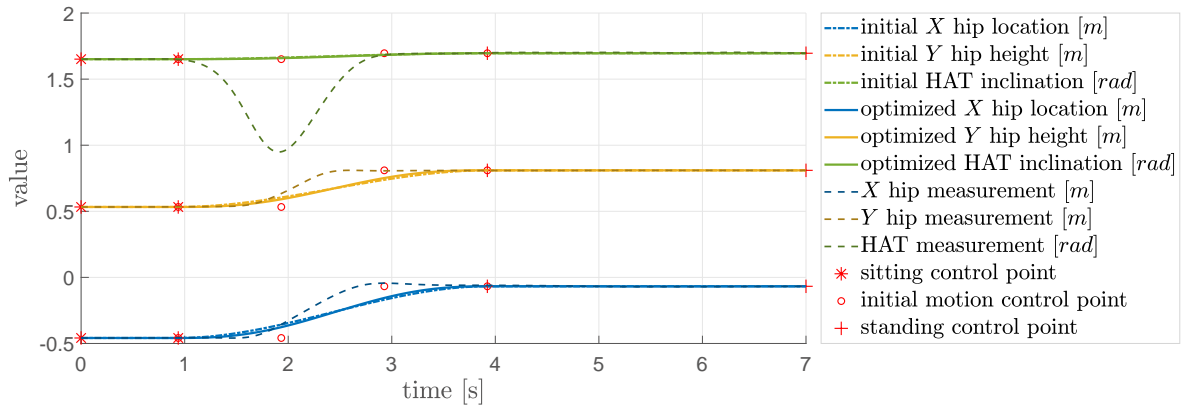


Figure 6.5: Three Bézier curves describing the initial (dot-dashed lines), final (solid lines) and reference (dashed lines) STS motion paths with sitting, motion and standing component.

The results do not show major improvements regarding an approximation to reference data. However, the optimization process was running through 32 iterations of the dynamic optimization resulting in 32 new control points through degree elevation. Every iteration step ended prematurely, as the size of the current step during the

function evaluation was less than the value of the step size tolerance and constraints were satisfied to within the value of the constraint tolerance. In addition, the cost only showed a small decrease from $8.7756e+05$ to $8.0016e+05$.

Going forward with this knowledge it was to be expected that corresponding angles φ_1 to φ_4 presented as solid lines in fig. 6.6 would not match the desired reference lines (dashed lines). Angle φ_1 was calculated based on the constant ankle height a . The angles φ_2 and φ_3 then were computed using the nonlinear system solver system `fsolve` that is based on a nonlinear least-squares algorithm. Options were left to their default values. The upper body angle φ_4 directly correlates with the data points of the Bézier curve of the HAT inclination.

Joint torques regarding hip, knee, ankle and virtual toe joint were calculated using inverse dynamics based on the derivation of the joint angles (solid blue lines). As can be seen in fig. 6.7 they do not align with reference data (grey dashed lines), either. For the sake of comparison to the operational space method presented in this thesis, simulations results using this method with x , y and φ as control variables (dotted purple lines) as well as with y and φ as control variables (solid purple lines) are illustrated, too.

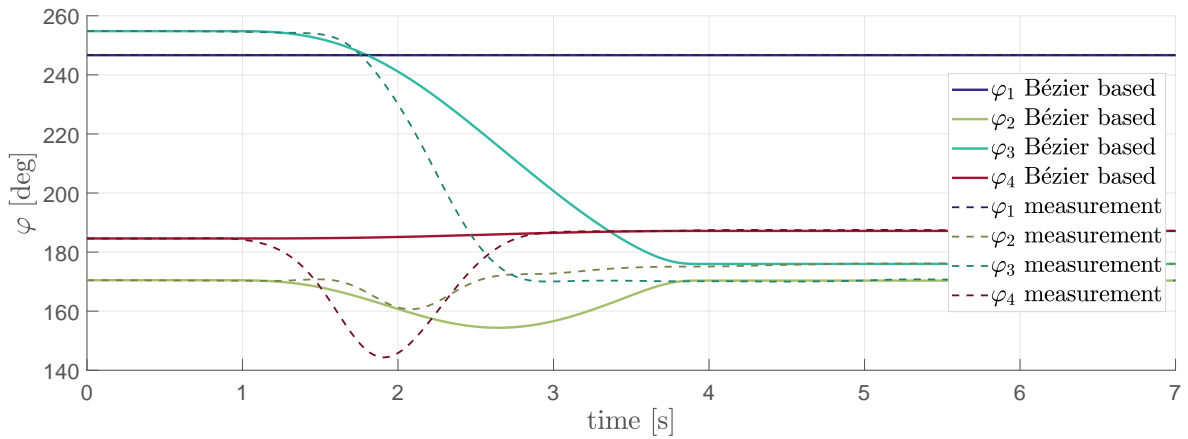


Figure 6.6: Angles φ_1 to φ_4 based on optimized Bézier curves (solid lines) and measurement data (dashed lines) in time.

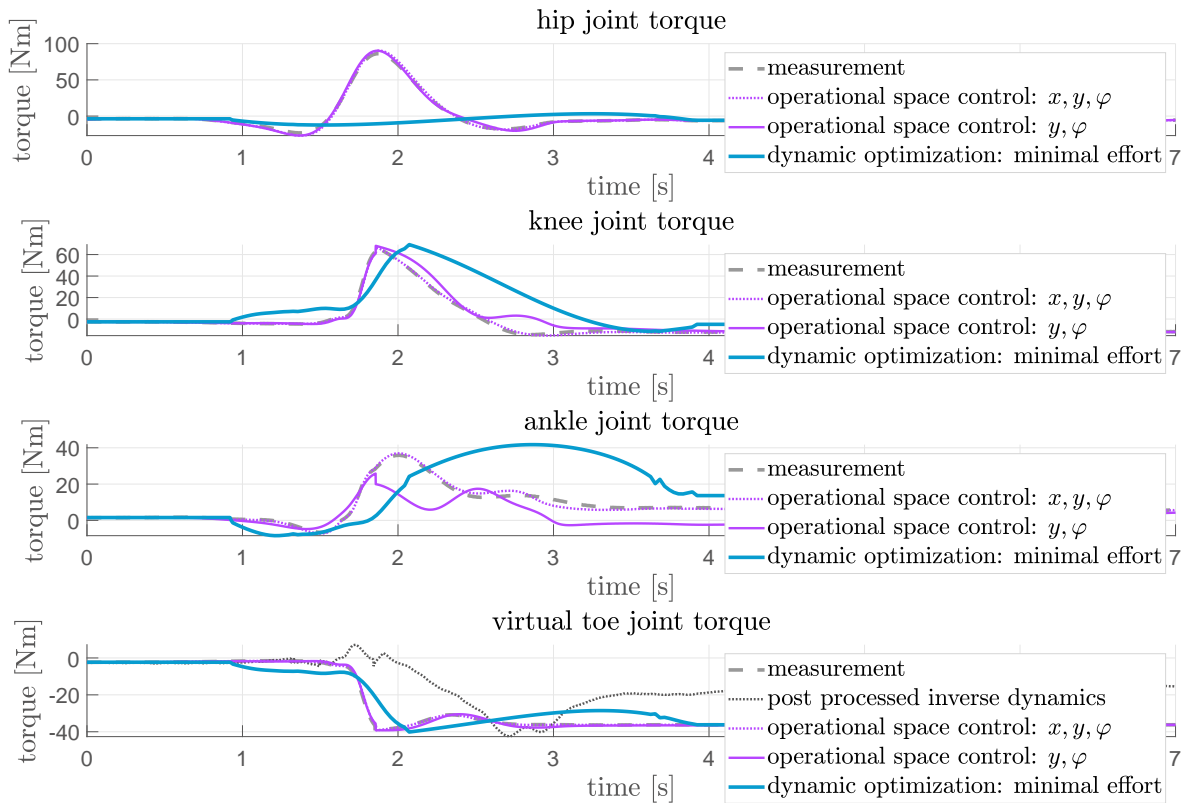


Figure 6.7: Joint torques based on measurement data (dashed gray lines), based on the operational space method with x , y and φ (dotted purple lines) as well as y and φ (solid purple lines) as control variables, and based on dynamic optimization of joint torques (blue solid lines).

In order to test whether the optimization yields better results when the initial Bézier curves are closer to reference data, four intermediate control points based on the measurement were chosen to begin with (cf. fig. 6.8). But again, optimized curves did not come close to the reference. Contrary to Norman-Gerum's findings, after the optimization the upper body still remains relatively stiff with an inclination angle that is roughly constant. The Y -position of the hip remains unchanged w.r.t. the initial curve. Only the hip X -location converges to reference data at the beginning, but the results are all in all similar to the optimization results in fig. 6.5. This might be an indication that humans do not only try to minimize mechanical effort while standing up from a sitting position.

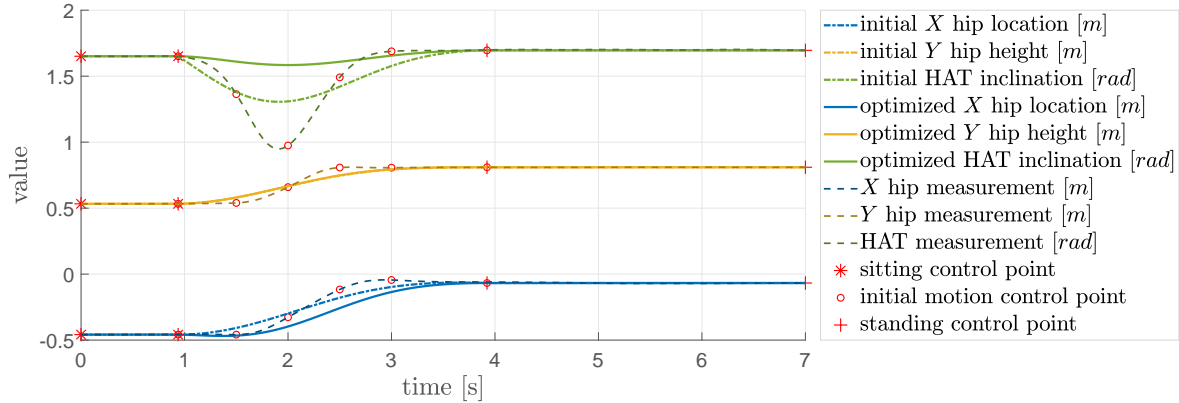


Figure 6.8: Three Bézier curves describing the initial (dot-dashed lines), final (solid lines) and reference (dashed lines) STS motion paths with sitting, motion and standing component based on initial curves that are approximated to measurement data.

Summarized, the torque-driven method from Norman-Gerum does not yield a satisfactory result. Although similar to the proposed method of chapter 4.4 concerning the computation of torques in joint space based on some reference trajectories in task space, Norman-Gerum’s approach uses global optimization based on inverse dynamics data, which is costly and time consuming with computation times of minutes or even hours depending on the option settings. The proposed operational space method, in contrast, utilizes optimization with regard to the employment of pseudo-inverses of the Jacobian matrix, but emerges as more accurate and softer in respect of joint torque and joint angle simulations. It is also more efficient considering the computation times. Even though the operational space method is coming up short in not being purely predictive at this point, since measurement data is used to compute desired end-effector command variables, this issue can be handled in the future, for example through modeling command variables at position level through Bézier curves or other splines. An experimental study to analyze end-effector trajectories of a large group of test subjects would have to be conducted in order to be able to describe general control points, for instance at event markers.

7 Conclusions and outlook

7.1 Contributions

An operational space control approach was successfully implemented for the real-time motion prediction of the human sit-to-stand transfer, one of the most challenging and important tasks of everyday living. To this end, human system kinematics were modeled through a four-link rigid model in the sagittal plane based on subject related anthropometric and measurement data of performed STS experiments. The typical three-link model was therefore extended by an additional rigid link presenting both feet fixed to the ground through a revolute joint at the human toe joint. This turned out to be a good representation of reality, since measured feet motions could thereby be factored in. Model dynamics of the quadruple pendulum were enhanced by the proposed Gaussian function model to replicate the contact forces between chair and buttocks during sitting. This mathematical modeling approach was compared to the implementation of a literature based visco-hyperelastic Kelvin-Voigt model with a Mooney-Rivlin spring and proved to be more accurate w.r.t. measured contact forces.

The proposed inverse dynamics control scheme in operational space resolves redundancies at kinematic level within the posture space of the task, giving freedom to the choice of the pseudo-inverse of the Jacobian matrix. Utilizing a general projector matrix in the null space of the Jacobian, the method is, as in Khatib's works, decoupled in task and posture control in order to accomplish posture objectives without interfering with the operational task. Herein the head location was employed within the task control, whereas the orientation of the foot related link was utilized as a posture command variable with the advantage of presenting only one additional parameter that is easy to define, even without the need for experimental setups. The proposed method emerges as being all in all general, yet powerful and fairly simple in its application to the STS motion. It allows for exact error specifications of the end-effector control variables in Cartesian space.

Two simulation approaches were analyzed regarding the definition of command variables at task level. For both approaches an inertia weighted pseudo-inverse of the Jacobian was implemented within task control. In approach one the end-effector x - and y -position and its orientation were given as input reference data and another inertia weighted pseudo-inverse was employed at posture level, since it yielded the best results compared to the implementation of a Moore-Penrose and a general pseudo-

inverse. In approach two a reduced set of command variables, only the y -position and orientation of the end-effector, was employed along with a general pseudo-inverse for the posture control. Simulation results in approach one showed that very accurate tracking of the head trajectory in real-time as well as overall conformity of joint angles, angular velocities and accelerations with measurement based values could be achieved. Unmeasurable joint torques were reliably predicted with regard to computed torques through inverse dynamics calculations based on measurement data. Approach two demonstrated slightly worse results, mostly concentrated in errors of ankle joint parameters, but still yielded acceptable approximations for toe, knee and hip. Qualitative torque curve progressions comply with literature curves for STS motions. Only peak torque values differ, possibly because of differences in joint coordination strategies and experimental setups.

The method was validated by comparison to a recent torque-driven optimization-based motion generation method from the literature, illustrating its superiority. Not only is it much faster, but it emerges as more accurate and softer in respect of joint torque and joint angle simulations than the validation method that did not yield satisfactory outcomes.

In sum, a physiologically accurate performance prediction could be realized with the proposed method in operational space on the basis of suitable pseudo-inverses of the Jacobian matrix. For the regarded human STS motion it can be concluded that task space control is more reflective of how the nervous system controls this task and more accurate than joint space control.

7.2 Limitations and outlook

Although appropriate pseudo-inverses of the Jacobian matrix were found and minimizing the kinetic energy seems to be the system's goal in approach one, no biomechanical interpretation, in the sense of what fundamental objective is processed by the neural system and underlies the specific motion, can be generally derived at this point, since in approach two a general pseudo-inverse with unclear physical interpretation proved to yield the most accurate results. Extended experimental testing has to be carried out regarding an extension of the subject pool, since so far only five viable measurements of one subject were conducted. This would help in analyzing the general applicability of the proposed pseudo-inverses. Also, this way the Gaussian function contact force model could be generalized and validated for larger groups of people of similar body

dimensions. Besides, the transmission of the Gaussian function model onto the biomechanical model comprises limitations in itself considering the lack of a realistic design for the rolling of the center of pressure on the chair surface. Further enquiries have to be undertaken in the future.

The skeletal model represents a simplification of the human body, where motion is constrained to the sagittal plane and symmetry as well as ideal joints are assumed. Limitations of realistic modeling of the human body are based on decisions that had to be made due to measurement inaccuracies and restrictions with regard to the data transmission from 3D to 2D. This includes the presented computation of segment lengths based on variable measurement data and of anthropometric data considering symmetric movement. Furthermore, head tilt itself and arms' swings were not considered at all, which, in addition, leads to imprecisions in portraying biomechanical reality. Future model improvements would include the consideration of muscle forces, the inclusion of the arms and the head as a separate unit as well as a possible extension to the three-dimensional space.

Since experimental data functions as input data to the forward dynamic simulations in the form of initial condition to the integration process as well as of the desired head trajectory that is tracked, the employed operational space control approach currently does not constitute a purely predictive method. However, this can be tackled in the future through generalizing reference trajectories through splines such as Bézier curves.

Finally, with regard to what-if simulations for intervention based STS analyses and proceeding pathological STS predictions, the method needs to be tested on a variety of STS experiments including numerous test subjects, varying chair heights and possible external weights in order to validate its application for this field.

Appendices

A Results to introductory example

A.1 Computation routine

The implementation was done in MATLAB using the routine `place` for the pole placement which is based on the algorithm of Kautsky et al. [36]. Direct dynamics is calculated using `ode45` to solve the differential equations numerically over a period of time on the basis of predefined initial conditions. Initial values for the state vector were taken from the measurement (cf. chapter 3). The integration time interval was defined as 0.0 s to 2.3 s with a step size of 1 ms . Further integration options were defined as `RelTol` = 10^{-11} and `AbsTol` = 10^{-10} , while all other options were left to their default settings. The cost function was evaluated by `fmincon` using the interior-point algorithm with `OptTol` = 10^{-8} and `StepTol` = 10^{-9} .

A.2 Cost function values of optimization process

Cost function values were minimized according to fig. 1:

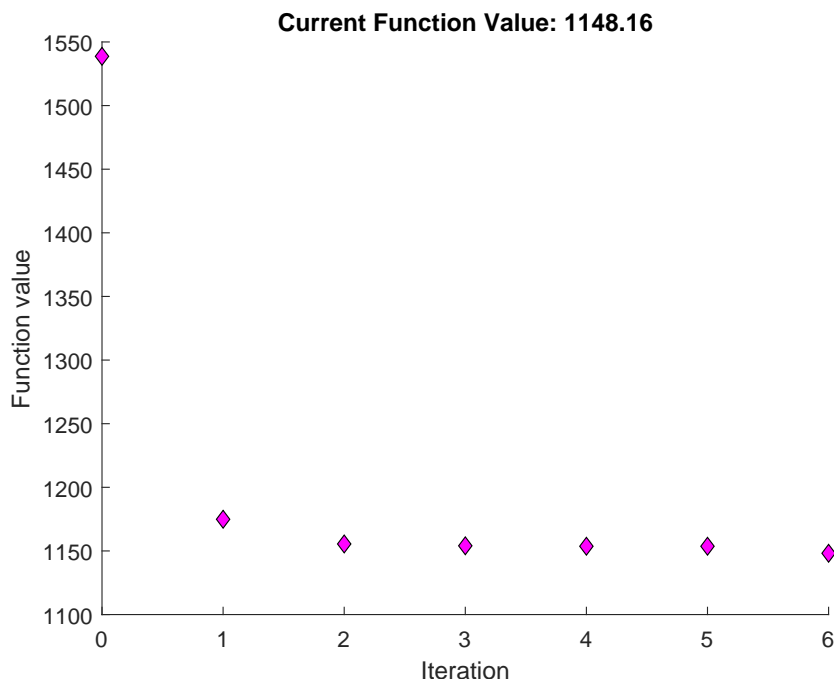


Figure 1: Cost function values w.r.t. the number of iterations.

A.3 Joint angles, angular velocities and angular accelerations

Green dashed lines show the simulation based time histories of angles, angular rates and accelerations with corresponding rates (from left to right) of hip, knee and ankle joint (from top to bottom). Reference measurement data (as used in chapter 5) are illustrated in light gray:

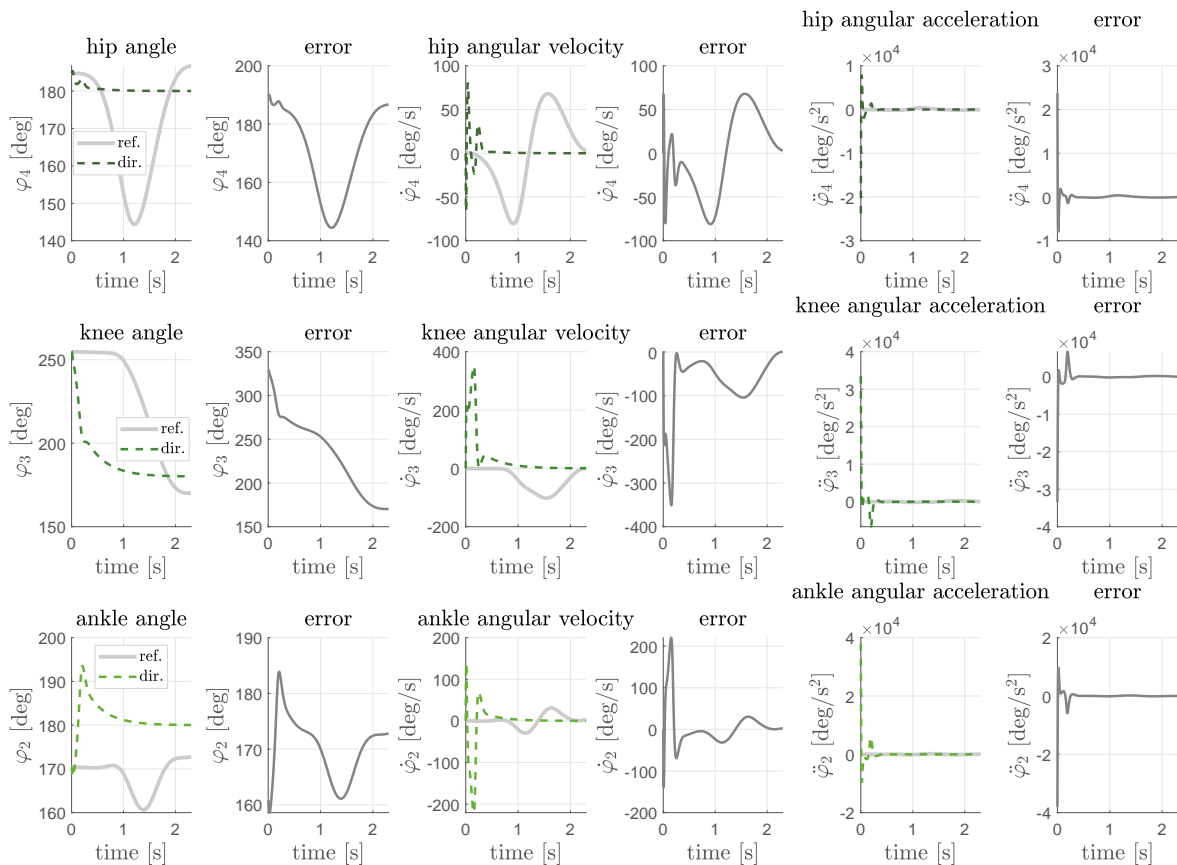


Figure 2: Time series of joint angles and angular rates of reference (ref.) and direct dynamics computations (dir.) with corresponding errors for the method of pole placement.

A.4 Joint torques

Hip, knee and ankle joint torques w.r.t. time before (dot-dashed lines) and after (solid lines) the iterative optimization, without considering supporting contact forces of the chair:

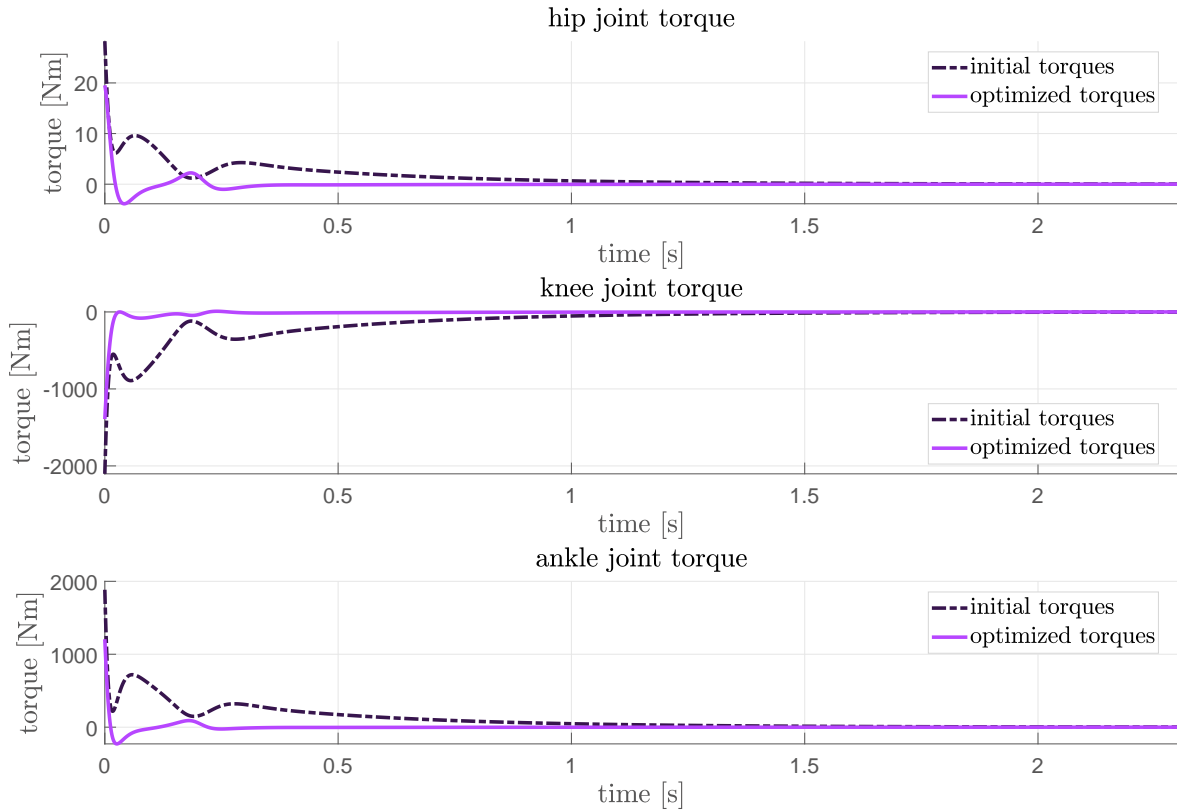


Figure 3: Joint torques regarding hip extension, knee extension and ankle dorsiflexion for the method of pole placement before and after the optimization process regarding mechanical energy.

B Range and null space of the Jacobian matrix

At the instantaneous manipulator configuration, the range $\mathcal{R}(\mathbf{J})$ is a subspace of \mathbb{R}^r which is spanned by the end-effector velocities $\dot{\mathbf{x}}$ that can be produced by the joint velocities $\dot{\mathbf{q}}$:

$$\mathcal{R}(\mathbf{J}) = \{ \dot{\mathbf{x}}_e \mid \dot{\mathbf{x}}_e = \mathbf{J} \dot{\mathbf{q}} \},$$

where the dependence on \mathbf{q} has been omitted for the sake of clarity.

The null space $\mathcal{N}(\mathbf{J})$ is a subspace of \mathbb{R}^n which is spanned by the joint velocities $\dot{\mathbf{q}}$ that do not generate any end-effector velocity:

$$\mathcal{N}(\mathbf{J}) = \{ \dot{\mathbf{q}} \mid \mathbf{J} \dot{\mathbf{q}} = \mathbf{0} \}.$$

C Equations of motion of quadruple pendulum

$$\mathbf{A}(\mathbf{q})\ddot{\mathbf{q}} + \mathbf{b}(\mathbf{q}, \dot{\mathbf{q}}) - \mathbf{g}(\mathbf{q}) - \mathbf{Q}(\mathbf{q}, \dot{\mathbf{q}}) = \mathbf{\Gamma}$$

$$\begin{bmatrix} m_1 s_1^2 + m_2 l_1^2 + m_4 l_1^2 + J_1 & \cos(\varphi_1 - \varphi_2) \cdot (m_2 l_1 s_2 + m_3 l_1 l_2 + m_4 l_1 l_2) & \cos(\varphi_1 - \varphi_3) \cdot (m_3 l_1 s_3 + m_4 l_1 l_3) & \cos(\varphi_1 - \varphi_4) \cdot m_4 l_1 s_4 \\ \cos(\varphi_1 - \varphi_2) \cdot (m_2 l_1 s_2 + m_3 l_1 l_2 + m_4 l_1 l_2) & m_2 s_2^2 + m_3 l_2^2 + m_4 l_2^2 + J_2 & \cos(\varphi_2 - \varphi_3) \cdot (m_3 l_2 s_3 + m_4 l_2 l_3) & \cos(\varphi_2 - \varphi_4) \cdot m_4 l_2 s_4 \\ \cos(\varphi_1 - \varphi_3) \cdot (m_3 l_1 s_3 + m_4 l_1 l_3) & \cos(\varphi_2 - \varphi_3) \cdot (m_3 l_2 s_3 + m_4 l_2 l_3) & m_3 s_3^2 + m_4 l_3^2 + J_3 & \cos(\varphi_3 - \varphi_4) \cdot m_4 l_3 s_4 \\ \cos(\varphi_1 - \varphi_4) \cdot m_4 l_1 s_4 & \cos(\varphi_2 - \varphi_4) \cdot m_4 l_2 s_4 & \cos(\varphi_3 - \varphi_4) \cdot m_4 l_3 s_4 & m_4 s_4^2 + J_4 \end{bmatrix} \cdot \begin{bmatrix} \ddot{\varphi}_1 \\ \ddot{\varphi}_2 \\ \ddot{\varphi}_3 \\ \ddot{\varphi}_4 \end{bmatrix}$$

$$+ \begin{bmatrix} \dot{\varphi}_2^2 \sin(\varphi_1 - \varphi_2) \cdot (m_2 l_1 s_2 + m_3 l_1 l_2 + m_4 l_1 l_2) + \dot{\varphi}_3^2 \sin(\varphi_1 - \varphi_3) \cdot (m_3 l_1 s_3 + m_4 l_1 l_3) + \dot{\varphi}_4^2 \sin(\varphi_1 - \varphi_4) \cdot m_4 l_1 s_4 \\ -\dot{\varphi}_1^2 \sin(\varphi_1 - \varphi_2) \cdot (m_2 l_1 s_2 + m_3 l_1 l_2 + m_4 l_1 l_2) + \dot{\varphi}_3^2 \sin(\varphi_2 - \varphi_3) \cdot (m_3 l_2 s_3 + m_4 l_2 l_3) + \dot{\varphi}_4^2 \sin(\varphi_2 - \varphi_4) \cdot m_4 l_2 s_4 \\ -\dot{\varphi}_1^2 \sin(\varphi_1 - \varphi_3) \cdot (m_3 l_1 s_3 + m_4 l_1 l_3) - \dot{\varphi}_2^2 \sin(\varphi_2 - \varphi_3) \cdot (m_3 l_2 s_3 + m_4 l_2 l_3) + \dot{\varphi}_4^2 \sin(\varphi_3 - \varphi_4) \cdot m_4 l_3 s_4 \\ -\dot{\varphi}_1^2 \sin(\varphi_1 - \varphi_4) \cdot m_4 l_1 s_4 - \dot{\varphi}_2^2 \sin(\varphi_2 - \varphi_4) \cdot m_4 l_2 s_4 - \dot{\varphi}_3^2 \sin(\varphi_3 - \varphi_4) \cdot m_4 l_3 s_4 \end{bmatrix}$$

$$+ \begin{bmatrix} (m_1 s_1 + m_2 l_1 + m_3 l_1 + m_4 l_1) \cdot g \sin \varphi_1 \\ (m_2 s_2 + m_3 l_2 + m_4 l_2) \cdot g \sin \varphi_2 \\ (m_3 s_3 + m_4 l_3) \cdot g \sin \varphi_3 \\ m_4 s_4 \cdot g \sin \varphi_4 \end{bmatrix} - \begin{bmatrix} l_1 \cos \varphi_1 & l_1 \sin \varphi_1 \\ l_2 \cos \varphi_2 & l_2 \sin \varphi_2 \\ (l_3 - b_x) \cos \varphi_3 & (l_3 - b_y) \sin \varphi_3 \\ 0 & 0 \end{bmatrix} \cdot \begin{bmatrix} F_{b_x} \\ F_{b_y} \end{bmatrix} = \begin{bmatrix} \Gamma_1 \\ \Gamma_2 \\ \Gamma_3 \\ \Gamma_4 \end{bmatrix}$$

D Gaussian function buttocks force fit

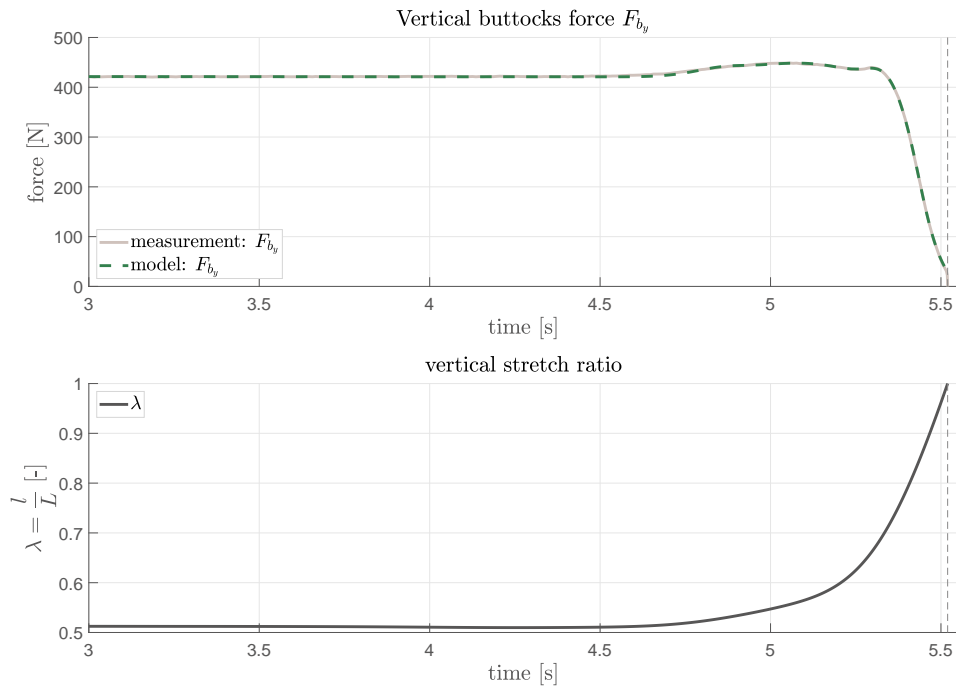


Figure 4: Approximated vertical contact force F_{b_y} using Gaussian function (upper plot) and vertical stretch ratio λ w.r.t. time (lower plot).

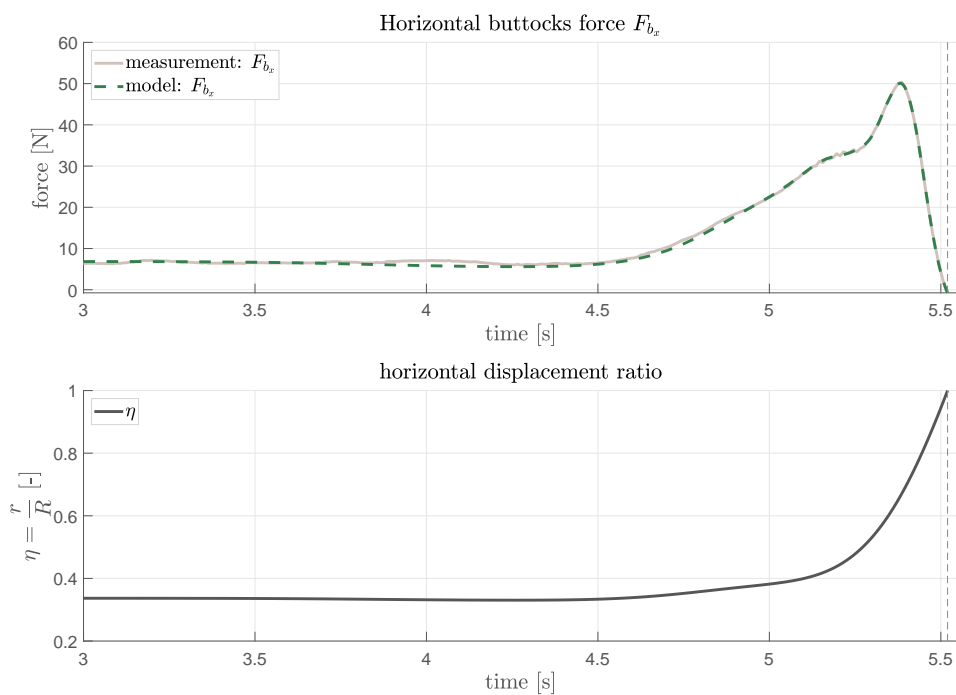


Figure 5: Approximated horizontal contact force F_{b_x} using Gaussian function (upper plot) and horizontal displacement ratio η w.r.t. time (lower plot).

E Dynamically consistent pseudo-inverse of the Jacobian matrix

Although eq. (4.11) in general provides freedom in the choice of the pseudo-inverse of the Jacobian matrix \mathbf{J}^* , such that $\mathbf{J} = \mathbf{J}\mathbf{J}^*\mathbf{J}$, the end-effector acceleration in eq. (4.2) acts as a constraint to this free choice. Inserting the general equation for the generalized joint forces

$$\boldsymbol{\Gamma} = \mathbf{J}^T(\mathbf{q})\mathbf{F} + [\mathbf{I} - \mathbf{J}^T(\mathbf{q})\mathbf{J}^{*T}(\mathbf{q})]\boldsymbol{\Gamma}_0 \quad (1)$$

into the general expression for end-effector accelerations of eq. (4.2) yields

$$\begin{aligned} \ddot{\mathbf{x}} = & \mathbf{J}(\mathbf{q})\mathbf{A}^{-1}(\mathbf{q})\mathbf{J}^T(\mathbf{q})\mathbf{F} + \mathbf{J}(\mathbf{q})\mathbf{A}^{-1}(\mathbf{q})[\mathbf{I} - \mathbf{J}^T(\mathbf{q})\mathbf{J}^{*T}(\mathbf{q})]\boldsymbol{\Gamma}_0 - \\ & - \mathbf{J}(\mathbf{q})\mathbf{A}^{-1}(\mathbf{q})\mathbf{b}(\mathbf{q}, \dot{\mathbf{q}}) + \mathbf{J}(\mathbf{q})\mathbf{A}^{-1}(\mathbf{q})\mathbf{g}(\mathbf{q}) + \dot{\mathbf{J}}(\mathbf{q})\dot{\mathbf{q}}. \end{aligned} \quad (2)$$

In order for the joint forces within the null space not to alter the end-effector dynamics behavior, the dynamic effects of the joint forces corresponding to the null space need to be canceled [48]:

$$\mathbf{J}(\mathbf{q})\mathbf{A}^{-1}(\mathbf{q})[\mathbf{I} - \mathbf{J}^T(\mathbf{q})\mathbf{J}^{*T}(\mathbf{q})]\boldsymbol{\Gamma}_0 \stackrel{!}{=} \mathbf{0}. \quad (3)$$

The generalized inverse of the Jacobian matrix is then said to be dynamically consistent [49]. This is achieved by choosing $\mathbf{J}^* = \bar{\mathbf{J}}$:

$$\begin{aligned} \mathbf{J}(\mathbf{q})\mathbf{A}^{-1}(\mathbf{q})[\mathbf{I} - \mathbf{J}^T(\mathbf{q})\bar{\mathbf{J}}^T(\mathbf{q})]\boldsymbol{\Gamma}_0 &= \mathbf{0} \\ \mathbf{J}(\mathbf{q})\mathbf{A}^{-1}(\mathbf{q})[\mathbf{I} - \mathbf{J}^T(\mathbf{q})\boldsymbol{\Lambda}_r(\mathbf{q})\mathbf{J}(\mathbf{q})\mathbf{A}^{-1}(\mathbf{q})]\boldsymbol{\Gamma}_0 &= \mathbf{0} \\ \mathbf{J}(\mathbf{q})\mathbf{A}^{-1}(\mathbf{q})\boldsymbol{\Gamma}_0 - \underbrace{\mathbf{J}(\mathbf{q})\mathbf{A}^{-1}(\mathbf{q})\mathbf{J}^T(\mathbf{q})\boldsymbol{\Lambda}_r(\mathbf{q})\mathbf{J}(\mathbf{q})\mathbf{A}^{-1}(\mathbf{q})}_{\boldsymbol{\Lambda}_r^{-1}(\mathbf{q})}\boldsymbol{\Gamma}_0 &= \mathbf{0} \\ \mathbf{J}(\mathbf{q})\mathbf{A}^{-1}(\mathbf{q})\boldsymbol{\Gamma}_0 - \underbrace{\boldsymbol{\Lambda}_r^{-1}(\mathbf{q})\boldsymbol{\Lambda}_r(\mathbf{q})}_{\mathbf{I}}\mathbf{J}(\mathbf{q})\mathbf{A}^{-1}(\mathbf{q})\boldsymbol{\Gamma}_0 &= \mathbf{0} \\ \mathbf{J}(\mathbf{q})\mathbf{A}^{-1}(\mathbf{q})\boldsymbol{\Gamma}_0 - \mathbf{J}(\mathbf{q})\mathbf{A}^{-1}(\mathbf{q})\boldsymbol{\Gamma}_0 &= \mathbf{0} \\ \mathbf{0} &= \mathbf{0} \end{aligned}$$

As can be seen, the choice of the pseudo-inverse of the Jacobian matrix is bound to the choice of the null operational force vector, which, in this case, is said to be $[\mathbf{I} - \mathbf{J}^T(\mathbf{q})\bar{\mathbf{J}}^T(\mathbf{q})]\boldsymbol{\Gamma}_0$.

F Simulation results of triple pendulum

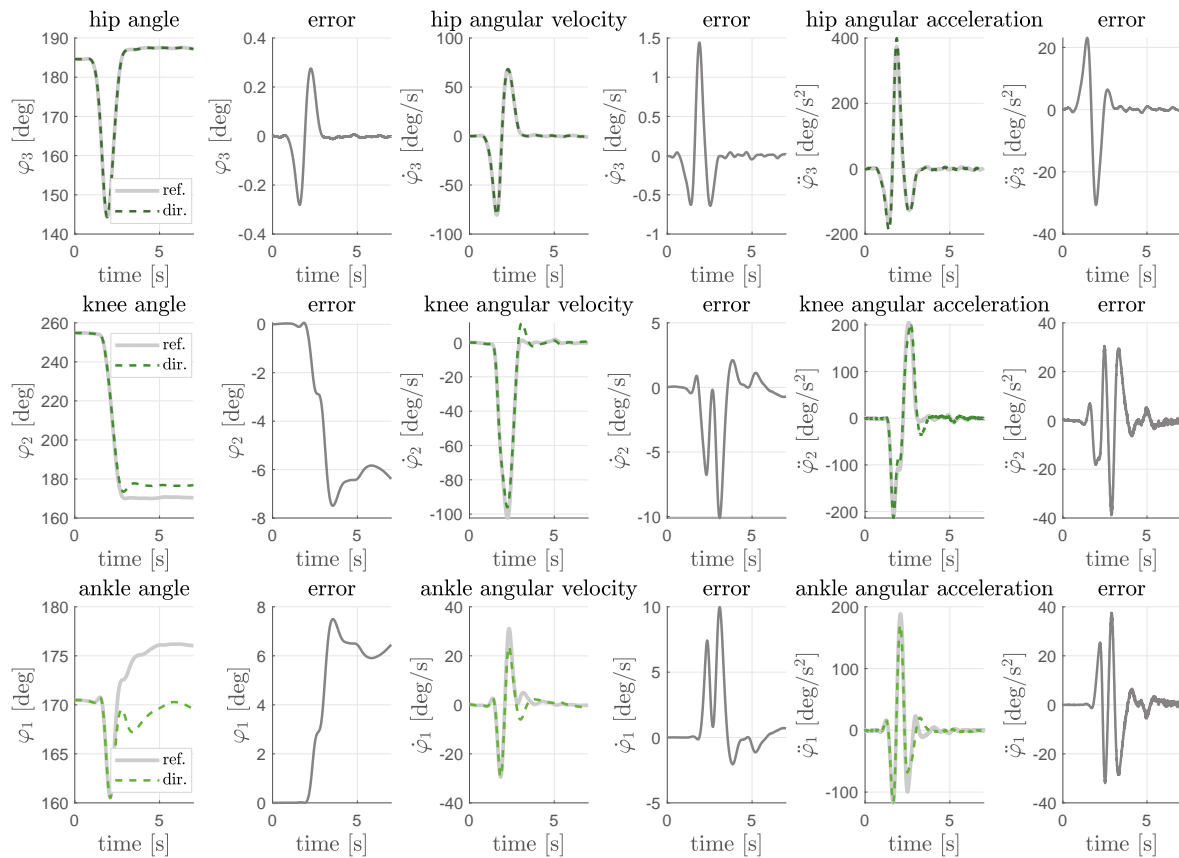


Figure 6: Time series of joint angles of hip (φ_3), knee (φ_2) and ankle joint (φ_1) with corresponding angular velocities and angular accelerations of reference data (ref.) and direct dynamics computations (dir.); related errors of simulation data w.r.t. reference data are plotted on the right, respectively.

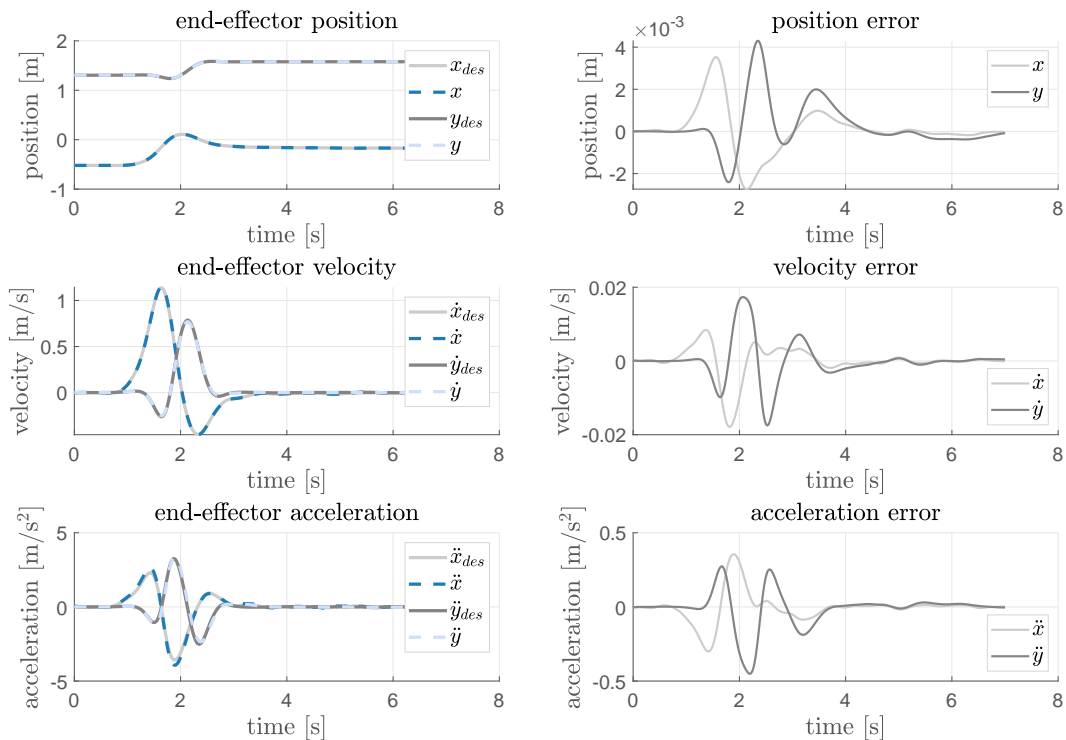


Figure 7: End-effector position, velocity, acceleration and corresponding errors w.r.t. actual and desired trajectories.

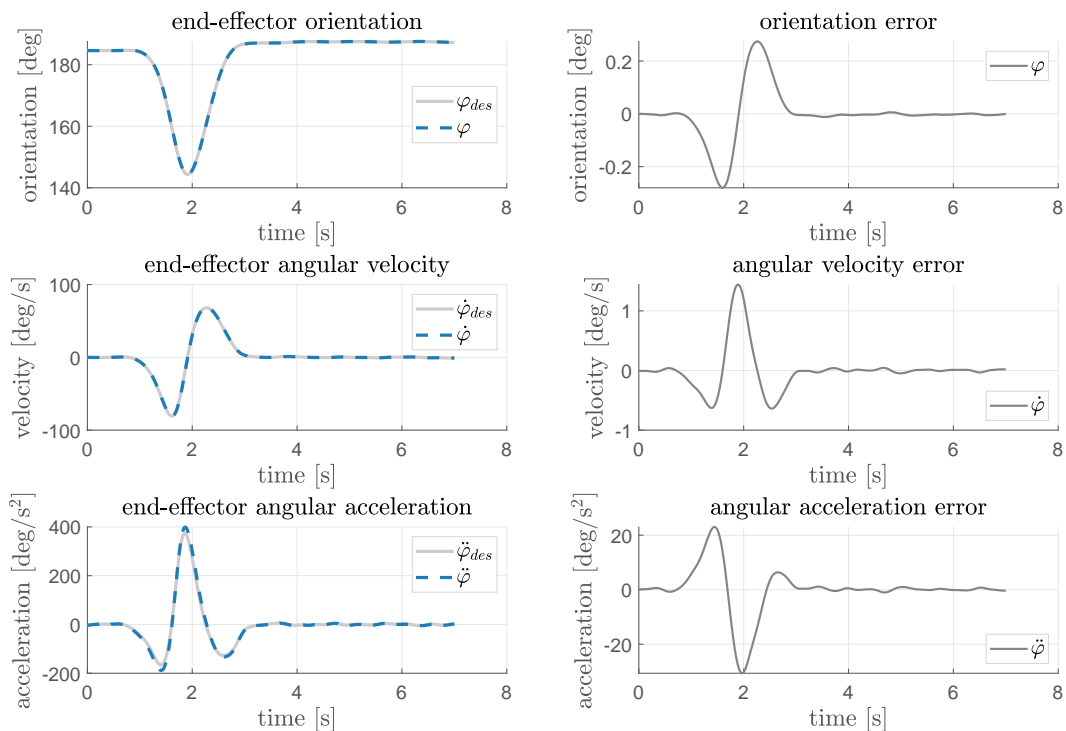


Figure 8: End-effector orientation, angular velocity, angular acceleration and corresponding errors w.r.t. actual and desired trajectories.

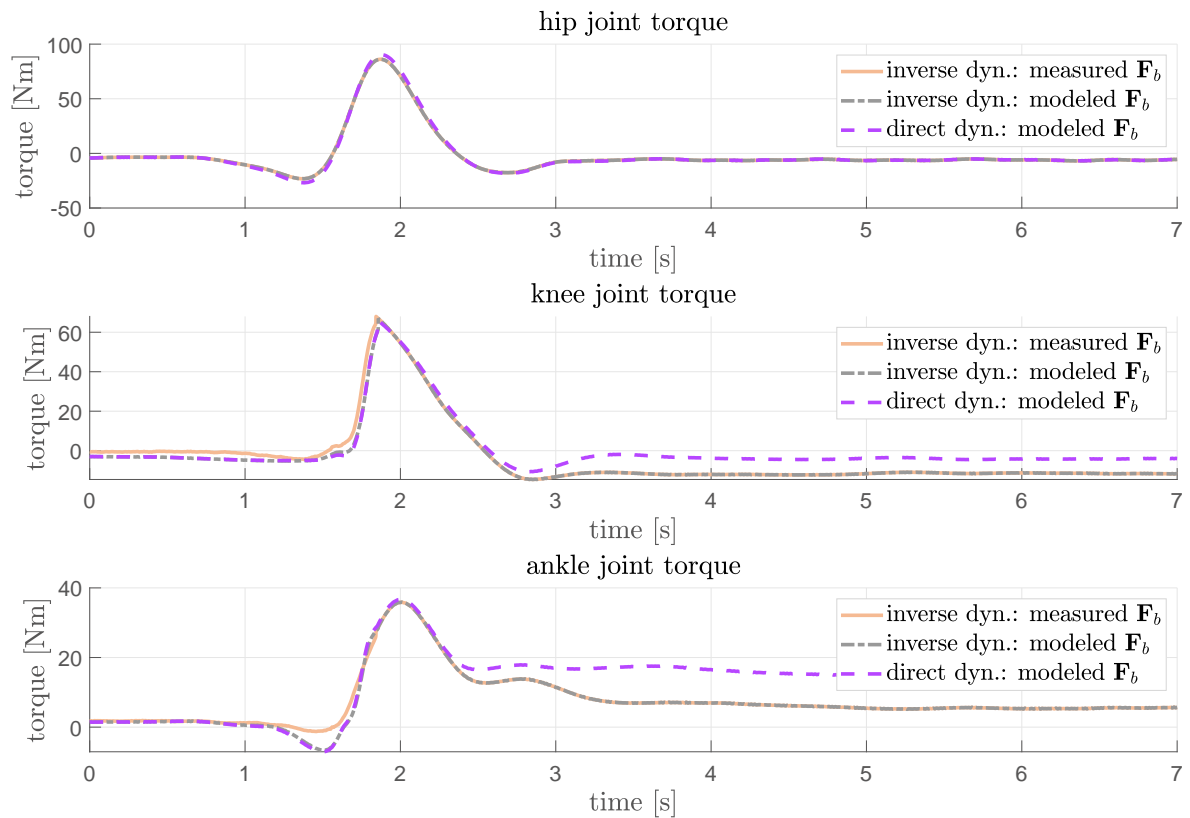


Figure 9: Joint torques regarding hip extension, knee extension and ankle dorsiflexion of inverse dynamics computations based on measured and modeled buttocks contact forces \mathbf{F}_b as well as of direct dynamics calculations with modeled buttocks forces.

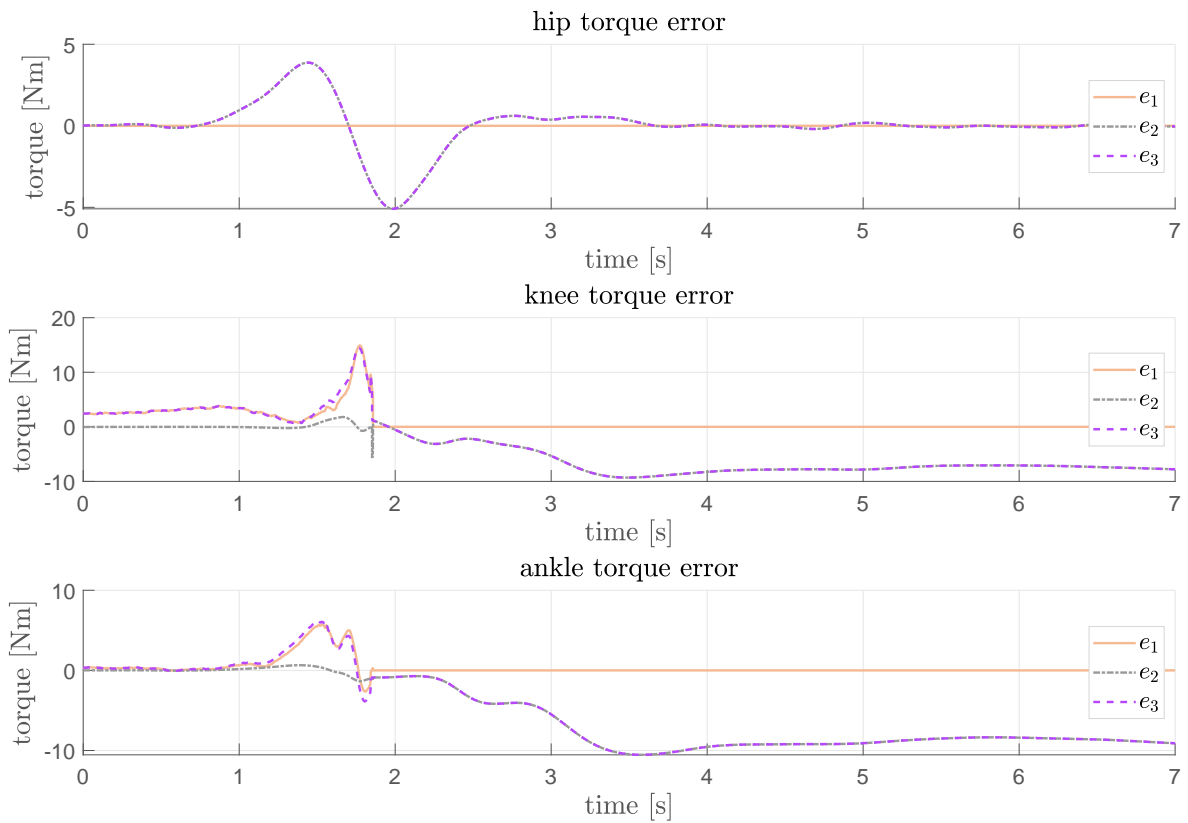


Figure 10: Joint torque errors: e_1 is the error between the inverse dynamics joint torques based on measured buttocks forces and based on modeled buttocks forces; e_2 is the error between the simulated torques and the torques resulting from inverse dynamics calculations with modeled buttocks forces; e_3 is the error between the simulated torques and the torques resulting from inverse dynamics calculations with measured buttocks forces.

Bibliography

- [1] R. Aissaoui and J. Dansereau. Biomechanical analysis and modelling of sit to stand task: a literature review. In *Systems, Man, and Cybernetics, 1999. IEEE SMC'99 Conference Proceedings. 1999 IEEE International Conference*, volume 1, pages 141–146. IEEE, 1999.
- [2] U. P. Arborelius, P. Wretenberg, and F. Lindberg. The effects of armrests and high seat heights on lower-limb joint load and muscular activity during sitting and rising. *Ergonomics*, 35(11):1377–1391, 1992.
- [3] F. Bahrami, R. Riener, P. Jabedar-Maralani, and G. Schmidt. Biomechanical analysis of sit-to-stand transfer in healthy and paraplegic subjects. *Clinical Biomechanics*, 15(2):123–133, 2000.
- [4] S. Barthélemy, C. Salaun, and P. Bidaud. Dynamic simulation and control of sit-to-stand motion. In *Proceedings of the 9th International Conference on Climbing and Walking Robots (CLAWAR)*, volume 350, 2006.
- [5] O. Brock and O. Khatib. Elastic strips: A framework for motion generation in human environments. *IJRR*, 21(12):1031–1052, Dec. 2002.
- [6] R. G. Burdett, R. Habasevich, J. Pisciotta, and S. R. Simon. Biomechanical comparison of rising from two types of chairs. *Physical Therapy*, 65(8):1177–1183, 1985.
- [7] P. Cerveri, A. Pedotti, and G. Ferrigno. Kinematical models to reduce the effect of skin artifacts on marker-based human motion estimation. *Journal of Biomechanics*, 38(11):2228–2236, 2005.
- [8] K. C. Chang and O. Khatib. Efficient algorithm for extended operational space inertia matrix. In *IROS*, volume 1, pages 350–355, Kyongju, South Korea, Oct. 1999.
- [9] K.-S. Chang and O. Khatib. Operational space dynamics: Efficient algorithms for modeling and control of branching mechanisms. In *Proceedings 2000 ICRA. Millennium Conference. IEEE International Conference on Robotics and Automation. Symposia Proceedings (Cat. No. 00CH37065)*, volume 1, pages 850–856. IEEE, 2000.

-
- [10] P.-T. Cheng, M.-Y. Liaw, M.-K. Wong, F.-T. Tang, M.-Y. Lee, and P.-S. Lin. The sit-to-stand movement in stroke patients and its correlation with falling. *Archives of physical medicine and rehabilitation*, 79(9):1043–1046, 1998.
- [11] S. Chiaverini, L. Sciavicco, and B. Siciliano. Control of robotic systems through singularities. In *Advanced Robot Control*, pages 285–295. Springer, 1991.
- [12] E. A. Chumacero-Polanco and J. Yang. A review on human motion prediction in sit to stand and lifting tasks. In *International Design Engineering Technical Conferences and Computers and Information in Engineering Conference*, volume 50077, page V01AT02A066. American Society of Mechanical Engineers, 2016.
- [13] V. De Sapio, J. Warren, and O. Khatib. Predicting reaching postures using a kinematically constrained shoulder model. In *Advances in robot kinematics*, pages 209–218. Springer, 2006.
- [14] V. De Sapio, J. Warren, O. Khatib, and S. Delp. Simulating the task-level control of human motion: a methodology and framework for implementation. *The Visual Computer*, 21(5):289–302, 2005.
- [15] E. Demircan, T. Besier, S. Menon, and O. Khatib. Human motion reconstruction and synthesis of human skills. In *Advances in Robot Kinematics: Motion in Man and Machine*, pages 283–292. Springer, 2010.
- [16] E. Demircan, L. Sentis, V. De Sapio, and O. Khatib. Human motion reconstruction by direct control of marker trajectories. In *Advances in Robot Kinematics: Analysis and Design*, pages 263–272. Springer, 2008.
- [17] R. Drillis and R. Contini. Body segment parameters (report no. 1166-03). *Office of Vocational Rehabilitation, Department of Health, Education, and Welfare. New York University School of Engineering and Science, New York*, 1966.
- [18] M. L. Felis and K. Mombaur. Using optimal control methods to generate human walking motions. In *International Conference on Motion in Games*, pages 197–207. Springer, 2012.
- [19] M. Fujimoto and L.-S. Chou. Dynamic balance control during sit-to-stand movement: an examination with the center of mass acceleration. *Journal of biomechanics*, 45(3):543–548, 2012.
- [20] B. A. Garner. *A dynamic musculoskeletal computer model for rising from a squatting or sitting position: a study of performance criteria for optimal control*

- of non-ballistic human movements*. Dissertation, University of Texas at Austin, 1992.
- [21] M. Geerligs, G. W. Peters, P. A. Ackermans, C. W. Oomens, and F. Baaijens. Linear viscoelastic behavior of subcutaneous adipose tissue. *Biorheology*, 45(6):677–688, 2008.
- [22] M. Geravand, P. Z. Korondi, and A. Peer. Human sit-to-stand transfer modeling for optimal control of assistive robots. In *5th IEEE RAS/EMBS International Conference on Biomedical Robotics and Biomechatronics*, pages 670–676. IEEE, 2014.
- [23] W. Gilleard, J. Crosbie, and R. Smith. A longitudinal study of the effect of pregnancy on rising to stand from a chair. *Journal of biomechanics*, 41(4):779–787, 2008.
- [24] J. C. Gillette and C. A. Stevermer. The effects of symmetric and asymmetric foot placements on sit-to-stand joint moments. *Gait & posture*, 35(1):78–82, 2012.
- [25] M. Gross, P. Stevenson, S. Charette, G. Pyka, and R. Marcus. Effect of muscle strength and movement speed on the biomechanics of rising from a chair in healthy elderly and young women. *Gait & posture*, 8(3):175–185, 1998.
- [26] H. Hanafusa, T. Yoshikawa, and Y. Nakamura. Analysis and control of articulated robot arms with redundancy. *IFAC Proceedings Volumes*, 14(2):1927–1932, 1981.
- [27] H. Hemami and V. C. Jaswa. On a three-link model of the dynamics of standing up and sitting down. *IEEE Transactions on Systems, Man, and Cybernetics*, 8(2):115–120, 1978.
- [28] K.-L. H. Hoang and K. D. Mombaur. Optimal design of a physical assistive device to support sit-to-stand motions. In *2015 IEEE International Conference on Robotics and Automation (ICRA)*, pages 5891–5897. IEEE, 2015.
- [29] J. Hollerbach and K. Suh. Redundancy resolution of manipulators through torque optimization. *IEEE Journal on Robotics and Automation*, 3(4):308–316, 1987.
- [30] K. R. Holzbaur, W. M. Murray, and S. L. Delp. A model of the upper extremity for simulating musculoskeletal surgery and analyzing neuromuscular control. *Annals of biomedical engineering*, 33(6):829–840, 2005.

-
- [31] E. Hsu, S. Gentry, and J. Popović. Example-based control of human motion. In *Proceedings of the 2004 ACM SIGGRAPH/Eurographics symposium on Computer animation*, pages 69–77, 2004.
- [32] M. Hughes, D. Weiner, M. Schenkman, R. Long, and S. Studenski. Chair rise strategies in the elderly. *Clinical biomechanics*, 9(3):187–192, 1994.
- [33] R. Jamisola, M. H. Ang, D.-N. Oetomo, O. Khatib, T.-M. Lim, and S.-Y. Lim. The operational space formulation implementation to aircraft canopy polishing using a mobile manipulator. In *ICRA*, volume 1, pages 400–405, Washington, DC, USA, May 2002.
- [34] W. G. Janssen, H. B. Bussmann, and H. J. Stam. Determinants of the sit-to-stand movement: a review. *Physical therapy*, 82(9):866–879, 2002.
- [35] S. Jatsun, S. Savin, A. Yatsun, and R. Turlapov. Adaptive control system for exoskeleton performing sit-to-stand motion. In *2015 10th International Symposium on Mechatronics and Its Applications (ISMA)*, pages 1–6. IEEE, 2015.
- [36] J. Kautsky, N. K. Nichols, and P. Van Dooren. Robust pole assignment in linear state feedback. *International Journal of control*, 41(5):1129–1155, 1985.
- [37] S. Kawagoe, N. Tajima, and E. Chosa. Biomechanical analysis of effects of foot placement with varying chair height on the motion of standing up. *Journal of Orthopaedic Science*, 5(2):124–133, 2000.
- [38] A. Kecskeméthy. Lecture notes in kinematics of robots and mechanisms. Chair of mechanics and robotics, University of Duisburg-Essen, 2019.
- [39] O. Khatib. *Commande dynamique dans l'espace opérationnel des robots manipulateurs en présence d'obstacles*. Dissertation, École Nationale Supérieure de l'Aéronautique et de l'Espace, 1980.
- [40] O. Khatib. Dynamic control of manipulator in operational spaces. In *Proc. 6th IFToMM World Congress on Theory of Machines and Mechanisms*, pages 1128–1131, 1983.
- [41] O. Khatib. Real-time obstacle avoidance for manipulators and mobile robots. *IJRR*, 5(1):90–98, Spring 1986.
- [42] O. Khatib. Robot manipulator control in operational space. In *Proc. of the CNRS Symposium on Mathematical Tools for Modeling and Control of Robots*, pages 367–391, Paris, France, Sept. 1986. The MIT Press, Cambridge, MA, USA.

-
- [43] O. Khatib. A unified approach for motion and force control of robot manipulators: The operational space formulation. *IEEE Journal on Robotics and Automation*, 3(1):43–53, 1987.
- [44] O. Khatib. The augmented object and reduced effective inertia in robot systems. In *ACC*, volume 3, pages 2140–2147, Atlanta, GA, USA, June 1988.
- [45] O. Khatib. Dynamic control of multi-structure robot systems at the manipulated object level. In Y. Kabil and M. Said, editors, *Current Advances in Mechanical Design and Production IV*, pages 433–440, Cairo, Egypt, Dec. 1988. Pergamon Press, Oxford, UK.
- [46] O. Khatib. Object manipulation in a multi-effector robot system. In R. Bolles and B. Roth, editors, *ISRR*, pages 137–144, Santa Cruz, CA, USA, May 1988. The MIT Press, Cambridge, MA, USA.
- [47] O. Khatib. Object level manipulation. In O. Kaynak, editor, *Proc. of the IEEE International Workshop on Intelligent Motron Control*, pages 497–502, Istanbul, Turkey, Aug. 1990.
- [48] O. Khatib. Reduced effective inertia in macro-/mini-manipulator systems. In *ISRR*, pages 279–284. The MIT Press, Cambridge, MA, USA, 1990.
- [49] O. Khatib. The operational space framework. *JSME international journal. Ser. C, Dynamics, control, robotics, design and manufacturing*, 36(3):277–287, 1993.
- [50] O. Khatib, O. Brock, K.-S. Chang, D. Ruspini, L. Sentis, and S. Viji. Human-centered robotics and interactive haptic simulation. *The International Journal of Robotics Research*, 23(2):167–178, 2004.
- [51] O. Khatib and J. Burdick. Motion and force control of robot manipulators. In *Proceedings. 1986 IEEE International Conference on Robotics and Automation*, volume 3, pages 1381–1386. IEEE, 1986.
- [52] O. Khatib and J. Burdick. Optimization of dynamics in manipulator design: The operational space formulation. *INT. J. ROBOTICS AUTOM.*, 2(2):90–98, 1987.
- [53] O. Khatib, E. Demircan, V. De Sapia, L. Sentis, T. Besier, and S. Delp. Robotics-based synthesis of human motion. *Journal of Physiology-Paris*, 103(3-5):211–219, 2009.

- [54] O. Khatib, L. Sentis, J. Park, and J. Warren. Whole-body dynamic behavior and control of human-like robots. *International Journal of Humanoid Robotics*, 1(01):29–43, 2004.
- [55] O. Khatib, K. Yokoi, K. Chang, D. C. Ruspini, R. Holmberg, and A. Casal. Decentralized cooperation between multiple manipulators. In *Proc. of the Fifth IEEE International Workshop on Robot and Human Communication*, pages 183–188, Tsukuba, Japan, Nov. 1996.
- [56] M. Khemlani, J. Carr, and W. Crosbie. Muscle synergies and joint linkages in sit-to-stand under two initial foot positions. *Clinical Biomechanics*, 14(4):236–246, 1999.
- [57] K. Kobara, A. Eguchi, S. Watanabe, Y. Ishiura, D. Fujita, T. Nishimoto, and K. Shinkoda. Investigation of the validity of an experimental model for the estimated shear force on buttocks in a comfortable sitting posture. *Journal of Physical Therapy Science*, 20(3):157–162, 2008.
- [58] T. Kotake, N. Dohi, T. Kajiwara, N. Sumi, Y. Koyama, and T. Miura. An analysis of sit-to-stand movements. *Archives of physical medicine and rehabilitation*, 74(10):1095–1099, 1993.
- [59] A. Kralj, R. J. Jaeger, and M. Munih. Analysis of standing up and sitting down in humans: definitions and normative data presentation. *Journal of biomechanics*, 23(11):1123–1138, 1990.
- [60] J. Kuželicki, M. Žefran, H. Burger, and T. Bajd. Synthesis of standing-up trajectories using dynamic optimization. *Gait & posture*, 21(1):1–11, 2005.
- [61] A. Leardini, L. Chiari, U. Della Croce, and A. Cappozzo. Human movement analysis using stereophotogrammetry: Part 3. soft tissue artifact assessment and compensation. *Gait & posture*, 21(2):212–225, 2005.
- [62] C.-C. Liang and C.-F. Chiang. A study on biodynamic models of seated human subjects exposed to vertical vibration. *International Journal of Industrial Ergonomics*, 36(10):869–890, 2006.
- [63] S. R. Lord, S. M. Murray, K. Chapman, B. Munro, and A. Tiedemann. Sit-to-stand performance depends on sensation, speed, balance, and psychological status in addition to strength in older people. *The Journals of Gerontology Series A: Biological Sciences and Medical Sciences*, 57(8):M539–M543, 2002.

-
- [64] S.-Z. Lou, Y.-L. Chou, P.-H. Chou, C.-J. Lin, U.-C. Chen, and F.-C. Su. Sit-to-stand at different periods of pregnancy. *Clinical Biomechanics*, 16(3):194–198, 2001.
- [65] A. A. Maciejewski and C. A. Klein. Obstacle avoidance for kinematically redundant manipulators in dynamically varying environments. *The international journal of robotics research*, 4(3):109–117, 1985.
- [66] K. Manal, I. McClay, S. Stanhope, J. Richards, and B. Galinat. Comparison of surface mounted markers and attachment methods in estimating tibial rotations during walking: an in vivo study. *Gait & posture*, 11(1):38–45, 2000.
- [67] M. Mistry and S. Schaal. Representation and control of the task space in humans and humanoid robots. In *Humanoid Robotics and Neuroscience: Science, Engineering and Society*. CRC Press/Taylor & Francis, 2015.
- [68] K. Mombaur. Using optimization to create self-stable human-like running. *Robotica*, 27(3):321–330, 2009.
- [69] K. Mombaur. Optimization of sit to stand motions of elderly people for the design and control of physical assistive devices. *PAMM*, 14(1):805–806, 2014.
- [70] K. Mombaur and K.-L. H. Hoang. How to best support sit to stand transfers of geriatric patients: Motion optimization under external forces for the design of physical assistive devices. *Journal of Biomechanics*, 58:131–138, 2017.
- [71] F. Mourey, A. Grishin, P. d’Athis, T. Pozzo, and P. Stapley. Standing up from a chair as a dynamic equilibrium task: a comparison between young and elderly subjects. *The Journals of Gerontology Series A: Biological Sciences and Medical Sciences*, 55(9):B425–B431, 2000.
- [72] A. M. Mughal and K. Iqbal. A fuzzy biomechanical model for optimal control of sit-to-stand movement. In *2005 ICSC Congress on Computational Intelligence Methods and Applications*, pages 6–pp. IEEE, 2005.
- [73] A. M. Mughal and K. Iqbal. A fuzzy biomechanical model with h2 control system for sit-to-stand movement. In *2006 American Control Conference*, pages 3427–3432. IEEE, 2006.
- [74] A. M. Mughal and K. Iqbal. Physiological cost optimization for sit-to-stand transfer. In *2007 IEEE Region 5 Technical Conference*, pages 147–152. IEEE, 2007.

- [75] A. M. Mughal and K. Iqbal. Bipedal modeling and decoupled optimal control design of biomechanical sit-to-stand transfer. In *2008 International Workshop on Robotic and Sensors Environments*, pages 46–51. IEEE, 2008.
- [76] A. M. Mughal and K. Iqbal. Physiological cost optimization for bipedal modeling with optimal controller design. In *International conf. on computational and experimental engineering, Honolulu, Hawaii*, pages 16–21, 2008.
- [77] A. M. Mughal and K. Iqbal. Synthesis of angular profiles for bipedal sit-to-stand movement. In *2008 40th southeastern symposium on system theory (SSST)*, pages 293–297. IEEE, 2008.
- [78] A. M. Mughal and K. Iqbal. 3d bipedal model for biomechanical sit-to-stand movement with coupled torque optimization and experimental analysis. In *2010 IEEE International Conference on Systems, Man and Cybernetics*, pages 568–573. IEEE, 2010.
- [79] A. M. Mughal and K. Iqbal. 3d bipedal model with holonomic constraints for the decoupled optimal controller design of the biomechanical sit-to-stand maneuver. *Journal of biomechanical engineering*, 132(4), 2010.
- [80] Y. Nakamura, H. Hanafusa, and T. Yoshikawa. Task-priority based redundancy control of robot manipulators. *The International Journal of Robotics Research*, 6(2):3–15, 1987.
- [81] V. Norman-Gerum. *Predictive Dynamic Simulation of Healthy Sit-to-Stand Movement*. Dissertation, University of Waterloo, 2019.
- [82] ode45. <https://de.mathworks.com/help/matlab/ref/ode45.html>, 1994–2020. The MathWorks, Inc., accessed on 2020-09-02.
- [83] C. W. J. Oomens, O. Bressers, E. Bosboom, C. Bouten, and D. Bader. Can loaded interface characteristics influence strain distributions in muscle adjacent to bony prominences? *Computer methods in biomechanics and biomedical engineering*, 6(3):171–180, 2003.
- [84] B. Ozsoy and J. Yang. Simulation-based unassisted sit-to-stand motion prediction for healthy young individuals. In *International Design Engineering Technical Conferences and Computers and Information in Engineering Conference*, volume 46391, page V006T10A001. American Society of Mechanical Engineers, 2014.

-
- [85] Y.-C. Pai, B. Naughton, R. W. Chang, and M. Rogers. Control of body centre of mass momentum during sit-to-stand among young and elderly adults. *Gait & Posture*, 2(2):109–116, 1994.
- [86] Y.-C. Pai and M. W. Rogers. Speed variation and resultant joint torques during sit-to-stand. *Archives of physical medicine and rehabilitation*, 72(11):881–885, 1991.
- [87] A. Palevski, I. Glaich, S. Portnoy, E. Linder-Ganz, and A. Gefen. Stress relaxation of porcine gluteus muscle subjected to sudden transverse deformation as related to pressure sore modeling. *Journal of Biomechanical Engineering*, 128(5):782–787, Oct. 2006.
- [88] M. Pandy, B. Garner, and F. Anderson. Optimal control of non-ballistic muscular movements: a constraint-based performance criterion for rising from a chair. *Journal of Biomechanical Engineering*, 117(1):15–26, Feb. 1995.
- [89] E. Papa and A. Cappozzo. Sit-to-stand motor strategies investigated in able-bodied young and elderly subjects. *Journal of biomechanics*, 33(9):1113–1122, 2000.
- [90] A. Pedotti, V. Krishnan, and L. Stark. Optimization of muscle-force sequencing in human locomotion. *Mathematical Biosciences*, 38(1-2):57–76, 1978.
- [91] R. K. Prinz, S. W. Neville, and N. J. Livingston. Synthesizing the sit-to-stand movement using fuzzy logic and a simple biomechanical model. *CMBES Proceedings*, 33, 2010.
- [92] D. Raab. Vorlesungsskript zur Instrumentellen Bewegungsanalyse. Universität Duisburg-Essen, 2019.
- [93] G. Rasool, A. M. Mughal, and K. Iqbal. Fuzzy biomechanical sit-to-stand movement with physiological feedback latencies. In *2010 IEEE international conference on systems, man and cybernetics*, pages 316–321. IEEE, 2010.
- [94] P. O. Riley, D. E. Krebs, and R. A. Popat. Biomechanical analysis of failed sit-to-stand. *IEEE Transactions on rehabilitation engineering*, 5(4):353–359, 1997.
- [95] G. Roy, S. Nadeau, D. Gravel, F. Malouin, B. J. McFadyen, and F. Pottie. The effect of foot position and chair height on the asymmetry of vertical forces during sit-to-stand and stand-to-sit tasks in individuals with hemiparesis. *Clinical Biomechanics*, 21(6):585–593, 2006.

-
- [96] J. Russakow, O. Khatib, and S. M. Rock. Extended operational space formulation for serial-to-parallel chain (branching) manipulators. In *Proceedings of 1995 IEEE international conference on robotics and automation*, volume 1, pages 1056–1061. IEEE, 1995.
- [97] J. Russakow, S. M. Rock, and O. Khatib. An operational space formulation for a free-flying, multi-arm space robot. In *Experimental Robotics IV*, pages 448–457. Springer, 1997.
- [98] M. Sadeghi, M. E. Andani, F. Bahrami, and M. Parnianpour. Trajectory of human movement during sit to stand: a new modeling approach based on movement decomposition and multi-phase cost function. *Experimental brain research*, 229(2):221–234, 2013.
- [99] L. Saint-Bauzel, V. Pasqui, B. Gas, and J.-L. Zarader. Pathological sit-to-stand models for control of a rehabilitation robotic device. In *2007 IEEE 10th International Conference on Rehabilitation Robotics*, pages 347–355. IEEE, 2007.
- [100] M. Schenkman, R. A. Berger, P. O. Riley, R. W. Mann, and W. A. Hodge. Whole-body movements during rising to standing from sitting. *Physical therapy*, 70(10):638–648, 1990.
- [101] D. E. Schinstock, T. N. Faddis, and R. B. Greenway. Robust inverse kinematics using damped least squares with dynamic weighting. In *AIAA/NASA Conference on Intelligent Robotics in Field, Factory, Service and Space (CIRFFSS)*, volume 2, pages 861–869. NASA. Johnson Space Center, 1994.
- [102] A. B. Schultz, N. B. Alexander, and J. A. Ashton-Miller. Biomechanical analyses of rising from a chair. *Journal of Biomechanics*, 12(25):1383–1391, 1992.
- [103] G. Schultz and K. Mombaur. Modeling and optimal control of human-like running. *IEEE/ASME Transactions on mechatronics*, 15(5):783–792, 2009.
- [104] L. Sentis. *Synthesis and control of whole-body behaviors in humanoid systems*. Dissertation, Stanford university, 2007.
- [105] L. Sentis and O. Khatib. Task-oriented control of humanoid robots through prioritization. In *IEEE International Conference on Humanoid Robots*, pages 1–16, 2004.

-
- [106] F. Sibella, M. Galli, M. Romei, A. Montesano, and M. Crivellini. Biomechanical analysis of sit-to-stand movement in normal and obese subjects. *Clinical biomechanics*, 18(8):745–750, 2003.
- [107] B. Siciliano, L. Sciavicco, L. Villani, and G. Oriolo. *Robotics: modelling, planning and control*. Springer Science & Business Media, 2010.
- [108] S. B. Slotine. A general framework for managing multiple tasks in highly redundant robotic systems. In *proceeding of 5th International Conference on Advanced Robotics*, volume 2, pages 1211–1216, 1991.
- [109] G. Sommer, M. Eder, L. Kovacs, H. Pathak, L. Bonitz, C. Mueller, P. Regitnig, and G. A. Holzapfel. Multiaxial mechanical properties and constitutive modeling of human adipose tissue: a basis for preoperative simulations in plastic and reconstructive surgery. *Acta biomaterialia*, 9(11):9036–9048, 2013.
- [110] D. Thelen and F. Anderson. An operational space tracking algorithm for generating dynamic simulations of movement. In *Proceedings of the 5th International Symposium on Computer Methods in Biomechanics and Biomedical Engineering*, 2001.
- [111] D. G. Thelen, F. C. Anderson, and S. L. Delp. Generating dynamic simulations of movement using computed muscle control. *Journal of biomechanics*, 36(3):321–328, 2003.
- [112] Vicon. plug-in gait reference guide, 2018. Vicon Motion Systems Ltd.
- [113] F.-C. Wang, C.-H. Yu, Y.-L. Lin, and C.-E. Tsai. Optimization of the sit-to-stand motion. In *2007 IEEE/ICME International Conference on Complex Medical Engineering*, pages 1248–1253. IEEE, 2007.
- [114] D. A. Winter. *Biomechanics and motor control of human movement*. John Wiley & Sons, 2009.
- [115] H. R. Yamasaki, H. Kambara, and Y. Koike. Dynamic optimization of the sit-to-stand movement. *Journal of applied biomechanics*, 27(4):306–313, 2011.
- [116] J. Yang and B. Ozsoy. Three dimensional unassisted sit-to-stand prediction for virtual healthy young and elderly individuals. *Multibody System Dynamics*, pages 1–20, 2019.

DuEPublico

Duisburg-Essen Publications online

UNIVERSITÄT
DUISBURG
ESSEN

Offen im Denken

ub | universitäts
bibliothek

Diese Dissertation wird über DuEPublico, dem Dokumenten- und Publikationsserver der Universität Duisburg-Essen, zur Verfügung gestellt und liegt auch als Print-Version vor.

DOI: 10.17185/duepublico/73998

URN: urn:nbn:de:hbz:464-20210205-080052-5

Alle Rechte vorbehalten.